Université de Neuchâtel

Institut de Physique

Design, fabrication, and testing of intersubband infrared photodetectors operating at wavelengths between 2 μm and 17 μm

Thèse

Présentée à la Faculté des Sciences de l'Université de Neuchâtel

Pour l'obtention du grade de Docteur ès sciences

Par

Fabrizio Giorgetta

Soutenue le 20 décembre 2007

En présence du directeur de thèse

Prof. Daniel Hofstetter

et des rapporteurs

Dr. Quankui Yang et Prof. Peter Seitz

Université de Neuchâtel

FACULTE DES SCIENCES
Secrétariat-Décanat de la faculté
- Rue Emile-Argand 11
- CP 158
- CH-2009 Neuchâtel

IMPRIMATUR POUR LA THESE

Desing, fabrication, and testing of intersubband infrared photodetectors operating at wavelengths between 2µm and 17µm

Fabrizio GIORGETTA

UNIVERSITE DE NEUCHATEL

FACULTE DES SCIENCES

La Faculté des sciences de l'Université de Neuchâtel,
sur le rapport des membres du jury

MM. D. Hofstetter (directeur de thèse),
P. Seitz
et Q. Yang (Fraunhofer IAF, Freiburg D)

autorise l'impression de la présente thèse.

Neuchâtel, le 31 janvier 2008

Le doyen :
F. Kessler

UNIVERSITE DE NEUCHATEL
FACULTE DES SCIENCES
Secrétariat - décanat de la faculté
Rue Emile-Argand 11 - CP 158
CH-2009 Neuchâtel
Félix Kessler

■ Téléphone : +41 32 718 21 00 ■ Fax : +41 32 718 21 03 ■ E-mail : secretariat.sciences@unine.ch ■ www.unine.ch/sciences

Keywords

- Semiconductor heterostructures
- Intersubband transitions
- Infrared photodetectors
- Quantum cascade detectors

Mots-clés

- Hétérostructures semiconductrices
- Transitions intersousbandes
- Photodétecteur infrarouge
- Détecteurs à cascade quantique

Abstract

Intersubband (ISB) photon detectors based on photon - electron interactions between quantized electron subbands in the conduction band of semiconductor heterostructures are presented. As opposed to interband devices, the operating wavelength of ISB devices is set by choosing appropriate layer thicknesses of the heterostructure and is not fixed by the semiconductor material system. As only electrons are involved in ISB detection, ISB detectors are potentially faster compared to semiconductor interband detectors involving both conduction and valence band; the speed of the latter is limited by the slower holes in the valence band.

This work focuses on novel quantum cascade detectors (QCDs). In contrast to common photoconductive ISB photodetectors, QCDs do not require an external bias voltage due to their asymmetric conduction band profile. This results in a favorable noise behavior, reduced thermal load, and simpler readout circuits. Several QCDs with detection wavelengths ranging from 2 µm to 17 µm are designed, grown, processed, characterized, and discussed.

Using the $In_{0.53}Ga_{0.47}As$ / $In_{0.52}Al_{0.48}As$ semiconductor system, QCDs detecting at 17 µm, 10 µm, 7.5 µm, and 4.7 µm are presented. The specific detectivity $\mathcal{D}^*$ of the 17 µm QCD is 1×10^{11} Jones at an operating temperature of 5 K; this result is close to the background limited $\mathcal{D}^*_{BLIP} = 1.4 \times 10^{11}$ Jones at 17 µm.

As the shortest ISB wavelength between bound states in a heterostructures is determined by the conduction band offset at the interface between two semiconductors, $In_{0.53}Ga_{0.47}As$ / $In_{0.52}Al_{0.48}As$ QCDs can only be realized down to about 4.5 µm. To obtain shorter wavelengths, QCDs based on two alternative semiconductor heterostructures are presented.

An $In_{0.61}Ga_{0.39}As$ / $In_{0.45}Al_{0.55}As$ QCD operating at 4 µm is demonstrated. At 100 K, its specific detectivity is $\mathcal{D}^* = 1.9 \times 10^{11}$ Jones. This value compares favorably to commercial semiconductor photodetectors in this wavelength range; at 4 µm, the common MCT detectors reach specific detectivities around 1×10^{11} Jones at operating temperatures of 77 K.

To obtain even shorter wavelengths, InAlAs is replaced by $AlAs_{0.56}Sb_{0.44}$. Based on this system, a QCD detecting at 2 µm is presented.

Contents

List of Figures

List of Tables

Chapter 1

Introduction

"If we call *light*, those rays which illuminate objects, and *radiant heat*, those which heat bodies, it may be inquired, whether light be essentially different from radiant heat? In answer to which I would suggest, that we are not allowed, by the rules of philosophizing, to admit two different causes to explain certain effects, if they may be accounted for by one." Friedrich William Herschel in "Experiments on the Refrangibility of the invisible Rays of the Sun" [Herschel, 1800].

1.1 Historical overview: from the discovery of infrared radiation to megapixel QWIP arrays

Around 1800, Friedrich William Herschel studied the spectrum of sunlight using a prism. He measured the temperature of each color, and found the highest temperature beyond the visible red; this was the hour of birth for the study of infrared (IR) radiation, electromagnetic radiation of a wavelength λ longer than that of visible light ($\lambda \gtrsim 750\,\mathrm{nm}$) and shorter than that of microwaves ($\lambda \lesssim 1\,\mathrm{mm}$). In 1831 Melloni and Nobili showed that radiant heat can be reflected, refracted and polarized in the same way as visible light [Wikipedia, 2007]. One of the first infrared photodetectors was the thermopile designed by Leopoldo Nobili in 1835 and used by Macedonio Melloni (see Scott Barr [1962]). By 1860 it was known that two thirds of the solar spectrum lie outside the visible range. Photon detectors not based on the thermoelectric effect have been developed since the early 40's of the last century. Since the late 50's, photon detectors using semiconductor alloys have been explored, such as Mercury cadmium telluride (MCT or $Hg_{1-x}Cd_xTe$) which covers the wavelength range from $3\,\mu\mathrm{m}$ to $22\,\mu\mathrm{m}$.

Kroemer [1957], who received 1/4 of the physics Nobel Prize of the year 2000 "for developing semiconductor heterostructures used in high-speed- and opto-electronics", proposed heterostructures using sequences of thin semiconductor layers with different bandgaps. With this technique, Alferov [1970] (who received another 25% of the year 2000 Nobel Prize) demonstrated the first GaAs / $Al_xGa_{1-x}As$ continuous wave semiconductor laser.

Esaki and Tsu [1970] elaborated the theory of a one-dimensional periodic potential formed by a sequence of semiconductor heterostructures with different band gaps for which they coined the term superlattice (SL); they calculated width and position of narrow allowed and forbidden energy bands (called subbands) which arise in SLs with a short

period length of around 100 Å due to the subdivision of the Brillouin zone into a series of minizones. Esaki and Sakaki [1977] suggested the possibility to use such a SL made of GaAs and AlGaAs layers to detect IR light. Smith et al. [1983] demonstrated a photoconductor based on an AlGaAs SL. Ando et al. [1982] were the first to measure the absorption between two subbands, which later became generally known as intersubband (ISB) absorption and West and Eglash [1985] demonstrated the inverse dependence between peak ISB absorption energy and the thickness of the lower bandgap material layer known as quantum well (QW). This means that the thickness of the QW determines the operating wavelength of an ISB optoelectronic device. The first photoconductive QW infrared photodetector based on ISB transitions (QWIP) was demonstrated by Levine et al. [1987] and 7 years later Faist et al. [1994] reported on the first ISB laser for which they invented the name quantum cascade laser (QCL).

Since then many groups have been working on ISB photodetection in the IR. Schneider et al. [1991b, 1992] observed pronounced photovoltaic effects in an asymmetric multi QW (MQW) structure. In contrast to the photoconductive (PC) QWIP, such a device can be operated in a bias less photovoltaic (PV) mode. According to [Schneider, 1993], an optimized PV QWIP has superior noise properties, the capability to operate at higher photon fluxes, and an improved dynamical range in comparison to a PC QWIP.

QWIP focal plane array (FPA) cameras sensitive at wavelengths between 8 µm and 10 µm have reached commercial maturity and are nowadays used in military, security, surveillance, and medical applications. While todays commercial QWIP FPAs have a resolution of about 256 × 256 pixels, Gunapala et al. [2005] presented a 1024×1024 pixel dual band QWIP FPA based on GaAs / AlGaAs with cutoff wavelengths of 5.1 µm and 8.4 µm.

Hofstetter et al. [2002] used a QCL structure as photovoltaic detector. A similar ISB detector was presented by Gendron et al. [2004] and entitled quantum cascade detector (QCD). QCDs were demonstrated at detection wavelengths between 84 µm [Graf et al., 2004] and 2 µm [Giorgetta et al., 2007b]

An overview of ISB detector design, physical properties, and device performance is found for example in the review article of Levine [1993], in the book chapter of Liu [2000] or the book of Schneider and Liu [2006].

1.2 Motivation and outline of this thesis

Although intersubband detectors have already been studied for quite some time, they still are of high interest to research. Especially at the extremes of IR radiation, namely in the low energy THz and in the high energy near infrared (NIR) ranges, there are still challenges in finding the best materials and optimized designs. Only recently, two different ISB THz detector designs were proposed: a photoconductive QWIP by Liu et al. [2004] and a PV QCD by Graf et al. [2004].

As opposed to PC QWIPs, dark current is absent in PV QCDs. This leads to several advantages: as no dark current is present, dark current noise is also absent; the integration time in readout circuits can be extended since no dark current would saturate the readout capacitance; the thermal load of the detector is strongly reduced, which is of interest when the available cooling is limited, for example in space born systems or hand-held terrestrial

staring systems.

The aim of this work is to advance the understanding and performance of the novel QCD design and to extend its operation range towards the NIR. Although QCD devices have made substantial progresses during the last few years [Gendron et al., 2005], their potential advantage of a low Johnson noise is still limited by a low device resistance. This problem must be overcome if QCDs are to stand their ground compared to QWIPs in terms of detectivity and operating temperature. To achieve a higher resistance, the barrier thickness of the QCD has to be increased, while, by carefully designing the QCD structure, efficient photocurrent transport is maintained using resonant tunneling and photon assisted scattering.

Fast interband semiconductor photodetectors are only available for wavelengths up to about 1.6 µm. For fast light detection at longer wavelengths, ISB photodetectors are promising candidates. The fundamental speed limit of ISB detectors is the intersubband scattering time of electrons $\tau_{scatter} \leq 1$ ps, therefore they are known to be very fast devices; for QWIPs, detection at signal frequencies up to 82 GHz at 10 µm was reported by Liu and Li [1995] and Hofstetter et al. [2006] demonstrated a QCD working up to 23 GHz at 5 µm. Those devices were grown with the mature and lattice matched GaAs / $Al_xGa_{1-x}As$ respectively $In_{0.53}Ga_{0.47}As$ / $In_{0.52}Al_{0.48}As$ semiconductor materials. As the conduction band offset (CBO) between QW and barrier is the limiting factor for short wavelength ISB detectors, the shortest accessible ISB wavelength using aforementioned materials is about 4.5 µm. Thus, novel materials are required to shift these encouraging results to shorter wavelengths.

By increasing the In content above 53% in an InGaAs QW and reducing it below 52% in an InAlAs barrier, the CBO is increased compared to the 520 meV of the lattice matched $In_{0.53}Ga_{0.47}As$ / $In_{0.52}Al_{0.48}As$. A short wavelength QCD based on strained $In_{0.61}Ga_{0.39}As$ / $In_{0.45}Al_{0.55}As$ is proposed and demonstrated in this work. Its CBO of 610 meV is sufficient to obtain wavelengths around 4 µm.

The lattice matched $In_{0.61}Ga_{0.39}As$ / $AlAs_{0.56}Sb_{0.44}$ heterostructure offers a very large CBO of 1.6 eV. This material system is hence a good candidate to close the gap between fast interband and ISB photodetectors. Thus, several QCDs operating between 2.5 µm and 2 µm are demonstrated in this work as well.

Chapter 2 describes some theoretical aspects and is divided in two main parts. An introduction to the theory describing ISB transitions is given in section 2.1. The physics of photodetectors is described in section 2.2, containing the common photodetector quantities of detectivity, responsivity, and noise.

In chapter 3 different detection mechanisms in ISB IR detectors are described, namely photoconductive QWIPs, photovoltaic QCDs and photodetection through optical rectification. An overview of non ISB IR detectors is given in section 3.2.4. The numerical Schrödinger solver used to simulate band structures in this work is shortly presented in section 3.3.

Chapter 4 gives an overview of heterostructures based on different material systems in relation to ISB devices.

Chapter 5 describes the sample preparation and the spectroscopic measurement methods used in this work.

In chapter 6, ISB photodetectors operating between 4.7 µm and 17 µm are presented:

a GaAs bound to bound QWIP and an InP bound-to-miniband QWIP (both detecting at 10 µm), and four InP QCDs (detecting at 17 µm, 10 µm, 7.5 µm, and 4.7 µm).

Chapter 7 presents a strained InGaAs / InAlAs QCD operating at 4 µm and several InGaAs / AlAsSb QCDs operating between 2 µm and 2.5 µm.

Chapter 8, finally, gives a short conclusion and an outlook.

Chapter 2

Theoretical Framework

In this chapter the relevant physics principles concerning discrete energy states in a confined potential are given. The second part deals with photodetector physics including noise mechanism.

2.1 Electron wavefunctions in quantum wells

Intersubband photodetectors are based on ISB absorption in a QW. Thus, the ISB absorption coefficient in a single-particle, one band model is discussed using Fermi's golden rule; a more detailed discussion can be found in Helm [2000], Kittel [1996], Schwabl [1998], Sze [1981], or Bastard [1988].

2.1.1 Schrödinger equation

The Schrödinger equation describes the space- and time-dependence of quantum-mechanical systems.

According to the correspondence principle, physical quantities are assigned to operators in quantum mechanics [Schwabl, 1998]. This translates into the following relations:

$$\text{Momentum } \boldsymbol{p} \quad \longrightarrow \quad \frac{\hbar}{i}\nabla \tag{2.1}$$

$$\text{Energy } E \quad \longrightarrow \quad i\hbar\frac{\partial}{\partial t}\,. \tag{2.2}$$

Applying the correspondence principle to the Hamiltonian of a particle in a potential $V(\boldsymbol{r})$ and taking into account that the state of a quantum mechanical system is described by a wave function $\psi(\boldsymbol{r},t)$ results in

$$E = \frac{\boldsymbol{p}^2}{2m} + V(\boldsymbol{r}) \;\longrightarrow\; i\hbar\frac{\partial}{\partial t}\psi(\boldsymbol{r},t) = \left(-\frac{\hbar^2}{2m}\nabla^2 + V(\boldsymbol{r})\right)\psi(\boldsymbol{r},t)\,. \tag{2.3}$$

This is the Schrödinger equation

$$i\hbar\frac{\partial}{\partial t}\psi(\boldsymbol{r},t) \;=\; H\psi(\boldsymbol{r},t) \tag{2.4}$$

$$H \;=\; -\frac{\hbar^2}{2m}\nabla^2 + V(\boldsymbol{r})\,, \tag{2.5}$$

where H is the Hamiltonian. Provided that H is time independent, the wavefunction can be separated in a space-independent and a time-independent part: $\psi(\boldsymbol{r},t) = f(t)\psi(\boldsymbol{r})$. The time-independent Schrödinger equation reads

$$H\psi(\boldsymbol{r}) = E\psi(\boldsymbol{r}) \tag{2.6}$$

which is an eigenvalue equation with eigenstates $\psi(\boldsymbol{r})$ and eigenvalues E.

2.1.2 The envelope function model

A semiconductor crystal consists of periodically arranged atoms and can be represented by a periodic potential. According to the Bloch theorem, the total electron wave function $\psi(\boldsymbol{r},t)$ at the Γ point (center of the Brillouin zone) is the product of a Bloch function $u_\nu(\boldsymbol{r})$ varying on the scale of the host material's crystalline periodicity and an envelope function $f_n(\boldsymbol{r})$ which is a plane wave varying slowly compared to $u_\nu(\boldsymbol{r})$:

$$\psi_n(\boldsymbol{r},t) = f_n(\boldsymbol{r})u_\nu(\boldsymbol{r})\exp(-i\frac{E_n t}{\hbar}), \tag{2.7}$$

where n is the quantum number, E_n the energy eigenvalue and $f_n(\boldsymbol{r})$ the envelope function which depends on the QW potential and externally applied fields. Assuming that the Hamiltonian is time independent and that the lattice-periodic Bloch function $u_\nu(\boldsymbol{r})$ is the same in the QW and in the barrier, the solution to the Schrödinger equation reduces to the envelope function $f_n(\boldsymbol{r})$. For a free motion in the x and y directions (with z being the growth direction), where $\boldsymbol{k} = (k_x, k_y, 0)$ and $V(\boldsymbol{r}) = V(z)$, the envelope function can be written as:

$$f_{n\boldsymbol{k}}(\boldsymbol{r}) = \frac{1}{\sqrt{A}}e^{i\boldsymbol{kr}}\phi_n(z) \tag{2.8}$$

where A is the sample area. Inserting equation (2.8) in equation (2.6) leads to the one-dimensional time-independent Schrödinger equation

$$\frac{-\hbar^2}{2m^*}\phi_n(z)\left(\frac{d^2}{dx^2}+\frac{d^2}{dy^2}\right)e^{i\boldsymbol{kr}} + \frac{-\hbar^2}{2m^*}e^{i\boldsymbol{kr}}\frac{d^2}{dz^2}\phi_n(z) + e^{i\boldsymbol{kr}}V(z)\phi_n(z) = E_{n,\boldsymbol{k}}e^{i\boldsymbol{kr}}\phi_n(z). \tag{2.9}$$

Along the z axis, (2.9) becomes

$$-\frac{\hbar}{2m^*}\frac{d^2}{dz^2}\phi_n(z) + V(z)\phi_n(z) = E_n\phi_n(z). \tag{2.10}$$

For a minimum in the dispersion relation, the total eigenenergy for a free particle in the $x-y$ plane is quadratic in $\boldsymbol{k}$:

$$E(n,\boldsymbol{k}) = E_n + \frac{\hbar^2\boldsymbol{k}^2}{2m^*} \tag{2.11}$$

where m^* stands for the effective mass and the subband energies E_n depend on the potential $V(z)$. For the simple case of a symmetric finite single QW, (2.9) can be solved

analytically. However, for most real structures no analytical solution exists and ϕ_n and E_n are obtained by numerical simulation.

A sample consisting in a repeating sequence of thin layers of materials A and B reveals an additional periodicity along the growth direction z. In such a superlattice (SL) (2.10) needs to be solved for each material, and the boundary conditions at the interfaces $z = z_{AB}$,

$$\phi_n^A(z_{AB}) = \phi_n^B(z_{AB}) \quad \text{and} \quad \frac{1}{m^{*A}}\frac{d\phi_n^A}{dz}(z_{AB}) = \frac{1}{m^{*B}}\frac{d\phi_n^B}{dz}(z_{AB}), \tag{2.12}$$

must be fulfilled: the wavefunction has to be continuous and the probability current needs to be conserved across the interface. d is the period of the SL and j an integer. The resulting bandstructure $E_n(k_z)$ consists of minibands. The SL energy dispersion can be obtained through the tight binding model, where the interaction with the nearest neighboring QWs is taken into account [Bastard, 1988]:

$$E_n(k) = E_n \pm \frac{\Delta_n}{2} cos(k_z d) + \frac{\hbar^2(k_x^2 + k_y^2)}{2m^*} \tag{2.13}$$

In (2.13), E_n is the center and Δ_n the width of the n-th miniband, and d is the period of the SL. The minus holds for odd and the plus for even minibands. Since the electrons have a higher probability density in the QW than in the barrier, the effective electron mass m^* for the inplane motion is assumed to be identical to m^*_{QW}.

The miniband width Δ can be estimated by

$$\Delta_n/4 = \int \psi^n_{loc}(z) V(z) \psi^n_{loc}(z-d), \tag{2.14}$$

where ψ^n_{loc} is the n^{th} bound state wavefunction of the QW centered at $z = 0$ respectively $z = d$ when it is considered as isolated.

2.1.3 Intersubband absorption coefficient of a single quantum well

In a two dimensional system with discrete energy states where only the ground state is occupied, the transition rate W_{if} from the ground state $|\psi_i\rangle$ to a final state $|\psi_f\rangle$ under the influence of an external electromagnetic wave with frequency ω is given by Fermi's golden rule:

$$W_{if} = \frac{2\pi}{\hbar} |\langle \psi_i | H' | \psi_f \rangle|^2 \delta(E_f - E_i - \hbar\omega), \tag{2.15}$$

with $H' = \frac{e}{2m^*}(\boldsymbol{A}\cdot\boldsymbol{p} + \boldsymbol{p}\cdot\boldsymbol{A})$ being the interaction Hamiltonian and m^* the effective mass based on the one-band effective-mass model. $\boldsymbol{A}$ is the vector potential of the electric field $\boldsymbol{E}$ which is described by a plane electromagnetic wave with an amplitude E_0:

$$\boldsymbol{E}(\boldsymbol{r}, t) = E_0 \boldsymbol{e} \cos(\boldsymbol{q}\cdot\boldsymbol{r} - \omega t) = \frac{E_0 \boldsymbol{e}}{2}\left(e^{i(\boldsymbol{q}\cdot\boldsymbol{r}-\omega t)} + e^{-i(\boldsymbol{q}\cdot\boldsymbol{r}-\omega t)}\right), \tag{2.16}$$

$\boldsymbol{q}$ is the propagation vector, and $\boldsymbol{e}$ the linear polarization vector perpendicular to $\boldsymbol{q}$. Using $\boldsymbol{E} = \frac{-\partial \boldsymbol{A}}{\partial t}$ leads to

$$\boldsymbol{A}(\boldsymbol{r}, t) = \frac{E_0 \boldsymbol{e}}{\omega} \sin(\boldsymbol{q}\cdot\boldsymbol{r} - \omega t) = \frac{i E_0 \boldsymbol{e}}{2\omega} e^{i(\boldsymbol{q}\cdot\boldsymbol{r}-\omega t)} + \text{c.c.}\ . \tag{2.17}$$

If the characteristic length of the electronic system is much smaller than the wavelength of the radiation, H' can be simplified using the dipole approximation: $\boldsymbol{A}$ and $\boldsymbol{p}$ commute, resulting in $H' = \frac{e}{m^*}\boldsymbol{A}\cdot\boldsymbol{p}$. For ISB transitions (ISBT), this condition is almost always met; the QWs studied in this work have thicknesses of 10–160 Å whereas the free space wavelength of the detected radiation is 2–17 µm. Therefore, (2.15) can be rewritten as

$$W_{if} = \frac{2\pi}{\hbar}\frac{e^2E_0^2}{4m^{*2}\omega^2}|\langle\psi_i|\boldsymbol{e}\cdot\boldsymbol{p}|\psi_f\rangle|^2\delta(E_f - E_i - \hbar\omega). \tag{2.18}$$

Using (2.7), the matrix element $\langle\psi_i|\boldsymbol{e}\cdot\boldsymbol{p}|\psi_f\rangle$ can be split in two parts due to the significantly slower variation of the envelope function f_n as compared to the Bloch function u_ν:

$$\langle\psi_i|\boldsymbol{e}\cdot\boldsymbol{p}|\psi_f\rangle = \boldsymbol{e}\cdot\langle u_\nu|\boldsymbol{p}|u_{\nu'}\rangle\langle f_n|f_{n'}\rangle + \boldsymbol{e}\cdot\langle u_\nu|u_{\nu'}\rangle\langle f_n|\boldsymbol{p}|f_{n'}\rangle. \tag{2.19}$$

If the initial and final state lie in different bands ($\nu \neq \nu'$), the overlap integral of the Bloch function $\langle u_\nu|u_{\nu'}\rangle$ vanishes and only the first term remains. It therefore describes interband transitions, whose dipole matrix elements $\langle u_\nu|\boldsymbol{p}|u_{\nu'}\rangle$ are built on the Bloch functions [Rosencher and Vinter, 1998]. If the initial and final states lie in the same band ($\nu = \nu'$), the first term vanishes and $\langle u_\nu|u_{\nu'}\rangle = 1$. The second term describes hence ISBTs, whose dipole matrix elements $\langle f_n|\boldsymbol{p}|f_{n'}\rangle$ must be calculated using the envelope functions. The ISB dipole matrix element of the envelope function (2.8) is

$$\begin{aligned}&\langle f_{n\boldsymbol{k}}|\boldsymbol{e}\cdot\boldsymbol{p}|f_{n'\boldsymbol{k'}}\rangle \\ &= \frac{1}{A}\int d^3r e^{-i\boldsymbol{k}\boldsymbol{r}}\phi_n^*(z)\left[e_xp_x + e_yp_y + e_zp_z\right]e^{i\boldsymbol{k'}\boldsymbol{r}}\phi_{n'}(z).\end{aligned} \tag{2.20}$$

Due to the particular form of the envelope function, ISBTs are only allowed between states having the same wave vectors $\boldsymbol{k}^i_{x,y} = \boldsymbol{k}^f_{x,y}$; for transitions between different initial and final states ($n \neq n'$) only the term proportional to e_z does not vanish. In semiconductor heterostructures, this polarization selection rule allows optical transitions only if the electric field has a component perpendicular to the semiconductor layers. This reduces the dipole matrix element describing ISB transitions in a one band model to

$$\langle n|p_z|n'\rangle = \mu_{nn'} = \int dz\phi_n^*(z)p_z\phi_{n'}(z). \tag{2.21}$$

In an ideal QW with a symmetric potential, the wavefunctions ϕ are also symmetric and have either an even or an odd parity; the dipole matrix element (2.21) becomes zero if ϕ_n and $\phi_{n'}$ have the same parity. This is known as the parity selection rule.

A commonly used quantity in spectroscopy is the dimensionless oscillator strength

$$f_{nn'} = \frac{2}{m^*\hbar\omega_{n'n}}|\langle n|p_z|n'\rangle|^2 = \frac{2m^*\omega_{n'n}}{\hbar}|\langle n|z|n'\rangle|^2 \tag{2.22}$$

obeying the sum rule

$$\sum_{n'} f_{nn'} = 1 \tag{2.23}$$

where $f_{nn'}$ is positive for $n < n'$ (absorption) and negative for $n > n'$ (emission). An interesting aspect of this sum rule is the fact that a higher lying quantum transition can

have $f_{nn'} > 1$. This is equivalent to a high transition probability between n and n', which could be potentially used in devices. The definition of the oscillator strength has to be adapted for multiband or nonparabolic models [Sirtori et al., 1994].

Based on the dipole matrix element (2.21), the absorption coefficient α can be calculated. In general, α is defined as the ratio between absorbed electromagnetic energy per volume V and time ($\hbar\omega \times W_{if}/V$) and the intensity of the incident radiation ($I = 1/2 \times \epsilon_0 cnE_0^2$). In the case of a quasi-two-dimensional system (for example a QW) a two dimensional absorption coefficient α_{2D} is defined. As opposed to the three dimensional α which has the dimension of inverse length, α_{2D} is dimensionless. If the sum over all possible initial and final states n, n' (considering emission and absorption) is taken into account, α_{2D} is given by

$$\begin{aligned}\alpha_{2D} =& \frac{\hbar\omega}{IA} \sum_{n,n'} \sum_{\boldsymbol{k}_\perp} \frac{2\pi}{\hbar} |\langle n| \frac{e}{m^*} \boldsymbol{A} \cdot \boldsymbol{p} |n'\rangle|^2 \times \\ & [f(E_n(\boldsymbol{k})) - f(E_{n'}(\boldsymbol{k}))]\, \delta(E_{n'}(\boldsymbol{k}) - E_n(\boldsymbol{k}) - \hbar\omega),\end{aligned} \tag{2.24}$$

where $f(E_n)$ is the occupation in state n given by the Fermi-Dirac distribution. Using (2.17) and $I = 1/2 \times \epsilon_0 cnE_0^2$, applying the polarization selection rule and changing the summation over $\boldsymbol{k}$ into a 2D-integral leads to

$$\begin{aligned}\alpha_{2D} =& \frac{\pi e^2}{\epsilon_0 cn\omega m^{*2}} \sum_{n,n'} \frac{2}{(2\pi)^2} \times \\ & \int d^2\boldsymbol{k} |\langle n| p_z |n'\rangle|^2 \left(f(E_n) - f(E_{n'})\right) \delta(E_{n'} - E_n - \hbar\omega).\end{aligned} \tag{2.25}$$

Assuming a parabolic in-plane dispersion (2.11), the integration over the Fermi-Dirac distributions can be solved analytically. Additionally, the δ function is replaced by a Lorentzian with a full width at half maximum (FWHM) of 2Γ to take into account the finite lifetime of the excited state. Assuming $\omega_{nn'} \approx \omega$ [Helm, 2000] the absorption coefficient is

$$\alpha_{2D} = \frac{e^2 k_B T}{2\epsilon_0 cn\hbar} \sum_{n,n'} f_{nn'} \ln\left(\frac{1 + e^{\frac{E_F - E_n}{k_B T}}}{1 + e^{\frac{E_F - E_{n'}}{k_B T}}}\right) \frac{\Gamma/\pi}{(E_{n'} - E_n - \hbar\omega)^2 + \Gamma^2}. \tag{2.26}$$

In ISB structures, often only the transition between the ground state and the first excited state of the QW, which has the largest oscillator strength, is of interest. For this transition, using $\ln\left(\frac{\cdot}{\cdot}\right) \approx \frac{E_F - E_1}{k_B T}$, (2.26) simplifies to

$$\alpha_{2D} = \frac{n_s e^2 \hbar}{2\epsilon_0 cnm^*} f_{12} \frac{\Gamma}{(E_2 - E_1 - \hbar\omega)^2 + \Gamma^2} \qquad \text{at } k_B T \ll E_F - E_1. \tag{2.27}$$

2.1.4 Manybody effects

The single particle Schrödinger equation does not include the electrostatic interaction between electrons, it is based on the assumption that carriers are far apart from each other and do not interact. In heavily doped semiconductors, this simplification can lead to significant errors. To improve the simulation of ISBTs, the interactions between carriers,

so-called manybody effects, must be taken into account. The following discussion is based on Helm [2000].

Kohn and Sham [1965] introduced the exchange-correlation potential $V_{xc}(n(z))$ based on the electron density $n(z)$ as fundamental variable (omitting the complex many-electron wavefunction). Exchange and correlation introduces a lowering of the total potential in regions of high electron density, resulting in a blue shift of typical ISBTs where the electron population lies mostly in the ground state.

$V_{xc}(n(z))$ can be computed in the local density approximation as a function of the electron density:

$$\begin{aligned} V_{xc} &= -\left(\frac{9\pi}{4}\right)^{1/3} \frac{2}{\pi r_s(n(z))} \times \\ &\quad \left[1 + \frac{0.7734}{21} r_s(n(z)) \ln\left(1 + \frac{21}{r_s(n(z))}\right)\right] \frac{e^2}{8\pi\epsilon\epsilon_0 a_B^*} \end{aligned} \tag{2.28}$$

$$r_s = \left[\frac{4\pi}{3} a^* 3n(z)\right]^{-1/3} \tag{2.29}$$

$$n(z) = \frac{m^* kT}{\pi\hbar^2} \sum_i \ln\left[1 + e^{\frac{E_F - E_i}{kT}}\right] |\psi_i(z)|^2 \tag{2.30}$$

where the dimensionless parameter r_s is the mean electron separation normalized to the effective Bohr radius $a^* = \frac{4\pi\epsilon_0\epsilon_r\hbar^2}{m_0 m^* e^2}$ and characterizes the electron gas; $\psi_i(z)$ are the wavefunctions in the QW, and E_F is the Fermi level.

External radiation not only excites electrons from the first state into a higher lying state in the QW, but leads also to a modulation of the carrier density. This collective oscillation of the electron plasma screens the external infrared field and results in an increase of the transition energy. The frequency or depolarization shift of the ISBT E_{12} α describing this phenomenon is given by

$$\alpha = \frac{2e^2 n_s}{\epsilon\epsilon_0 E_{12}} \int_{-\infty}^{\infty} dz \left[\int_{-\infty}^{z} dz' \psi_2(z')\psi_1(z')\right]^2, \tag{2.31}$$

where $\epsilon\epsilon_0$ is the semiconductor permittivity, and n_s the sheet carrier density.

On the other hand, the ISBT energy is reduced by THE coulomb interaction between the excited electron and the quasi-hole left behind in the ground state. This so-called excitonic correction is described by a parameter β which can be expressed by

$$\beta = -\frac{2n_s}{E_{12}} \int_{-\infty}^{\infty} dz \psi_2(z)^2 \psi_1(z)^2 \frac{\partial V_{xc}(n(z))}{\partial n(z)}, \tag{2.32}$$

where V_{xc} is the exchange correlation potential and $n(z)$ is the electron density, both described in (2.28).

The combined depolarization (α) and excitonic (β) shifts of the ISBT E_{12} result in an effective ISBT energy $\tilde{E}_{12}$ of

$$\tilde{E}_{12}^2 = E_{12}^2(1 + \alpha - \beta). \tag{2.33}$$

Density of states and Fermi level In a bulk semiconductor, the energy dependent density of states for energies E greater than the conduction band edge E_c is:

$$\frac{dN_{3D}}{dE} = \frac{(2m^*)^{3/2}}{2\hbar^3\pi^2}\sqrt{E - E_c} \qquad and \qquad n_{3D} = \frac{1}{3\hbar^3\pi^2}\sqrt{(2m^*(E_F - E_c))^3} \tag{2.34}$$

where E_F is the Fermi level and n_{3D} the 3D carrier density. To achieve ISB absorption in a 2D QW, it needs to be degenerately doped in such a way that the Fermi level lies between the ground state E_1 and the first excited state E_2. Assuming a complete ionization of the donors, the 2D sheet carrier density n_s is hence

$$n_s = \frac{m^*}{\pi\hbar^2}(E_F - E_1). \tag{2.35}$$

In ISB detector structures, the contact layers are doped up to the n_{3D} where their Fermi level equals the Fermi level of the active QWs $E_{F3D,contact} = E_{F2D,QW}$ in order to provide efficient electron injection into the active region.

2.2 Photodetector physics

In this section, photodetector concepts used in this work are introduced. If not otherwise cited, it is based on Rogalski [2003], Wolfe and Zissis [1985], and Liu [2000].

A photodetector can be described as a radiation transducer, which changes the incoming radiation into an electric signal. The methods of transduction can be separated into two groups:

Thermal detectors are sensitive to changes in the temperature brought about by changes in incident radiation. They employ transduction processes including the bolometric, thermovoltaic, thermopneumatic, and pyroelectric effect. Thermal detectors have a broad spectral response and can often be considered to be wavelength independent; their response depends upon the radiant power, but not upon its spectral content.

Photon detectors are sensitive to changes in the number or mobility of free electrons, holes, or both, that are brought about by changes in the number of incident photons. They employ transduction processes including the photovoltaic, photoconductive, photoelectromagnetic, and the photoemissive effect. The photon detector response per unit incident radiant power depends selectively on wavelength: if the wavelength is longer than the cutoff wavelength, the detector response drops to zero.

As this work deals with photoconductive and photovoltaic photon detectors, the remainder of this section focuses on those photodetection mechanisms.

2.2.1 Responsivity

The current responsivity $\mathcal{R}$ is defined as detector output current I_S per unit of input signal power P_S. The efficiency of photon detectors is given by the quantum efficiency

$$\eta = \frac{\overline{n_{det}}}{\Phi}, \tag{2.36}$$

where $\overline{n_{det}}$ is the average amount of photogenerated carriers and $\Phi = P_s/h\nu$ is the amount of incident photons, both per unit time. The photodetector gain g_p is defined as the ratio between the average number $\overline{n_x}$ of electrons that are collected in the external circuit and the average number $\overline{n_{det}}$ of detected photons,

$$g_p = \overline{n_x}/\overline{n_{det}}. \tag{2.37}$$

The detector output current I_s can thus be expressed as $I_s = q\eta g_p \Phi$, and the current responsivity $\mathcal{R} = I_s/P_s$ is given by

$$\mathcal{R}(\nu) = \frac{I_S}{P_S} = \frac{q}{h\nu}\eta g_p = \frac{\lambda q}{hc}\eta g_p, \tag{2.38}$$

where $\nu = c/\lambda$ is the signal frequency, λ the signal wavelength, c the vacuum speed of light, q the elementary charge, and h Planck's constant.

2.2.2 Noise mechanisms

Noise is a random variation of an entity such as voltage or current and is described by the variance $\mathrm{var}(x) = \overline{(x - \overline{x})^2}$, where x is a stochastic variable. For photodetectors transforming light into current, noise is determined by $i_n^2 = \mathrm{var}(I)$, where i_n^2 is the squared current noise and I the total current through the photodetector.

Several noise sources contribute to the overall photodetector noise:

$1/f$ noise is a noise signal with its power spectral density proportional to the reciprocal of the frequency. It was not observed for the photodetectors presented in this work and thus not further discussed.

Johnson noise (also known as Nyquist or thermal noise) is the electronic noise generated by the thermal agitation of the charge carriers (usually the electrons) inside an electrical conductor at equilibrium, which happens regardless of any applied voltage. It was first measured by Johnson [1928] at Bell labs. The root mean square value i_n^J of the Johnson noise current is given by

$$i_n^J = \sqrt{\frac{4k_B T \Delta f}{R}}, \tag{2.39}$$

where k_B is the Boltzmann constant, Δf the measurement electrical bandwidth in Hz, and R the device resistance in Ω.

Dark current noise results from current flowing through the photodetector in the absence of irradiation. It is caused by current fluctuations because of the discrete nature of charge carriers and thus obeys a Poisson distribution; noise associated with a Poisson distribution is also called shot noise. The root mean square dark noise current i_n^d is given by

$$i_n^d = \sqrt{uqg_n I_d \Delta f}, \tag{2.40}$$

where q is the elementary charge, and I_d the device dark current. u is a constant describing the noise generation mechanism: $u = 2$ in the case of generation (photodiodes) and $u = 4$ in

the case of generation-recombination (photoconductors). The noise gain g_n approximately equals the photoconductive gain g_p in conventional photoconductors, whereas g_n can be larger than g_p for QWIPs. To minimize dark current noise, I_d must be reduced, which is the reason why for a photoconductor operated at a given bias voltage, a high resistance is desirable.

Photon noise, just as dark current noise, manifests itself as shot noise. The dark current I_d in (2.40) is replaced by a photon noise current I_{ph} given by

$$I_{ph}/A = J_{ph} = q \int g_p \eta(\nu) \frac{d\Phi_{BG}(\nu)}{d\nu} d\nu \tag{2.41}$$

resulting in

$$i_n^{ph} = \sqrt{uq^2 g_n \int g_p \eta(\nu) \frac{d\Phi_{BG}(\nu)}{d\nu} d\nu A \Delta f}, \tag{2.42}$$

where A is the detector surface, η the quantum efficiency and $\frac{d\Phi_{BG}(\nu)}{d\nu}$ the background photon flux spectral density in $\mathrm{m^{-2}s^{-1}Hz^{-1}}$. For a full cone field of view (FOV) angle Θ it is related to the emissivity $L_{\Theta\nu}$ in $\mathrm{Wm^{-2}Hz^{-1}sr^{-1}}$ by

$$h\nu \cdot \frac{d\Phi_{BG}(\nu)}{d\nu} = \pi \sin^2 \frac{\Theta}{2} \cdot L_{\Theta\nu}(\nu, T). \tag{2.43}$$

For an ideal blackbody, the emissivity is given by

$$L_{\Theta\nu}(\nu, T) = \frac{2h\nu^3}{c^2} \frac{1}{e^{\frac{h\nu}{k_B T}} - 1}, \quad L_{\Theta\lambda}(\lambda, T) = \frac{2hc^2}{\lambda^5} \frac{1}{e^{\frac{hc}{\lambda k_B T}} - 1}, \tag{2.44}$$

where T is the black body temperature, h Planck's constant, c the vacuum speed of light, k_B Boltzmann's constant, ν the frequency and λ the wavelength of the emitted light. For a quantum efficiency η which is independent of detector temperature T, the photon noise does not depend on the device temperature as opposed to Johnson and dark current noise. Background photon noise can be reduced by decreasing the FOV using a cold shield with an appropriate aperture.

2.2.3 Detectivity

An important detector characteristic is the specific detectivity D^*, which is the signal (per unit incident power) to noise ratio normalized by the detector area and the measurement electrical bandwidth:

$$D^* = \frac{\mathcal{R}_p}{i_n} \sqrt{A\Delta f}. \tag{2.45}$$

In (2.45), $\mathcal{R}_p$ is the peak current responsivity in A/W, A the detector surface, Δf the electrical bandwidth of the measurement, and i_n is the root mean square noise current. The units of D^* are Jones [J], which correspond to $\mathrm{cm}\sqrt{\mathrm{Hz}}/\mathrm{W}$.

Using (2.40) for dark current noise, (2.45) becomes

$$D_d^* = \mathcal{R}_p \sqrt{\frac{A}{uqI_d g_n}}. \tag{2.46}$$

This expression is useful for photoconductors, where usually generation-recombination noise dominates.

For photovoltaic detectors, where the detectivity is Johnson noise (2.39) limited at elevated temperatures,

$$D_J^* = \mathcal{R}_p \sqrt{\frac{AR_0}{4k_BT}}. \tag{2.47}$$

As D_J^* and D_d^* increase with decreasing temperature, the detectivity is photon noise limited at low temperatures. This photon noise limited detectivity is known as background limited infrared performance (BLIP) detectivity $\mathcal{D}_{BLIP}^*$. By inserting (2.42) into (2.45), one obtains

$$D_{BLIP}^* = \frac{\mathcal{R}(\nu)}{\sqrt{uq^2 g_n \int g_p \eta(\nu') \frac{d\Phi_{BG}(\nu')}{d\nu'} d\nu'}}. \tag{2.48}$$

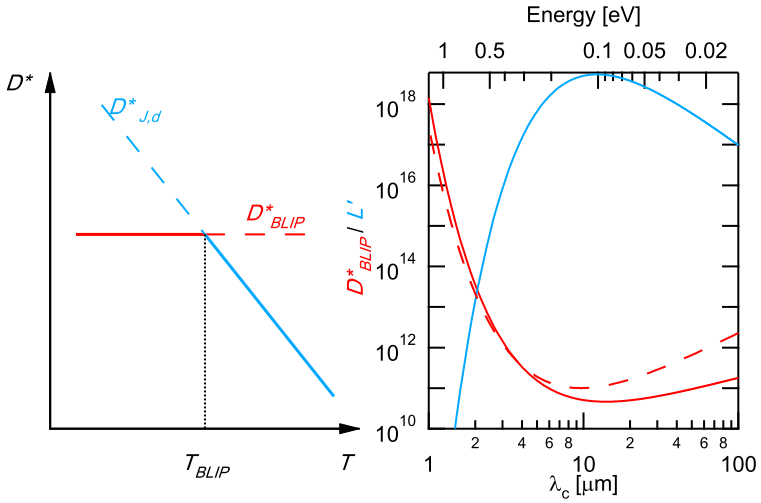

Figure 2.1: Left: D^* as function of temperature . At T_{BLIP}, the Johnson or dark current limited $D_{J,d}^*$ crosses the background limited D_{BLIP}^*. Right: photovoltaic D_{BLIP}^* in Jones for a 300 K blackbody temperature, $\Theta = \pi$, and $\eta = 1$ (red) as function of cutoff wavelength λ_c (solid) and for a Lorentzian spectral sensitivity with a fractional linewidth of 6% (dashed); the blue line is the photon flux spectral density $L' = L/(h\nu)$ of a 300 K blackbody in $[\mathrm{s}^{-1}\mathrm{Hz}^{-1}\mathrm{cm}^{-2}\mathrm{sr}^{-1}]$.

The left panel of figure 2.1 shows the schematic temperature dependence of a photodetectors detectivity: below a characteristic temperature T_{BLIP}, at which $i_n^{ph} = i_n^d$ or $i_n^{ph} = i_n^J$, the detectivity is background limited ($D^* = D_{BLIP}^*$) and temperature independent if one assumes that the absorption efficiency η, too, is temperature independent. At temperatures above T_{BLIP}, $D^* = D_d^*$ or $D^* = D_J^*$ decreases with increasing temperature. D_{BLIP}^* is presented on the right panel of figure 2.1 for an ideal ($\lambda < \lambda_c : \eta = 1,\ \eta = 0$ otherwise) photovoltaic detector as function of the cutoff wavelength λ_c for a 300 K background and a hemispheric FOV. For comparison, D_{BLIP}^* is shown for a Lorentzian shaped spectral sensitivity with a fractional linewidth of 6%, a typical lineshape of an ISB photodetector.

D_{BLIP}^* and T_{BLIP} for 300 K background illumination are commonly used as figure of merit for infrared detectors.

Noise equivalent temperature difference ($NE\Delta T$) is defined as the temperature difference of the background required to produce an electric signal equal to the RMS noise signal. For N_s signal electrons and N_n noise electrons, using $dN_s/dT \approx (h\nu/k_B T^2)$, $NE\Delta T$ is given by [Schneider and Liu, 2006]:

$$NE\Delta T = \frac{N_n}{dN_s/dT} = \frac{N_n}{N_s}\frac{k_B T^2}{h\nu}. \tag{2.49}$$

For an ideal photoconductor, (2.49) becomes

$$NE\Delta T = \frac{k_B T^2}{h\nu}\sqrt{\frac{2g_n}{N_s}} \tag{2.50}$$

$NE\Delta T$ is the objective criterion of performance of imaging devices such as a FPAs [Rogalski, 2003].

Chapter 3

Design and Simulation of Intersubband Photodetectors

This chapter starts with an overview of sample geometries adequate for ISB devices, describes different designs of ISB photodetector structures, and shortly discusses the simulation of ISB conduction band structures.

3.1 Sample geometries

As discussed in section 2.1.3, only the electric field component perpendicular to the QW layers interacts with ISBTs. The sample geometry of an ISB device must thus ensure that the internal light propagation is not perpendicular to the sample surface. This is easily achieved by illuminating the sample at an oblique angle as shown in figure 3.1 b), preferably the Brewster angle at which the reflection of the TM-polarization (the electric field component polarized in the plane of incidence) at the air - semiconductor interface vanishes. However, the high refractive index of most semiconductors results in a small angle of incidence within the sample in the Brewster configuration ($\Theta = 17°$ for InGaAs with a refractive index of $n = 3.3$). The effective coupling between electric field and ISB absorption for this case is $\sin^2 17°/\cos 17° = 0.09$ for the single pass of the light through the structure, where $\sin^2\Theta$ accounts for the fraction of the radiation intensity polarized perpendicularly to the growth plane and $\cos\Theta$ describes the effective interaction length in the QW. The Brewster angle configuration is hence only suitable for ISB devices with a high absorbance $N_{QW}\alpha_{2D}$.

An alternative sample geometry is the 45° multipass waveguide (MPW), depicted in figure 3.1 a). In a standard MPW two opposite facets are polished into 45° wedges; to minimize scattering losses, the backside of the substrate is also polished. The light beam is coupled into the sample perpendicularly to one of the polished facets, undergoes several total internal reflections and exits the sample through the other 45° facet. The number of passes through the active region is $n_P = L/D$, where L is the sample length and D its thickness including the substrate. Compared to the effective coupling of 0.09 for the Brewster angle geometry, a value of $\sin^2 45°/\cos 45° = 1/\sqrt{2} \approx 0.7$ is obtained in a 45° MPW. In addition, the light passes n_P times through the active region in a 45° MPW compared to a single pass in the Brewster geometry.

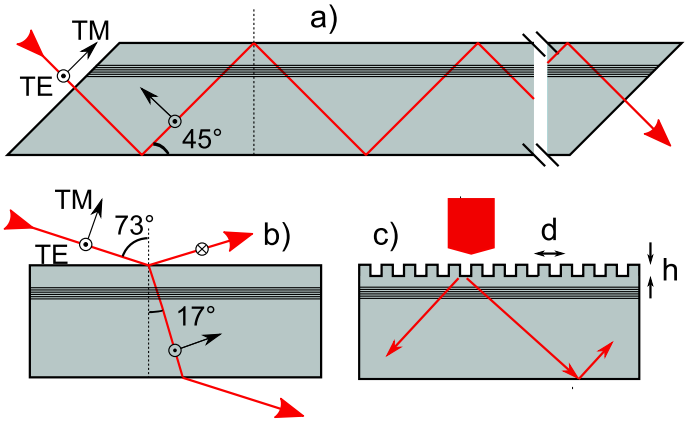

Figure 3.1: Schemes of different ISB device geometries. a): 45° multipass waveguide. b): Brewster angle configuration. c): Grating coupler.

The 45° MPW geometry still 'throws away' 50% of the incident TM polarized light intensity. A more efficient coupling can be obtained by the use of a grating coupler. Grating couplers, which allow for incoming light perpendicular to the growth plane, are also the best choice for ISB imaging applications, since the 45° MPW geometry can not be applied to two dimensional ISB detector arrays. Gratings can be either etched directly into the cap layer of the sample or deposited by metal evaporation. On the downside, gratings complicate sample processing and need to be adjusted for different operating wavelengths. As the grating dimensions are proportional to the operating wavelength, short wavelength gratings involve more demanding processing.

In figure 3.1 c) a grating coupler consisting of pits etched into a sample's cap layer is schematically depicted. To obtain a maximal diffraction angle and thus absorption, the grating period d should equal approximately the device operating wavelength in the semiconductor $d = \lambda_0/n$, where λ_0 is the free space wavelength and n the refractive index of the semiconductor. The etch depth h should be about one fourth of d. To eliminate direct reflection of the zeroth order diffraction, the areas of the etched and unetched regions should be about the same [Schneider and Liu, 2006]. Figure 3.2 shows a scanning electron micrograph of a grating processed onto a QCD detecting at 5 µm.

In this work, all detectors are processed into 45° MPWs due to the simple processing and the well defined electric field strength and intensity in the sample, allowing for easier comparison between different samples and theory.

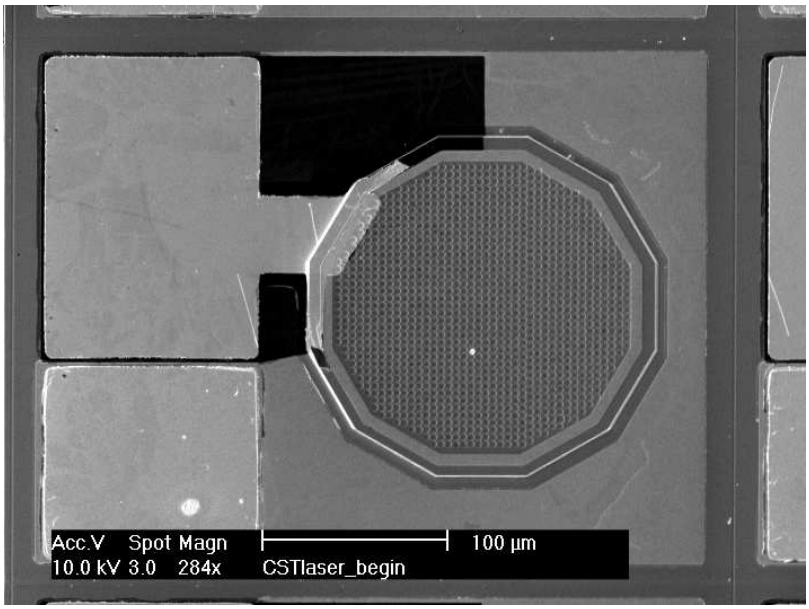

Figure 3.2: Pit grating on a QCD detecting at 5 µm. After etching the area surrounding the polygonal mesa down to the lower contact layer, shallow pits are etched into the structure's upper contact layer. An insulating Si_3N_4 layer is then deposited (black area on top left). Finally, two metal bond pads are evaporated: one on the insulator contacting the upper contact layer on top of the mesa (top left), the other on the etched area surrounding the mesa contacting the lower contact layer (bottom left).

3.2 Intersubband photodetector designs

In this section, different working principles for ISB infrared photodetectors are presented. Detailed information on the subject can be found in Schneider and Liu [2006] and references therein.

The by far most common design is the photoconductive (PC) quantum well infrared photodetector (QWIP), where the change of device resistance under illumination is determined by applying an external bias voltage across the detector and measuring the current at the same time. Photovoltaic (PV) ISB detectors on the other hand possess an internal field due to an asymmetric conduction band potential; no external bias is applied, the detector acts as a current source. The PV quantum cascade detector (QCD) design was used for most detectors presented in this work. Optical rectification, another PV ISB detection mechanism, is also briefly discussed.

3.2.1 Quantum well infrared photodetector

The active region of a QWIP consists of identical QWs separated by significantly thicker barriers, as seen in the schematic conduction band profile in figure 3.3 on the top. The QW thickness and CBO are chosen such that the second quantized electron level is close to resonance with the barrier's conduction band edge. Light detection is based on photoemission of electrons from the QWs: electrons are excited from the QW ground state to the first excited state by photon absorption and are swept out of the QW by an externally applied electric field, thus generating a measurable photocurrent depicted by the red arrows in figure 3.3. The photoconductive gain g_p and thus the responsivity $\mathcal{R}$ of a QWIP is given by

$$g_p = \frac{p_e}{N_{QW} p_c}, \qquad \mathcal{R} = \frac{e}{h\nu}\eta g_p = \frac{e}{h\nu}\eta \frac{p_e}{N_{QW} p_c}, \tag{3.1}$$

where p_e is the escape probability from the QW into the continuum above the barrier for a photoexcited electron, p_c is the capture probability of an electron from the continuum into the QW, N_{QW} is the total number of QWs in the active region, and η is the absorption efficiency.

Depending on the position of the upper electron level E_2, one distinguishes between bound to bound (E_2 about 10 meV below barrier), bound to quasi bound (E_2 in resonance with barrier) and bound to continuum (E_2 about 10 meV above the barrier) QWIPs. Of those three designs, the bound to quasi bound QWIP has the best performance as it gives both a large absorption η (as does the bound to bound QWIP) and a large escape probability p_e (as does the bound to continuum QWIP) [Liu, 1993].

The prevalent noise mechanism of PC QWIPs is dark current noise (2.40). In order to suppress inter-QW tunneling current, QWIPs have thick barrier layers (about 30−50 nm); the dark current I_d (indicated by black arrows in figure 3.3) is thus dominated by thermionic emission of electrons out of the QWs.

A less common PC QWIP design is the bound to miniband (B2M) QWIP shown at the bottom of figure 3.3. The thick barrier is replaced by multiple thin QWs and barriers forming a ground state miniband. The active QW contains two bound states of which the upper one is in resonance with the above mentioned miniband. The continuum is thus 'replaced' by the miniband. This design allows to decouple the detection energy from

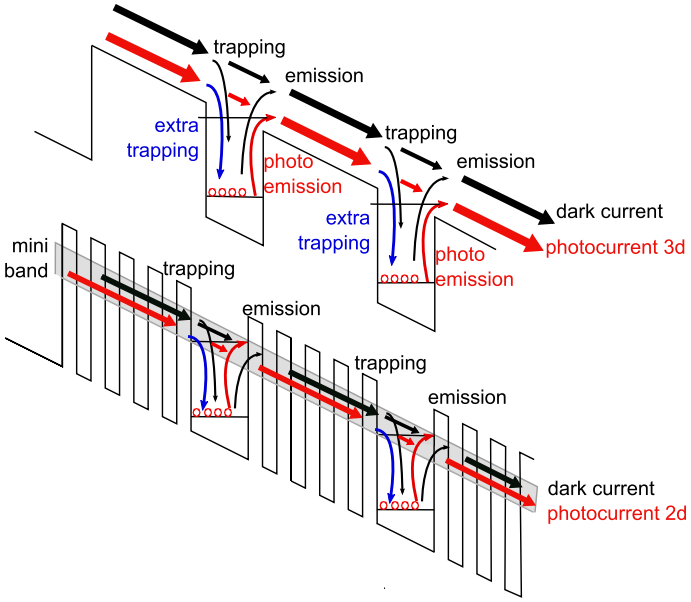

Figure 3.3: Schematic of a bound to quasibound QWIP (after Liu [2000]) and of a bound to miniband QWIP. Electrons are excited either by photoemission (red arrows) or by thermionic emission (black arrows) from the QW. Once excited, they contribute to dark- and photocurrent until being recaptured by another QW or collected by the anode.

the CBO, as the excited state of the active QW does not need to be close to the barrier's conduction band edge. The detection spectrum bandwidth is given by the miniband width which again is controlled by the thickness of the thin barrier and QW layers. Compared to the bound to quasibound design, a B2M QWIP has a lower g_p, because the photoexcited electron transport occurs in the miniband, which has a lower mobility compared to the continuum resulting in a lower p_e [Gunapala and Bandara, 2000].

3.2.2 Quantum cascade detector

Quantum cascade detectors (QCDs) are photovoltaic devices: they have a built in asymmetric conduction band potential which allows for bias less operation. The active region is built up of multiple periods, each containing a thick, degenerately doped active QW and a nominally undoped extraction cascade. As schematically shown in the upper panel of figure 3.4, the function of this cascade is to introduce an asymmetry in the band potential such that photoexcited electrons have a preferential escape direction, resulting in a measurable net photocurrent. For a QCD, this cascade is realized through multiple QWs with varying thicknesses. The ground state of the first QW of the extraction cascade is in resonance with the excited state of the active QW and the one of the QW on the opposite end of the cascade lies just above the ground state of the next period's active QW. In the calculated conduction band profile shown at the bottom of figure 3.4, QW A is the active QW and the cascade consists of QWs B to H.

Analogous to a QWIP, the gain of a QCD is described by (3.1), where p_c is the probability that an electron 'traveling down' the cascade is captured in the next period's

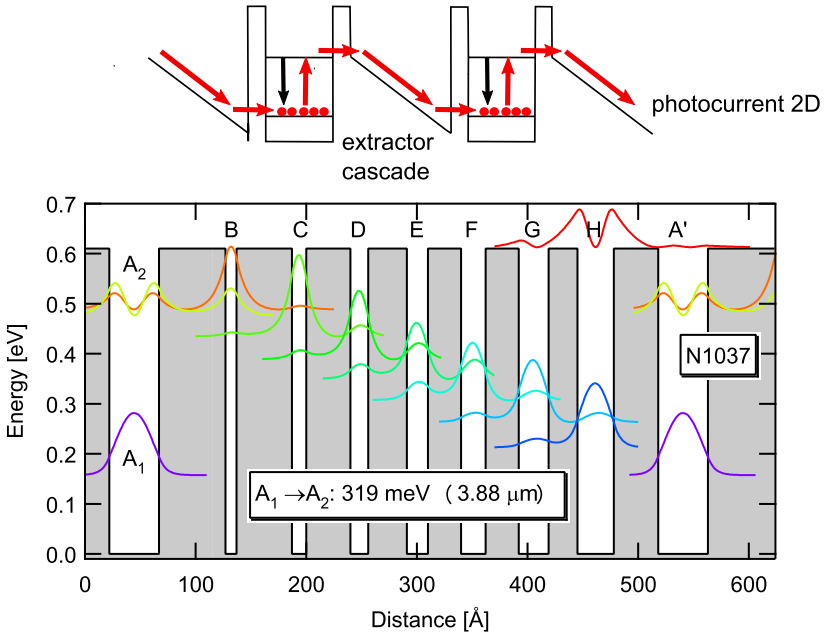

Figure 3.4: Top: schematic of a QCD. Bottom: calculated conduction band profile of QCD N1037 presented in section 7.1. QWs B to H correspond to the extractor cascade shown in the schematic on top.

active QW ground state and p_e is the fraction of photoexcited electrons in the active QW traveling to the next period and not relaxing back into the active QW.

The transport from the active QW into the cascade is ensured through resonant tunneling; this allows for a thick barrier between the active QW and the extractor to reduce the interaction between active QW and intermediate extractor levels, without lowering the escape probability. To achieve an efficient electron extraction through phonon assisted scattering, the energy difference between the individual extractor states should be close to the longitudinal optical phonon energy E_{LO} (GaAs: $E_{LO} = 36\,\text{meV}$, $In_{0.53}Ga_{0.47}As$: $E_{LO} = 32\,\text{meV}$).

For a QCD, p_c is close to unity and p_e is usually around 50%. The gain in a QCD is hence lower compared to a QWIP, where $p_e \approx 1$ and $p_c \ll 1$ is assumed. The advantage of a QCD lies in its photovoltaic operation: Johnson noise dominates, which is generally lower than a QWIPs dark current noise. To get a general idea, the dark current noise i_n^d (2.40) of a (fictive) PC QWIP with dark current $I_d = V_{bias}/R$ is compared to the Johnson noise i_n^J (2.39) of a fictive QCD with the same resistance R. Dividing (2.40) by (2.39) results in $i_n^d/i_n^J = \sqrt{qgV_{bias}/k_BT}$; for a photoconductive gain of $g = 0.5$, a bias voltage of $V_{bias} = 1\,\text{V}$, and a temperature of $T = 77\,K$, the QWIP dark current noise i_n^d is thus 8.7 larger than the QCD Johnson noise i_n^J. Therefore, the Johnson noise limited detectivity of a QCD (2.47) can reach values comparable to or even higher than a QWIPs dark current limited detectivity.

The challenge in QCD design is to maximize $\mathcal{D}^*$ by ensuring a high device resistance (thus a low Johnson noise) without lowering the escape probability and thus the efficiency. The most important design parameters are the layer thicknesses (determining the band

profile discussed above), the doping density n_s of the active QW, and the number of periods N_{QW}.

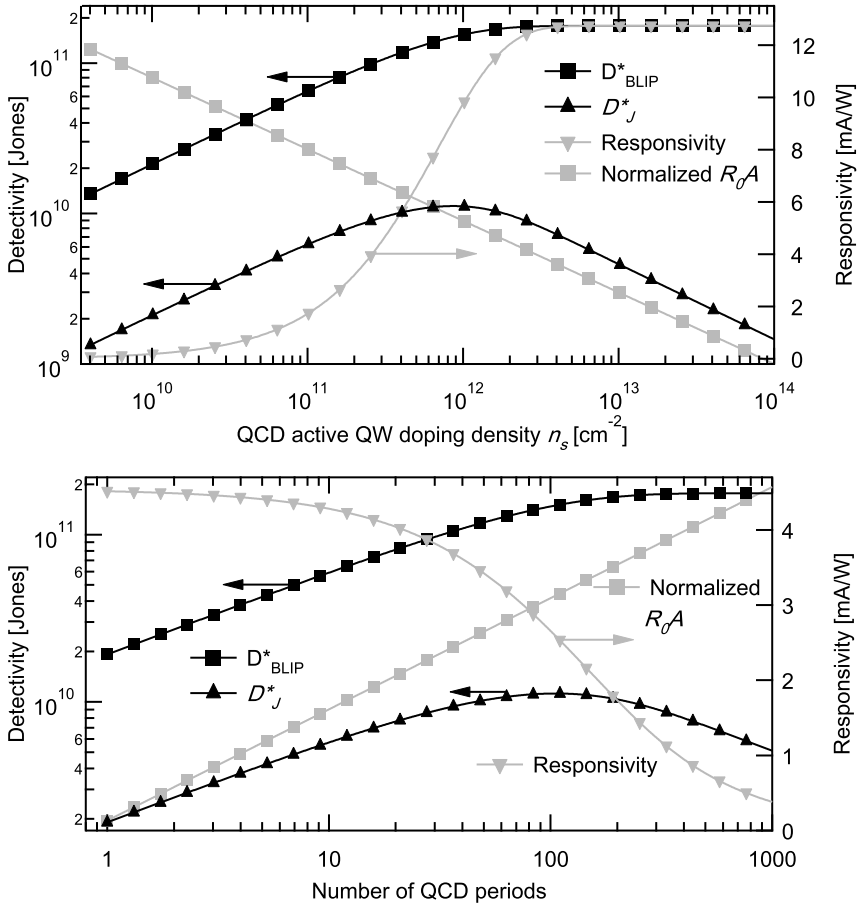

Figure 3.5: QCD detectivity, responsivity, and R_0A for varying doping density and number of periods. The vertical scaling of the normalized R_0A is logarithmic. The calculations are based on the values of QCD N1021 presented in section 6.3.2 at a temperature of 100 K; it has a 45° MPW geometry, 30 periods and a sheet carrier doping density of 2.46×10^{11} cm^{-2} in the active QW.

As long as the absorbance $N_{QW}\alpha_{2D} \ll 1$, so that $\eta = 1 - e^{-N_{QW}\alpha_{2D}} \approx N_{QW}\alpha_{2D}$, the absorption η and thus the responsivity $\mathcal{R}$ are proportional to the doping density n_s (see (2.27) and (2.38)). Looking at (2.48), it follows that the background limited detectivity $\mathcal{D}^*_{BLIP}$ is proportional to $\sqrt{n_s}$. As the device conductance is linear in n_s, the same proportionality $\mathcal{D}^*_J \propto \sqrt{n_s}$ is also true for the Johnson noise limited detectivity $\mathcal{D}^*_J$ (2.47). This does however not imply that n_s should be as high as possible. η cannot become larger than 1 and saturates for high dopings. In the example shown on the top panel of figure 3.5, this starts to be the case at $n_s \approx 2\times10^{11}\,\mathrm{cm}^{-2}$. Therefore, $\mathcal{R}$ and D^*_{BLIP} also saturate, whereas $\mathcal{D}^*_J \propto 1/\sqrt{n_s}$ decreases with a further increase of n_s. The calculated dependencies of $\mathcal{D}^*_J$, $\mathcal{D}^*_{BLIP}$, and $\mathcal{R}$ on n_s for the 7.5 µm QCD N1021 presented in section 6.3.2 are shown on the top panel of figure 3.5.

Assuming again that $N_{QW}\alpha_{2D} \ll 1$ and thus $\eta \propto N_{QW}$, $\mathcal{R}$ is independent on the number of periods N_{QW} and $\mathcal{D}^*_{BLIP}$ increases with $\sqrt{N_{QW}}$. As the device resistance grows linearly with N_{QW}, the same is true for $\mathcal{D}^*_J \propto \sqrt{N_{QW}}$. For large N_{QW}, the aforementioned assumption is not true anymore, η and $\mathcal{D}^*_{BLIP}$ saturate, $\mathcal{R}$ is proportional to $1/N_{QW}$, and $\mathcal{D}^*_J$ is proportional to $1/\sqrt{N_{QW}}$. The calculated dependencies of $\mathcal{D}^*_J$, $\mathcal{D}^*_{BLIP}$, and $\mathcal{R}$ on N_{QW} for N1020 are shown on the bottom panel of figure 3.5.

3.2.3 Optical rectification

Optical rectification, a second order nonlinear process, was proposed as photovoltaic ISB detection mechanism by Rosencher et al. [1989]. The basic idea is that dipoles are created through an electron transition between two states $|\psi_i\rangle, |\psi_f\rangle$ with different centers of gravity $\langle\psi_i|z|\psi_i\rangle \neq \langle\psi_f|z|\psi_f\rangle$. In ISB devices, this asymmetry can be obtained by carefully engineering the band profile.

Figure 3.6 shows two conduction band profiles with such asymmetric states. The left panel displays an InGaAs / InAlAs structure, where the asymmetry is established by an intermediate InAlGaAs layer between QW and barrier. The right panel shows a GaN QW sandwiched between AlN barriers. In a nitride based heterostructure the internal electric fields give rise to an intrinsic conduction band asymmetry. Upon illumination electrons are excited from the ground state $|\psi_1\rangle$ to the first excited state $|\psi_2\rangle$ in the QW, and undergo at the same time a spatial displacement δ_{12}=$\langle\psi_1|z|\psi_1\rangle - \langle\psi_2|z|\psi_2\rangle$. Due to this displacement microscopic dipoles are created between photoexcited electrons and the carriers remaining in the ground state. The summation over all dipoles and all QWs in the active region is the photoinduced polarization, which can be measured as a photovoltage at the terminals of the detector [Rosencher and Bois, 1991, Rosencher et al., 1989]. Optical rectification in GaN / AlN heterostructures was observed by Hofstetter et al. [2007] and Baumann [2007]. In contrast to QWIPs and QCDs, no tunneling or 3D electron transport takes place in

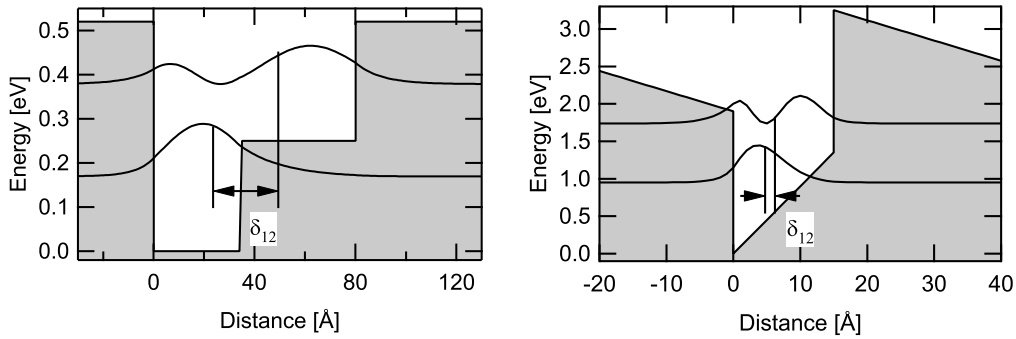

Figure 3.6: Simulation of a InGaAs / InAlGaAs / InAlAs step QW (left) and a GaN QW between AlN barriers (right). The spatial difference between the centers of gravities of $|\psi_1\rangle$ and $|\psi_2\rangle$ is δ_{12}.

an optical rectification photodetector. Its photovoltage is proportional to the number of QWs.

3.2.4 Comparison to other IR photon detectors

In the following, various IR photon detectors are presented and compared to ISB photodetectors. Figure 3.7 shows the spectral detectivity curves for a number of available IR detectors. Besides responsivity and detectivity, also detector geometry, resistance, speed, and costs are important characteristics of IR detectors.

Common semiconductor photon detectors in the mid and near infrared are MCT ($Hg_{1-x}Cd_xTe$) with cut off wavelengths $\lambda_c = 3 - 20\,\mu m$, InAs ($\lambda_c = 3\,\mu m$), InSb ($\lambda_c = 5\,\mu m$), PbS ($\lambda_c = 3.3\,\mu m$), and PbSe ($\lambda_c = 5\,\mu m$). A semiconductor can be doped with specific impurities to detect light at energies below its bandgap; such devices are called extrinsic photodetectors. Based on this technique, the cut off wavelength of Si:As is $\lambda_c = 3 - 24\,\mu m$, and $\lambda_c = 4 - 18\,\mu m$ for Si:Ga; extrinsic detectors must be cooled to temperatures below 20 K and D^* drops to 10^{10} Jones compared to about 10^{13} Jones for intrinsic Si photodiodes. Other extrinsic photodetectors such as Ge:Cu, Ge:Hg, Ge:Au, Ge:Cd, or Ge:Zn, cover the range between 2 µm and 40 µm at working temperatures of 5 K [Wolfe and Zissis, 1985]. The technology of both Si and Ge based extrinsic photodetectors is relatively simple and results in low costs and high yields. Their disadvantages are the low operating temperature, high thermal generation and low quantum efficiency [Rogalski, 2003].

DTGS (deuterated triglycine sulfate, $(ND_2CD_2OOD)_3D_2SO_4$) is a pyroelectric detector sensitive from 1.7 µm up to 28 µm. It exhibits large, spontaneous electrical polarization and its response is hence slow. It is often used as inexpensive broad band detector in spectroscopy when speed and detectivity are of secondary importance.

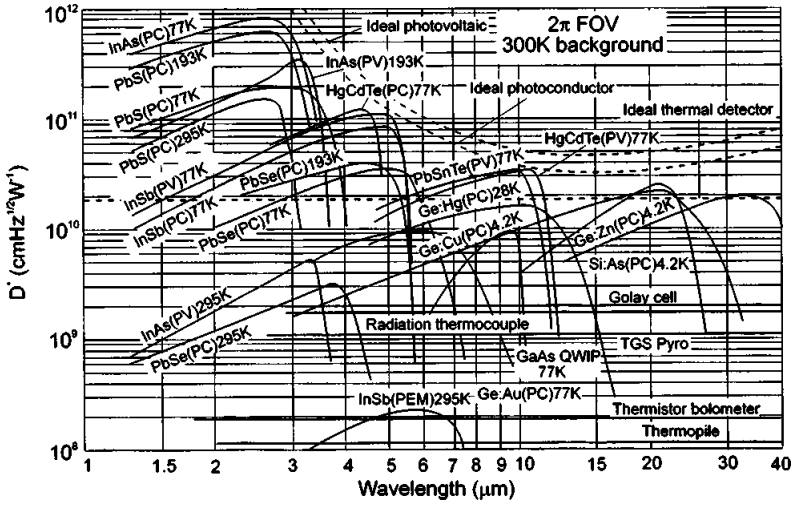

Figure 3.7: Detectivity of various infrared detectors [Rogalski, 2003].

The bandgap of the intrinsic semiconductor photon detector material HgCdTe can be tailored to detect at wavelengths from 1 µm up to 22 µm. It is the most efficient and most often used detector for MIR radiation [Rogalski, 2003]. MCT detectors can be operated in both PV and PC mode and are background limited at a working temperature of 77 K. MCTs are also integrated into linear arrays and focal plane arrays (FPAs). The MCT material however suffers from some disadvantages. The weak Hg-Te bond results in bulk,

surface and interface instabilities. The native defects and compositional inhomogeneity lead to non-uniformity of the detectivity and response wavelength. The high density of Shockley-Read-Hall trap centers causes tunneling leakage and dark currents which are especially critical in FPAs. All this causes high growth and processing costs [Shen, 1993]. Furthermore, MCT is considered a toxic material.

Rogalski [2003] came to the conclusion that in the 8 µm to 15 µm range QWIPs cannot compete with HgCdTe as a single device, as their performance is limited by a lower optical conversion efficiency and a higher dark current. However the large industrial infrastructure in III-V semiconductor growth, device processing and packaging gives the QWIP a potential advantage in producibility and cost. FPAs based on ISB detectors also profit from higher uniformity and hence a lower noise-equivalent temperature difference NEΔT compared to MCT FPAs.

The maximum electrical bandwidth of MCT detectors is about 3 GHz [Rogalski, 2003], whereas intrinsically faster unipolar ISB photodetectors have been demonstrated to detect signals up to 82 GHz [Liu and Li, 1995].

The photovoltaic ISB quantum cascade detectors (QCDs) discussed in this work operate bias less and have thus no dark current, while retaining the high speed and mature material advantages of the QWIP [Hofstetter et al., 2006].

3.3 Simulation

To be able to design ISB devices, it is crucial to have a precise a priori knowledge of energy and wavefunction of electronic states in a heterostructure. This is accomplished by solving the Schrödinger equation (2.4); for simple cases such as the infinite, symmetric QW, it can be solved analytically, but for more complicated structures, numerical simulation is required.

In this work, the numerical Schrödinger solver *calcul-bande* [Faist et al., 2000] was used to calculate the conduction band profile of the semiconductor heterostructures. It is based on the transfer matrix method [Chuang, 1995] and includes band nonparabolicity through an energy dependent effective electron mass using the effective valence band model described in Sirtori et al. [1994]. *calcul-bande* does also allow the introduction of self-consistency with Poisson's equation; for the ISB detector structures presented in this work, self-consistent simulations hardly deviate from simpler Schrödinger simulations due to the structures' low doping, wherefore the conduction band profiles shown in chapters 7 and 6 are not computed self-consistently.

Electronic transport is a crucial characteristic of ISB photodetector structures because it contributes to the device noise and dictates the operating temperature. In a photoconductive QWIP, dark current noise (2.40) is generally dominating. Photovoltaic QCDs are limited by Johnson noise (2.39), which is proportional to the square root of the differential device resistance at 0 V.

Koeniguer et al. [2006] proposed a model for electronic transport in QCDs relying on the calculation of all transition rates between different electron states using an electron-optical phonon Hamiltonian [Ferreira and Bastard, 1989]. To obtain the device resistance, a bias voltage is introduced as a perturbation of the model and the potential drop is

assumed to take place at the interface between two QCD periods. This is justified by calculations which show that the electronic mobility is higher inside a period than between two consecutive periods by several orders of magnitude.

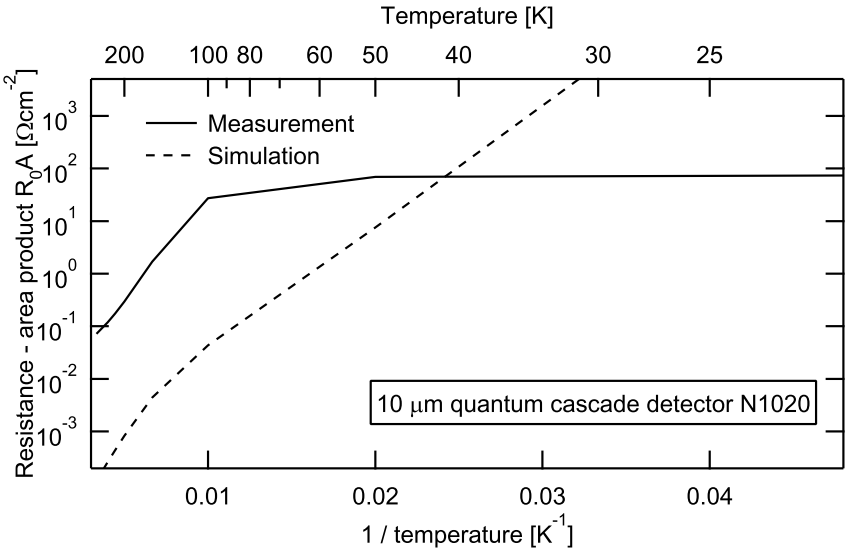

Figure 3.8: Comparison of simulated and measured R_0A of the 10 µm QCD N1020 presented in section 6.3.2.

Figure 3.8 shows the measured resistance - area product R_0A of a QCD detecting at 10 µm (sample N1022 presented in section 6.3.2) as function of inverse temperature. This way of presenting the temperature dependence of a resistance is often referred to as Arrhenius plot in deduction of the Arrhenius equation. The Arrhenius equation describes many thermally excited reactions such as the dependence of a QWIP's dark current I generated by thermionic emission on the temperature T and activation energy E_a :

$$I = e^{-E_{act}/k_bT}. \tag{3.2}$$

If the temperature dependence of the displayed quantity is described by (3.2), the Arrhenius plot is a straight line, and E_a can be extracted from its slope. More complex processes, such as the current transport in a QCD structure, have a superposition of multiple activation energies with temperature dependent weightings.

The measured data is compared to the one calculated with the Koeniguer et al. [2006] model using the wavefunctions simulated with a Schrödinger solver. It is apparent that the measured R_0A is not well described by this model. Especially at low temperatures, additional current leakage paths which lead to a saturation of R_0A are not included in the model. The partial failure of this model was not too harmful for this work: the design accounted for device resistance based on the available data of previous QCDs by taking into account that R_0A increases with thicker and higher barriers and decreases for thicker QWs and higher doping densities.

Chapter 4

Semiconductor Materials for ISB Structures

In this chapter, semiconductor heterostructures used for conduction band ISB devices are discussed and their assets and drawbacks are presented. Besides growth related parameters such as defect density and interface roughness, the most relevant figures are conduction band offset (CBO), effective electron mass, ISB scattering time, and phonon energy. Also, a direct Γ valley transition, lattice matched QWs, barriers, and substrate, and efficient n-doping is favorable. Table 4.1 summarizes the material parameters of the GaAs and InP based material systems used in this work.

	GaAs $Al_xGa_{1-x}As$	$In_{0.53}Ga_{0.48}As$ $In_{0.53}Al_{0.47}As$	$In_{0.69}Ga_{0.31}As$ $In_{0.38}Al_{0.62}As$	$In_{0.53}Ga_{0.48}As$ $AlAs_{0.56}Sb_{0.44}$
CBO [meV]	373 ($x = 0.38$) 982 ($x = 1$, $\Gamma - \Gamma$)	520	730	1015 ($\Gamma - X$), 1600 ($\Gamma - \Gamma$)
m_0	0.067 / 0.15 ($x = 1$), 0.098 ($x = 0.38$)	0.043 / 0.076	0.035 / 0.082	0.043 / 0.125
γ [$10^{18}\,m^{-2}$]	0.49	1.13	1.53	1.13
E_{LO} [meV]	36	32	34	32
a_0[Å]	5.653 / 5.661 ($x = 1$)	5.870 / 5.870	5.936 / 5.814	5.870 / 5.867
Substrate	GaAs (a_0=5.653)	InP (a_0=5.869)	InP	InP

Table 4.1: Conduction band offset (CBO), effective electron mass (m_0), nonparabolicity coefficient γ, LO phonon energy E_{LO}, in plane lattice constant a_0, and substrate material for GaAs / AlGaAs on GaAs as well as for lattice matched InGaAs / InAlAs, InGaAs / AlAsSb, and 1% strained InGaAs / InAlAs on InP taken from Vurgaftman et al. [2001]. For $Al_xGa_{1-x}As$, the mass and CBO towards GaAs is additionally listed for the direct / indirect bandgap crossover point at $x = 0.38$. The CBO of the indirect AlAsSb towards InGaAs is given at the Γ and X point.

Along with the effective electron mass m_0 and the band nonparabolicity coefficient γ which describes the energy dependence of m_0 [Nelson et al., 1987], the CBO dictates the maximal energy separation E_{12}^{max} between the ground and the first excited electron

state in a QW. Figure 4.1 shows E_{12} as function of the QW thickness for the common GaAs / $Al_{0.38}Ga_{0.62}As$ and $In_{0.52}Ga_{0.48}As$ / $In_{0.53}Al_{0.47}As$ systems as well as for strained $In_{0.61}Ga_{0.39}As$ / $In_{0.45}Al_{0.55}As$. The maximal transition energy occurs when the first excited state is close to the continuum. A further decrease of the QW thickness leads to a lower ISBT energy, as the bound ground state shifts towards higher energies whereas the continuum state remains unchanged.

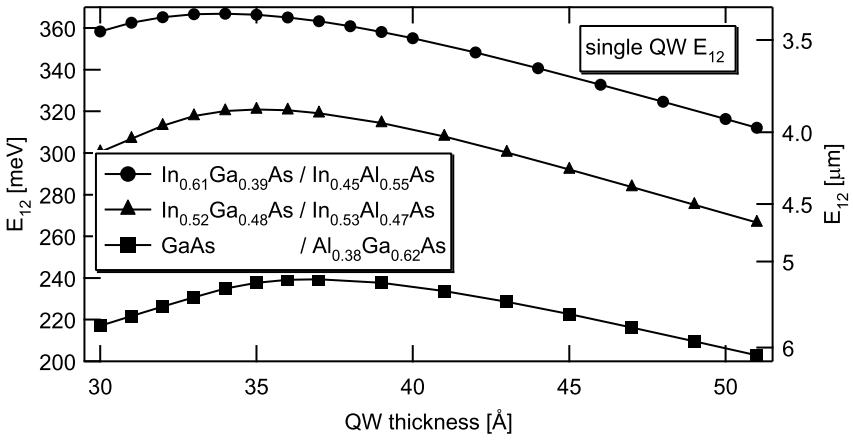

Figure 4.1: Simulated ISB transition energy E_{12} in a single QW as function of QW thickness for GaAs / $Al_{0.38}Ga_{0.62}As$, lattice matched InGaAs, and 0.5% strained $In_{0.61}Ga_{0.39}As$ / $In_{0.45}Al_{0.55}As$.

4.1 GaAs / AlGaAs

GaAs / $Al_xGa_{1-x}As$ is well suited for semiconductor heterostructure growth as the in-plane lattice constant of GaAs ($a_0 = 5.653\,Å$) is very close to the one of AlAs ($a_0 = 5.661\,Å$). This small lattice mismatch, together with readily available GaAs substrates, is one of the reasons for the high quality of GaAs / $Al_xGa_{1-x}As$ growth. The CBO between the GaAs QW and the $Al_xGa_{1-x}As$ barrier can be freely chosen by modifying the barrier Al content x. It is thus not surprising that the first suggestions to use QWs for ISB infrared devices by Esaki and Sakaki [1977] were based on the GaAs / $Al_xGa_{1-x}As$ material system. The first experimental reports on ISB absorptions in a QW system by Smith et al. [1983] and Chui et al. [1983] and the first QWIP demonstrated by Levine et al. [1987] were GaAs / $Al_xGa_{1-x}As$ structures. (Al)GaAs is commonly used in interband optoelectronic devices such as laser diodes, LEDs, and photodiodes in the near infrared and red. On a smaller scale, it is the material of choice for commercial QWIP cameras.

The CBO between GaAs and AlAs amounts to 0.982 eV, but whereas GaAs is a direct-gap material with $\Gamma - L - X$ valley ordering, $Al_xGa_{1-x}As$ becomes an indirect material with the reverse ordering for $x > 0.39$. This fact is unfavorable to ISB photodetectors with high barrier Al content $x > 0.38$. Γ−X intervalley scattering together with X valley trapping in the GaAs QW result in less efficient carrier collection and lower responsivity. Also, the energy crossing of the QW Γ valley and $Al_xGa_{1-x}As$ barrier X valleys at $x > 0.38$ reduces the thermal activation energy of the ground state electrons and thus the resistivity,

which again reduces the detector sensitivity [Choi et al., 2002]. Nevertheless, Levine et al. [1991] successfully demonstrated a GaAs / $Al_{0.55}Ga_{0.45}As$ indirect bandgap QWIP detecting around 4.2 µm (295 meV).

The CBO between GaAs and AlGaAs can be further increased by adding In to the GaAs QW. This comes however at the cost of introduced strain due to the larger lattice constant of the QW material. In a study on ISBTs in $In_yGa_{1-y}As$ / $Al_xGa_{1-x}As$ heterostructures, Chui et al. [1994] demonstrated ISBTs at wavelengths down to 2.1 µm (up to 580 meV) for $y = 0.6$ and $x = 1$, and Smet et al. [1994] reported on an ISBT wavelength of 1.55 µm (800 meV) for a 3 ML $In_{0.53}Ga_{0.47}As$ / AlAs single QW.

4.2 InGaAs / InAlAs

Soon after the first GaAs / $Al_xGa_{1-x}As$ ISB devices, such structures were realized with $In_{0.53}Ga_{0.47}As$ QWs and $In_{0.52}Al_{0.48}As$ barriers grown lattice matched on an InP substrate. Levine et al. [1988] were the first to report on ISBTs in this material system; they measured the absorption of a MQW structure which peaked at a wavelength of 4.4 µm (281 meV).

The effective electron mass of $In_{0.53}Ga_{0.47}As$ is 36% lighter compared to the one in GaAs. Due to the inverse dependency between ISB absorption efficiency and effective electron mass (see (2.27)), an $In_{0.53}Ga_{0.47}As$ QW has a stronger absorption compared to a GaAs QW with similar ISBT energy and doping density. The light mass also results in comparatively thick QW thicknesses for a given ISBT energy which facilitates the growth of short wavelength ISB structures.

As seen in figure 4.1, the CBO of 520 meV allows for a separation between a QW's ground and first excited state of up to 320 meV (corresponding to a wavelength of 3.88 µm). A larger CBO can be obtained by increasing the In content of the InGaAs QW above 53% and lowering the In content of the barrier below 52% such that the pseudomorphic lattice constant of the strained InGaAs / InAlAs heterostructure equals the InP lattice constant. Assuming equally thick QWs and barriers, an 1% lattice mismatch towards the InP buffer corresponds to $In_{0.69}Ga_{0.31}As$ and $In_{0.38}Al_{0.62}As$ and results in a CBO of 740 meV. Lai et al. [2004] studied ISB absorption in $In_{0.84}Ga_{0.16}As$ / AlAs / $In_{0.52}Al_{0.48}As$ heterostructures in the $2-7$ µm wavelength range and a quantum cascade laser based on strain compensating InGaAs / InAlAs / AlAs operating at 3.05 µm was reported by Semtsiv et al. [2007].

4.3 InGaAs / AlAsSb

$In_{0.53}Ga_{0.47}As$ / $AlAs_{0.56}Sb_{0.44}$ heterostructures offer a high CBO of 1.6 eV [Georgiev and Mozume, 2001], which makes them a promising candidate for short wavelength ISB devices. They are also lattice matched to the high quality, low cost InP substrates; the InP substrate allows for standard processing and waveguide designs. Similar to $Al_{x>0.39}Ga_{1-x}As$, $AlAs_{0.56}Sb_{0.44}$ is an indirect semiconductor with its X valley minimum 789 meV below the Γ valley minimum [Vurgaftman et al., 2001]. This reduces the efficiency of ISB devices as discussed above for the GaAs / $Al_xGa_{1-x}As$ material system. Although calculations yield a maximal ISBT energy E_{12}^{max} of 920 meV, the highest E_{12}^{max} obtained experimentally is 636 meV only [Neogi et al., 2000]; the discrepancy between experiment and simulation is attributed to interface diffusion between the InGaAs QW and the AlAsSb barrier, result-

ing in a graded QW potential and thus a redshift of the ISBT [Cristea et al., 2006]. Also, MBE growth of AlAsSb is complicated by the large miscibility gap of AlAsSb and the difficulties in growing alloys with different group V elements [Cristea et al., 2005].

Revin et al. [2007] demonstrated an $In_{0.53}Ga_{0.47}As$ / $AlAs_{0.56}Sb_{0.44}$ quantum cascade laser operating at 3.05 µm. In this work, $In_{0.53}Ga_{0.47}As$ / $AlAs_{0.56}Sb_{0.44}$ quantum cascade detectors operating at 2.2 µm and 2.5 µm will be presented in section 7.2.

4.4 Group III nitrides

In the hexagonal wurtzite phase, the group III nitrides AlN, GaN, and InN form a continuous alloy system with direct bandgaps. The large bandgap difference of 2.72 eV at 300 K between GaN and AlN [Vurgaftman and Meyer, 2003], results in a large CBO of 1.89 eV [Bernardini and Fiorentini, 1998]. This makes GaN / AlN heterostructures a promising candidate for ISB devices in the NIR. Figure 4.2 shows the ISBT energy E_{12} as function of the QW thickness t_{QW} for a GaN QW and AlN barriers. It is seen that theoretically the ISBT energy lies above 1 eV for $t_{QW} = 7.8$ Å.

However, there is still relatively little known about group III nitrides compared to other III−V semiconductors [Strite and Morkoç, 1992]. The lattice mismatch between GaN (a_0^{GaN}=3.189 Å), AlN (a_0^{AlN}=3.112 Å) and the commonly used sapphire substrate (a_0^{sap} = 2.748 Å) introduces a strain dependent piezo electric polarization in addition to the spontaneous polarization present in wurtzite crystals. The combined polarizations give rise to internal fields and complicate the design of group III nitride MQW structures. Despite the continuous progress in nitride growth technology, the defect density lies in the range of $10^9\,cm^{-2}$. Due to the high effective masses $m_0^{GaN} = 0.2$ and $m_0^{AlN} = 0.4$ respectively [Levinshtein et al., 2001] thin QWs are required to achieve high ISBT energies; the heavy m_0 further results in low tunneling probabilities through AlN barriers. On the other side, the high m_0 strengthens the electron-phonon coupling, which results in short ISB scattering times $\tau_{scatter} \approx 370\,fs$ [Heber et al., 2002] compared to $\tau_{scatter} \approx 1$ ps in GaAs and InP based devices. Group III nitride devices therefore offer a potential for high speed optoelectronic applications in the NIR.

Iizuka et al. [2002] measured ISB absorption down to a wavelength of 1.3 µm (corresponding to 954 meV) in GaN / AlN heterostructures. ISB emission at 2.3 µm originating from a second harmonic generation process was observed by Nevou et al. [2007]. Doyennette et al. [2005] reported on a quantum dot detector working around 1.38 µm and there are several reports on ISB detectors operating at 1.5 µm, for example by Baumann et al. [2006], Giorgetta et al. [2007a], Hofstetter et al. [2003] or Hofstetter et al. [2007].

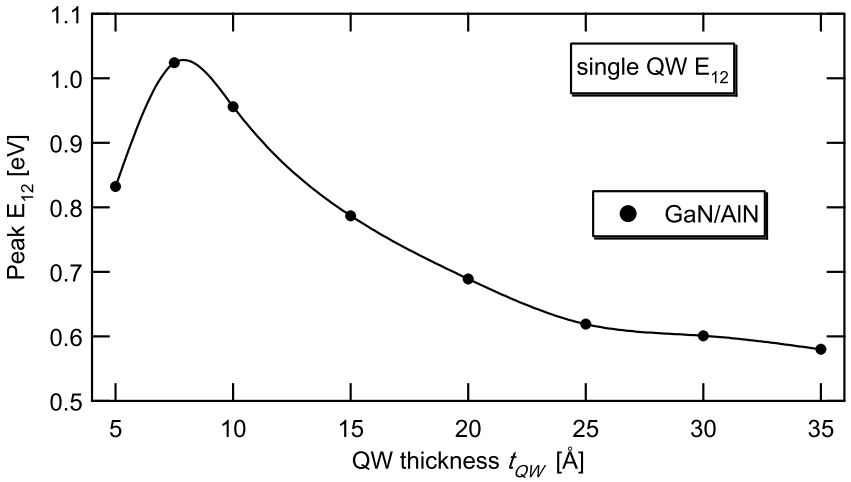

Figure 4.2: Simulated ISB transition energy E_{12} as function of QW thickness t_{QW} for a GaN QW sandwiched between AlN barriers, the line is a guide to the eye. The highest theoretical ISBT energy lies above 1 eV for $t_{QW} = 3$ ML. A further decrease of t_{QW} results in an decrease of the ISBT energy since the second electronic state lies in the continuum.

4.5 Others

InAs / AlSb is one of the candidates for short wavelength ISB devices due to its large CBO of 2.1 eV. Ohtani et al. [2003] observed ISB absorption at 625 meV (1.98 µm) for a 2.7 nm InAs QW sandwiched between two AlSb barriers. This system is however less mature than the established InGaAs / InAlAs and GaAs / AlGaAs systems: complications arise from the fact that both the group III and V elements change at each interface. Also, when grown on InAs substrates, the strain introduced by the AlSb barriers can not be compensated, limiting the maximal thickness of the active region. Marcadet et al. [2007] proposed to replace the AlSb barriers with AlAsSb to alleviate those drawbacks.

Substituting a few percent of N in an InGaAs QW layer grown on GaAs (so called dilute nitride QWs) significantly reduces the strain in the layer. It also reduces the QW band gap energy due to bowing effects, wherefore long wavelength interband lasers emitting at 1.3 µm and 1.5 µm can be realized with diluted nitride QWs. ISB absorption from a InGaNAs QW was measured by Duboz et al. [2002] at 124 meV (10 µm). Liu et al. [2006] reported on ISB absorption around 155 meV (8 µm) in $Ga_{0.77}In_{0.23}N_{0.01}As_{0.99}$ / GaAs MQW structures.

The wide bandgap II−VI material $Zn_xCd_{1-x}Se$ / $Zn_{x'}Cd_{y'}Mg_{1-x'-y'}Se$ can be grown lattice matched to InP. Its relatively high CBO of 1.12 eV makes it a candidate for room temperature QCLs emitting at wavelengths below 4 µm. ISB absorptions in $Zn_{0.46}Cd_{0.54}Se$ QWs sandwiched between $Zn_{0.24}Cd_{0.25}Mg_{0.51}Se$ barriers were reported by Lu et al. [2006] to lie at 3.99 µm and 4.99 µm for QW thicknesses of 28 Å and 42 Å respectively.

Akimoto et al. [2001] proposed the II−VI ZnSe / BeTe system lattice matched to GaAs offering a CBO of 2.6 eV and studied ISBTs therein using photoinduced absorption measurements; for a QW thickness of 4.5 ML, an ISBT energy of 775 meV (1.6 µm) was observed.

ISB devices with InAs, InGaAs, and GaAs QWs are impeded to emit light in the $30 - 60\,\mu m$ wavelength range, were those materials have strong phonon absorption. An alternative is the GaP / AlP system which has its phonon absorption band at lower wavelengths ($20 - 28\,\mu m$). Complications in this system arise from the strain between GaP and AlP and the indirect bandgap of AlP. Semtsiv et al. [2006] measured absorption of GaP / AlP ISB structures. Based on the measured absorption between the ground and the third excited electron state, they concluded that the $1-2$ ISBT lies in the 30-60 μm range.

Chapter 5

Experimental Methods

The first part of this chapter describes the sample processing steps required to characterize the devices presented in this work. In the second part, the measurement setups used for absorption and photosignal characterization are presented.

5.1 Sample preparation and mount

This section describes the sample preparation and mounting required to measure the optical absorption as well as photosignals.

First, the Indium used to attach the wafer to the MBE holder was removed either by mechanical grinding or by chemical wet etching via dipping the wafer into HF:H_2O:H_2O_2 (1:5:6) for about 20 minutes. Then, smaller pieces of roughly $6 \times 6\,\mathrm{mm}^2$ were cleaved from the 2" wafer so that first, multiple processes can be done on the same growth run and second, only little material is lost if a process goes awry.

For photosignal measurements, samples were first degreased with acetone and isopropanol. Then, mesas were etched and metal contacts deposited as shown in figure 5.1. The individual process steps are listed below labeled according to figure 5.1.

a Spin deposition of photoresist (AZ1518), 1' 110°C softbake.

b 10" photoresist exposure with etch mask using a Karl Süss MJB-3 mask aligner followed by a 30" dip into AZ351B:H_2O (1:3) developer to dissolve the exposed photoresist.

c Wet etching through top contact layer and active region down to the bottom contact layer using H_3PO_4 (85%) : H_2O_2 (38%) : H_2O (1 : 4 : 1), etch rate in InGaAs / InAlAs is roughly 30 nm/s.

d Photoresist removal with acetone / isopropanol.

e Spin deposition of photoresist (AZ1518), 1' 110°C softbake.

f Photoresist exposure and development (as in [b]) with metalization mask.

g Deposition of a metallic contact (Ti/Au/Ge/Ti/Au, 2/25/50/10/250 nm) using an Edwards EB3 E-gun evaporator.

h Metal liftoff: remove metal above photoresist by first swelling the photoresist at 80 ° in a 1-Methyl-2-Pyrrolidone : Ethylene Glycol (1:1) bath for 120', followed by a 2' ultrasonic bath in acetone.

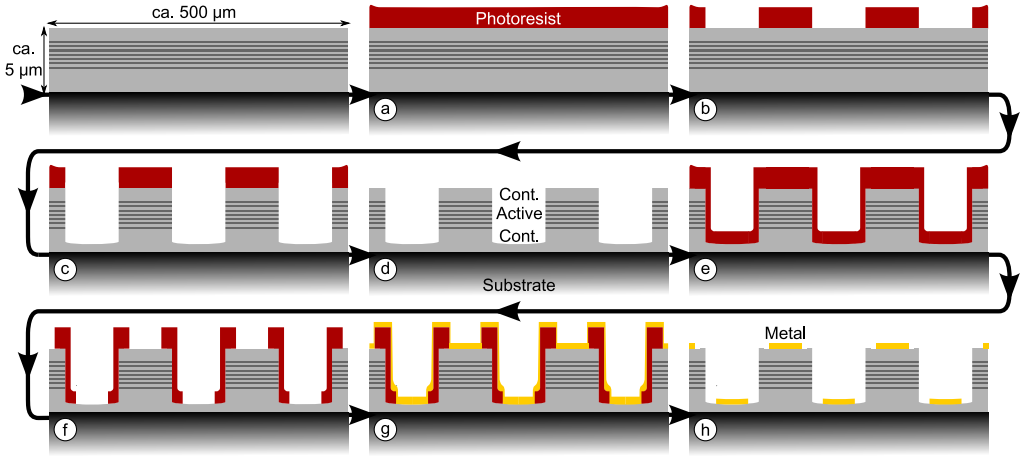

Figure 5.1: Schematic lateral view of the photolithography process. Vertical dimensions are about 25 times inflated.

After polishing a 45° wedge the processed sample is glued with varnish to a $19\times7\times1.5\,\mathrm{mm}^3$ copper submount. The mesa and ground metalizations are then wire bonded to gold coated ceramic pads also glued on the submount using a manual WestBond 7400A-66A wire bonder. Figure 5.2 shows photographs of a mounted absorption sample with unprocessed surface and a mounted photosignal sample with its surface processed as discussed above.

Figure 5.2: Sample pictures. Left: mounted absorption sample. Center: mounted photocurrent sample. The small ceramic pad chip between the two signal contact pads connects a bond from the sample ground to the copper submount by an indium film. The 45° facet is below the long top sample edge. Right: close-up of the mounted photocurrent sample. The ground (bottom) and mesa (top) contact wires are clearly visible. The square mesas have side lengths of 100 µm, 200 µm, and 300 µm.

For absorption measurements, samples were polished into the 45° MPW waveguide described in section 3.1 using an Allied OptiPrep™ polishing machine. First the sample backside (substrate side) was polished to ensure good reflectivity at this interface, followed by two parallel 45° facets on opposing sample edges. The surfaces were polished down to a grit size of 1 µm, resulting in a surface roughness below the optical free space operating wavelength for all devices presented in this work. Using varnish the absorption sample was finally glued to a copper submount adapted to the cryostat sample holder.

5.2 Spectroscopic measurements

Spectroscopy is the study of the interaction between electromagnetic radiation and matter. This section gives a short overview of the electromagnetic spectrum (henceforth called spectrum) and describes the measurement setup used in this work to spectrally characterize devices.

The spectrum is composed of electromagnetic waves which are characterized by their frequency. Figure 5.3 shows the common partition of a part of the spectrum as function of frequency ν in Hz, free space wavelength λ_0 in µm, energy E in eV, and wavenumbers w in cm^{-1}. The relations between these units are

$$\lambda_0\,[\mu\mathrm{m}] = \frac{c_0}{\nu} = \frac{c_0 \times h}{E} = \frac{1.240...}{E} = \frac{10000}{w} \qquad (c_0 = 2.998... \times 10^{14}\,\mu\mathrm{m/s}) \quad (5.1)$$

$$E\,[\mathrm{eV}] = h\nu = \frac{1.240...}{\lambda_0} = \frac{1.240... \times w}{10000} = \frac{w}{8065...} \qquad (h = 4.136... \times 10^{15}\,\mathrm{eV\,s}) \quad (5.2)$$

$$w\,[\mathrm{cm}^{-1}] = \frac{10000 \times \nu}{c_0} = \frac{10000}{\lambda_0} = 8065... \times E \quad (5.3)$$

$$\nu\,[\mathrm{Hz}] = \frac{c_0}{\lambda_0} = \frac{E}{h} = \frac{w \times c_0}{10000}, \quad (5.4)$$

where c_0 is the vacuum speed of light and h Planck's constant. λ_0 is commonly used to describe radiation close to the visible part of the spectrum; electron volts (eV) are an energy unit widely used in solid state, atomic, nuclear, and particle physics. $1\,\mathrm{eV}{=}1.60... \times 10^{19}\,\mathrm{J}$ corresponds to the energy an electron with charge $e = 1.60... \times 10^{19}\,\mathrm{C}$ gathers when it is accelerated across a potential difference of 1 V. Wavenumbers are the inverse of wavelength and are commonly used in mid infrared spectroscopy. Although strictly speaking, the unit of wavenumbers is inverse length, it is thought of as energy unit. Spectroscopic results in this work are presented in wavenumbers [cm^{-1}], electron volts [eV] and wavelength [µm].

In this work, radiation absorption and the thereby generated electric signal in semiconductor structures was studied. Spectral measurements were performed with a Bruker IFS66 Fourier Transform Infrared Spectrometer (FTIR), which is commonly used in the investigated radiation wavelength range of $2\,\mu\mathrm{m}{-}17\,\mu\mathrm{m}$. The working principle of an FTIR as shown in figure 5.4 is based on an Michelson interferometer. Radiation from a source (in this case a silicon rod heated to about 1460° C, a so called glowbar) is split into two beams by a beamsplitter (in this case a KBr beamsplitter); one beam is reflected off a fixed mirror and one off a moving mirror. The intensity of the two superimposed beams is recorded by a photodetector at different discrete mirror positions; the thus obtained signal is the autocorrelation of the light and is called interferogram. According to the Wiener Khintchine theorem, the power spectral density of the light is then obtained by Fourier transforming the interferogram.

ISB absorption in this work was measured in the MPW geometry discussed in section 3.1.The sample, attached to a cryostat's copper finger, is placed into the optical path of the FTIR spectrometer as shown in figure 5.4. The light exiting the sample through the second 45° facet is collected and focused onto a photodetector. This measurement is conducted with TM and TE polarized light (set by the polarizer depicted in figure 5.4). By dividing the sample spectra with the background spectra collected under identical

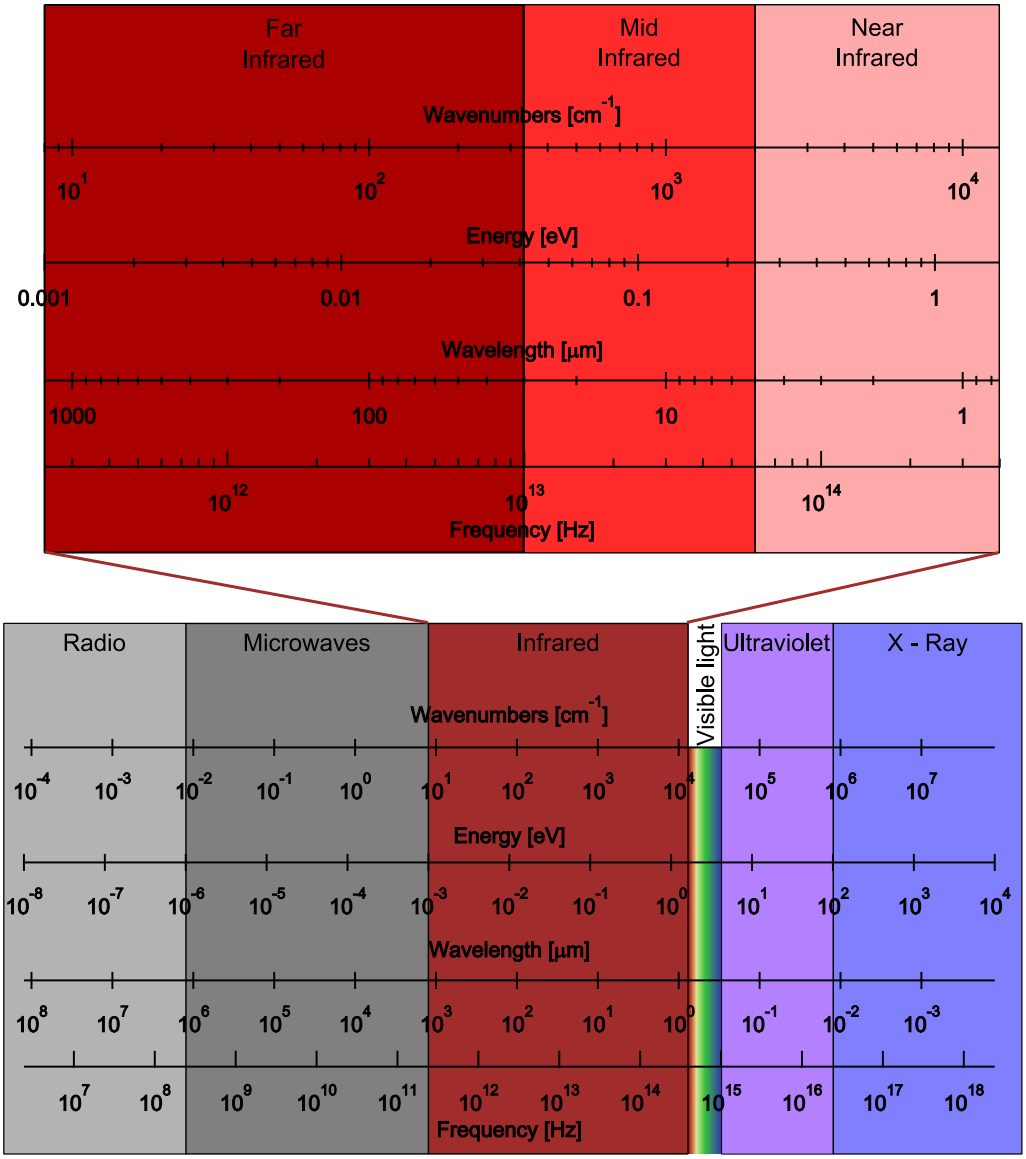

Figure 5.3: Electromagnetic spectrum shown from X-rays down to radio frequencies as functin of wavenumbers, energy, wavelength and frequency. A more detailed close up of the infrared is shown on the top. The division of the infrared spectrum in near- (NIR, visible–5 µm), mid- (MIR, 5–30 µm), and far- (FIR, 30–1240 µm) infrared corresponds to the astronomical convention.

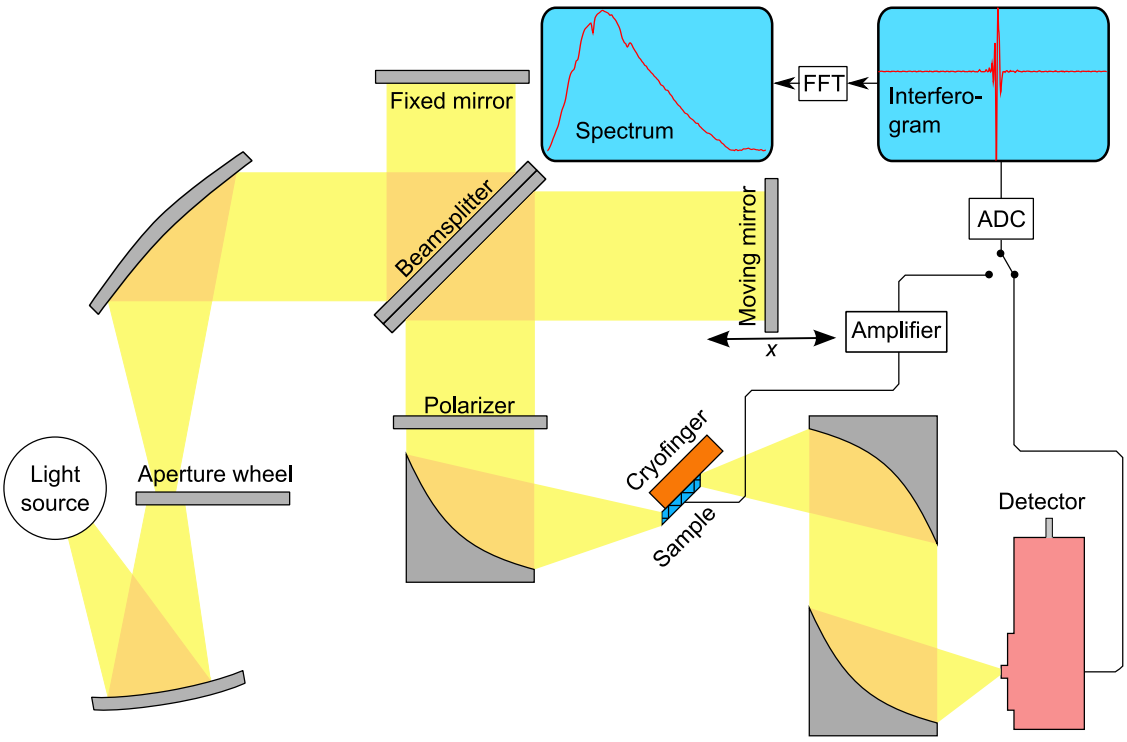

Figure 5.4: Schematic of a FTIR spectrometer as used in this work. The light exiting the spectrometer is focused on the sample. For transmission measurements, it is recollected behind the sample and focused on a detector; the detector signal is then digitized by the spectrometer's analog to digital converter (ADC) and Fourier transformed to obtain a spectrum. For photosignal measurements, the sample itself serves as detector.

conditions, the sample transmission spectra $T_S^{TM}(w)$ and $T_S^{TE}(w)$ are obtained. According to the polarization selection rule (2.20), only TM polarized light interacts with ISBTs, wherefore the ISB absorbance $\alpha_{ISB}(w)$ is given by

$$e^{-\alpha_{ISB}} = \frac{T_S^{TM}}{T_S^{TE}}, \quad \alpha_{ISB} = \ln\left(\frac{T_S^{TE}}{T_S^{TM}}\right), \tag{5.5}$$

$$\alpha_{ISB} = n_p \times N_{QW} \times \alpha_{2D} \times 2^{-0.5}, \tag{5.6}$$

where n_p is the number of passes of the light through the active region, N_{QW} is the number of QWs, α_{2D} is the ISB absorbance of a single QW as calculated in (2.27), and $2^{-0.5} = \sin^2 45°/\cos 45°$ is the geometry factor described in section 3.1.

For photocurrent measurement, the sample acts as detector for the FTIR. The electric signal coming from the sample is amplified by a Stanford Research SR570 low noise current amplifier and fed back into the ADC of the IFS66 spectrometer as shown in figure 5.4. To obtain the responsivity, the measured photocurrent density spectrum $J_S(w)$ is divided by the power density spectrum $P_l(w)$ of the light impinging on the sample.

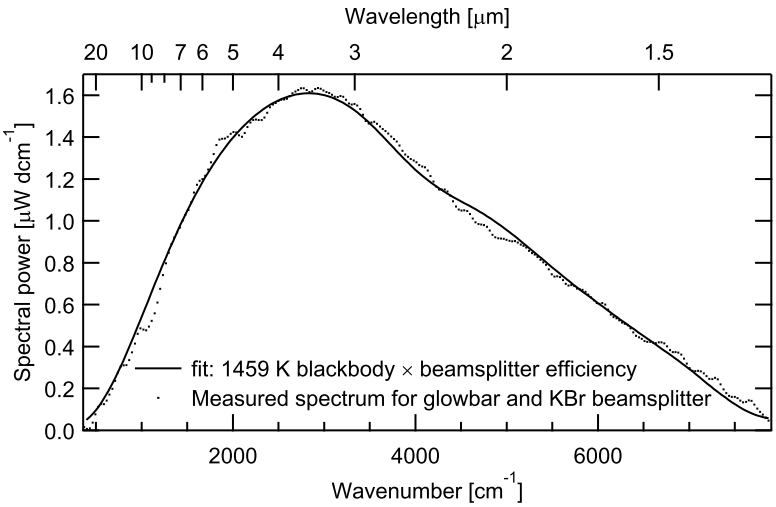

Figure 5.5: Measured power spectrum of the FTIR's glowbar in conjunction with the KBr beamsplitter (dotted line). The solid line is the product of blackbody emissivity and KBr efficiency fitted to the power spectrum.

$P_l(w)$ was obtained by measuring a background spectrum with an Ophir LaserStar power meter with a flat spectral response. Figure 5.5 displays the measured $P_l(w)$ along with a fit by the product of a blackbody emissivity and the KBr beamsplitter efficiency; the thus obtained glowbar temperature is 1459 K. To determine the total power impinging on the sample, the spatial intensity distribution at the sample's position in the plane perpendicular to the optical path was measured. Figure 5.6 shows the measured light intensity of the focal spot for an internal aperture of 3 mm. The data was obtained by translating a photodetector in the focal plane and measuring its response as function of x and y. The fraction M of the total light power collected by an optimally placed square

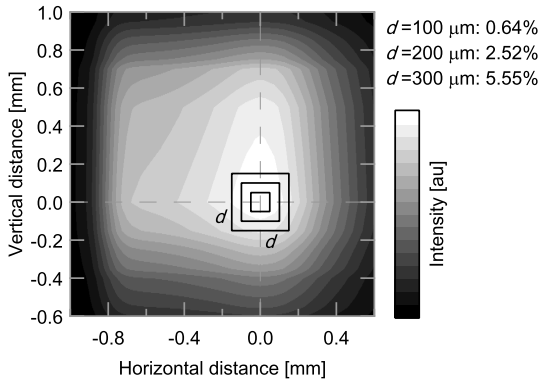

Figure 5.6: Focal spot intensity measured using a 3 mm internal aperture of the IFS 66 spectrometer. The area indicated by the side length d visualizes the position of mesas with different sizes. A $(100\,\mu\text{m})^2$ mesa collects 0.64% of the spot energy, a $(200\,\mu\text{m})^2$ mesa 2.52%, and a $(300\,\mu\text{m})^2$ mesa 5.55%.

mesa photodetector with side length d is 0.64% for $d = 100\,\mu$m, 2.52% for $d = 200\,\mu$m, and 5.55% for $d = 300\,\mu$m. Using the glowbar source and KBr beamsplitter with a 3 mm aperture, the integrated spot intensity equals 4.25 mW, wherefore 107 µW impinge on an optimally positioned $(200\,\mu\text{m})^2$ photodetector.

Finally, the responsivity $\mathcal{R}(w)$ is given by

$$\mathcal{R}(w) = \frac{I_s(w) \times Amp}{P_l(w) \times M}, \tag{5.7}$$

where $I_s(w)$ is the measured photocurrent spectrum in $A\,\text{dcm}^{-1}$, Amp is the amplification of the current amplifier in V/A (typically 10^{-6} V/A), $P_l(w)$ is the power spectrum in $\text{W}\,\text{dcm}^{-1}$, and M is the fraction of $P_l(w)$ collected by the detector.

To characterize devices at temperatures between 5 K and 320 K, the samples were placed in a Janis liquid Helium flow cryostat. The transmission of the Cryostat window, which consisted of either ZnSe or quartz, was taken into account for the presented absorption and responsivity spectra.

Finally, the electrical conductivity of the devices was characterized by measuring the current while sweeping the applied voltage (so called $I - V$ measurements).

Chapter 6

Mid Infrared Detectors

As shown in figure 5.3, mid infrared radiation encompasses wavelengths from 5 µm to 30 µm; there are various photodetector applications in this spectral range. Heat seeking of hot targets such as aircraft engine exhaust plumes takes place between 3 µm and 8 µm. Sensitive ISB detectors with a narrow linewidth can be an interesting choice to determine the amount of certain molecules or atoms in gases and liquids by measuring their characteristic absorption lines. A potential application for fast MIR photodetectors is heterodyne spectroscopy, which allows to distinguish spectrally close absorption lines due to its high resolution but requires an electrical detector bandwidth in the GHz range. Thermal imaging in the MIR is of general interest as the emission of a room temperature black body peaks at 10 µm. Cameras detecting around 10 µm with a low noise equivalent temperature difference are thus commonly used in construction to detect thermal bridges, in fire protection to pinpoint pockets of embers, as well as in various security and military applications such as missile detection. In medicine, the method of dynamic area thermometry has been introduced for breast cancer detection based on the detection of subtle temporal changes of the skin temperature [Fauci et al., 2001].

In this chapter, ISB detectors sensitive at wavelengths between 4.7 µm and 17 µm (71 meV − 260 meV) are presented. Except for a GaAs / AlGaAs QWIP, all investigated samples consist of $In_{0.52}Ga_{0.48}As$ QWs and $In_{0.53}Al_{0.47}As$ barriers lattice matched to the InP substrate. This material system allows for ISBTs at wavelengths down to 4 µm and benefits from a high maturity.

6.1 Bound to bound QWIP

The first device presented in this work is a bound to bound (B2B) state QWIP, as first demonstrated by Levine et al. [1987] and presented in section 3.2.1; the aim of this section is thus not to present a novel device but rather to discuss a well established ISB photodetector design so that the ISB detectors discussed later in this work can be compared to a standard device with an identical process and characterization setup.

A bound to bound QWIP consists of QWs isolated from each other by thick barriers. The GaAs QW thickness and $Al_xGa_{1-x}As$ barrier Al content x is chosen such that the upper bound state is close to resonance with the conduction band edge of the barrier. The energy spacing between the two bound electronic states corresponds to the detection

wavelength.

The active region of the B2B QWIP N64 consists of 100 repetitions of a 66 Å thick GaAs QW n-doped to $2.27 \times 10^{18}\,\mathrm{cm}^{-3}$ and a 250 Å $Al_{0.2}Ga_{0.8}As$ barrier and is sandwiched between two GaAs contact layers n-doped to $2 \times 10^{18}\,\mathrm{cm}^{-3}$. This structure was grown by MBE on a GaAs substrate.

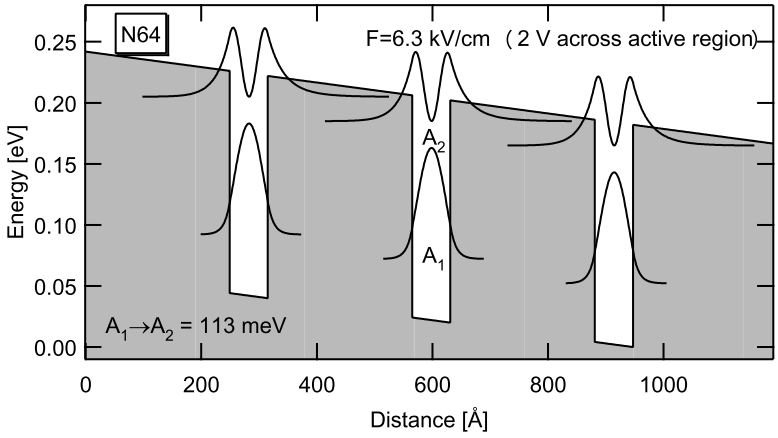

Figure 6.1: Simulated bandstructure of the bound to bound QWIP N64 designed for a detection energy around 113 meV (11 µm). The figure shows 3 out of 100 periods for an applied voltage of 2 V, corresponding to an electric field of 6.3 kV/cm.

The bandstructure obtained with a Schrödinger solver using a CBO of 0.182 eV [Vurgaftman et al., 2001] and an effective barrier mass of 0.836 obtained by linear interpolation between GaAs and AlAs is shown in figure 6.1. There are two bound states, A_1 and A_2, in the QW separated by a transition energy of 113 meV corresponding to a detection wavelength of 11 µm; at zero bias, the excited state A_1 lies 19 meV below the $Al_{0.2}Ga_{0.8}As$ barrier conduction band edge.

For current responsivity measurements, $(200\,\mu\mathrm{m})^2$ mesas were processed onto the sample, a 45° facet was polished below the mesas, and the sample was mounted and connected as described in section 5.1. Current responsivity spectra were taken with a Fourier transform infrared spectrometer (FTIR) as described in section 5.2. Figure 6.2 shows the measured current responsivity of N64 at 5 K as function of applied bias voltage.

For non-zero bias voltages V_b, the 5 K responsivity $\mathcal{R}$ shown in figure 6.2 peaks at $970\,\mathrm{cm}^{-1}$ (120 meV / 10.3 µm). Compared to the simulated $A_1 \rightarrow A_2$ transition energy of 113 meV, the responsivity peak is thus blueshifted by 6%. This discrepancy is explained by a deviation of the actual layer thicknesses from the nominal values: the actual thickness of one QW / barrier period extracted from x-ray measurements amounts to 289 Å, which is 9% thinner than the nominal period. Simulating N64's conduction band profile shortened by 9% results in a $A_1 \rightarrow A_2$ transition energy of 118 meV, which is in reasonable agreement with the measured 120 meV. The responsivity shoulder at $1200\,\mathrm{cm}^{-1}$ (149 meV) is caused by a bound to continuum transition and results in conjunction with transitions from the bound ground state A_1 to higher lying continuum states into an asymmetric responsivity shape with a high energy tail.

$\mathcal{R}$ increases monotonically with V_b and amounts to 120 mA/W at $970\,\mathrm{cm}^{-1}$ for $V_b =$

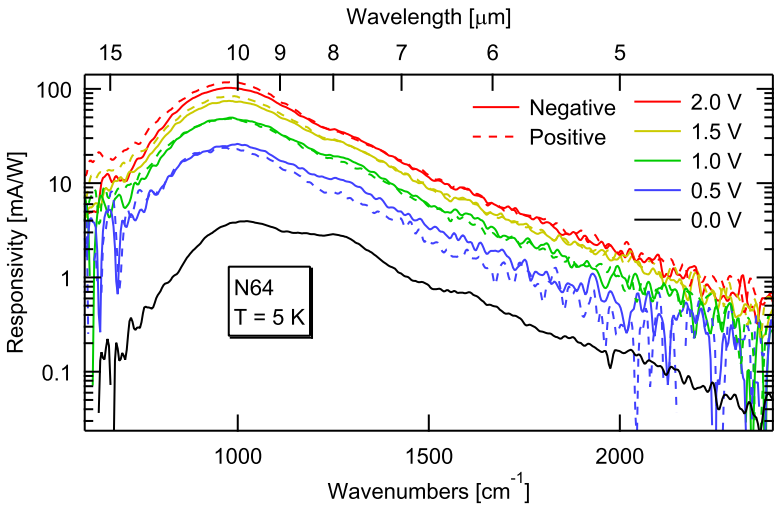

Figure 6.2: Measured responsivity of the B2B QWIP N64 at 5 K for bias amplitudes between 0 V and 2 V. Dashed lines are measured with negative bias, solid lines with positive bias.

2 V. As seen in figure 6.2, the lineshape is not affected by the bias amplitude and $\mathcal{R}$ is identical for opposite bias polarities. At $V_b = 0$ V, a perfectly symmetric B2B QWIP would result in $\mathcal{R} = 0$ mA/W. N64 however shows a weak zero-bias responsivity of 4 mA/W at 5 K. This indicates a slight asymmetry in the structure, such as a sloped doping profile caused by a drift in the Si evaporation rate during growth and layer interface asymmetries above and below each active QW A, which leads to a preferential transport direction of excited electrons even at $V_b = 0$ V. Non-vanishing zero-bias $\mathcal{R}_p$ for nominally symmetric QWIPs were also reported by Schneider et al. [1991a].

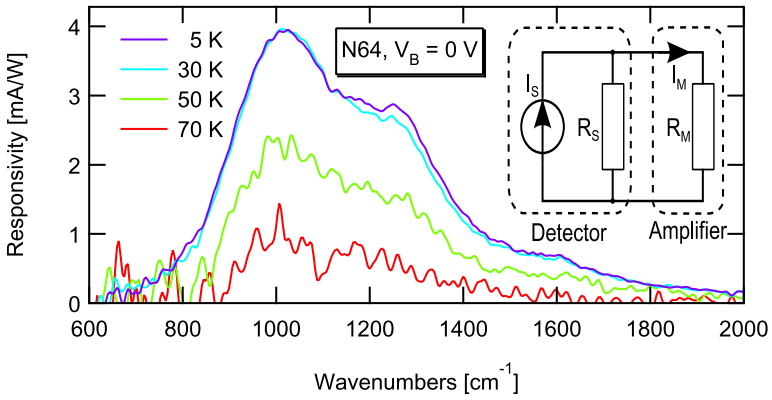

Figure 6.3: Responsivity of the B2B QWIP N64 at different temperatures at zero bias voltage. The inset shows a simple equivalent circuit of detector and amplifier.

The zero bias responsivity is shown for different temperatures up to 70 K in figure 6.3. For higher temperatures, the signal is buried by noise due to the fast decrease of the device resistance. The responsivity decrease above 30 K is explained by the impedance mismatch

between N64 and the current amplifier. Using a simple equivalent circuit (inset of figure 6.3) of a current source I_S with an internal resistance R_S and a current amplifier with an internal resistance R_M measuring the current I_M, the amplified current amounts to $I_M = I_S \cdot R_S/(R_A + R_S)$. The input impedance of the SR570 current amplifier amounts to $R_M = 100\,\Omega$ (amplification $10\,\mu$A/V) and the measured N64 resistance is $170\,\Omega$ at 50 K and $56\,\Omega$ at 70 K; the measured current I_M is thus 63% at 50 K respectively 36% at 70 K of I_S, which corresponds to the observed responsivity decrease.

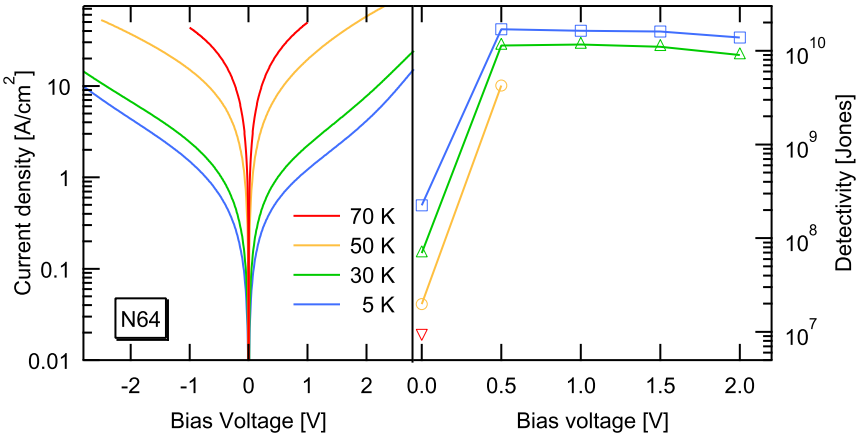

Figure 6.4: Left panel: current density - voltage measurement of N64 for different temperatures. Right panel: detectivity $\mathcal{D}^*$ of N46 as function of bias voltage for different temperatures. At 50 K and 70 K, the responsivity and thus detectivity was not measured at elevated voltages, as the current amplifier saturates for dark currents above 1 mA.

N64's detectivity $\mathcal{D}^* = \mathcal{R}/i_n\sqrt{A\Delta f}$ is shown on the right panel of figure 6.4. At $V_B = 0$, $\mathcal{D}^*$ is Johnson noise limited and i_n is given by (2.39) with the resistance at 0 V extracted from the measured I−V curves shown on the left panel of figure 6.4. For $V_B \neq 0\,$V, $\mathcal{D}^*$ is dark current limited and i_n is given by (2.40). The noise gain g_n used in (2.40) is set equal to the photoconductive gain g_{phot} calculated using (2.38); for the calculation of g_{phot}, the peak absorption $\eta_p = 51\%$ was calculated with Fermi's golden rule (2.27). The detectivity is maximal for $V_B = 0.5\,V$ at 5 K with $\mathcal{D}^* = 1.6 \times 10^{10}$ Jones.

In conclusion, a bound to bound QWIP detecting at 10 µm was presented. Compared to similar QWIPs [Levine et al., 1992], N64 has an overall low performance, especially at elevated temperatures. The optimization of this structure, for example by bringing the first excited state in resonance with the barrier and reducing the QW doping, was not pursued in this work as N64 has the main purpose to serve as reference for the later detectors.

6.2 Bound to miniband QWIP

The working principle of the bound to miniband (B2M) QWIP N284 presented in this section is based on a B2B QWIP, but each barrier is replaced by a superlattice consisting of equally thick barriers and QWs whose electron ground states couple to each other and form a miniband, as described in section 3.2.1. As opposed to the common B2B

QWIP design, where photoexcited electrons are transported in the continuum state above the barrier, the electron transport takes place in the superlattice miniband. For this purpose, the first excited state in the doped QW A is in resonance with the ground-state miniband of the superlattice. Compared to a B2B QWIP, this design offers a higher flexibility concerning the choice of detection wavelength λ_d and material system: λ_d is determined by the energy separation between the miniband and the ground state, and is not fixed by the CBO, whereas the upper state in a B2B QWIP needs to be close to the top of the barrier. Long wavelength B2M QWIPs can thus be realized in the alternative $In_{0.53}Ga_{0.47}As$ / $In_{0.52}Al_{0.48}As$ system with a CBO of 520 meV, whose light effective QW mass ($m = 0.0427$, GaAs: $m = 0.067$) increases the ISB absorption efficiency $\eta \propto 1/m$. The absorption and detection linewidth of a B2M detector is determined by the miniband width, which again depends on the remaining barrier height and the barrier thickness (see also section 2.1.2). B2M QWIPs have a lower photoconductive gain compared to B2B QWIPs because the photoexcited electron transport occurs in the miniband where electrons must tunnel through many thin heterobarriers, resulting in a lower mobility.

A B2M QWIP was first proposed by Yu and Li [1991]. Its working principle is visualized by the simulated bandstructure of sample N284 shown in figure 6.5 designed for a detection energy around 145 meV. Upon illumination, radiation is absorbed in the doped QW A,

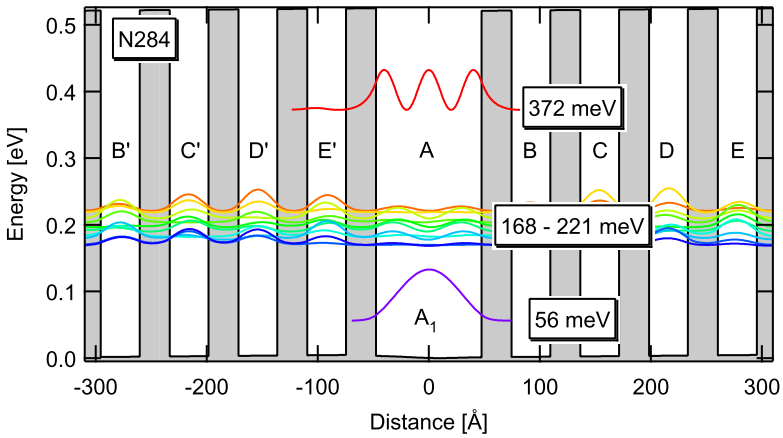

Figure 6.5: Simulated bandstructure of the bound to miniband detector N284 designed for a detection energy around 145 meV (8.5 µm).

exciting electrons from the doped ground state A_1 into the first excited state A_2 which is in resonance with the miniband. By applying a bias voltage over the active region, the photoexcited electrons are transported in the miniband towards the anode until they are collected by the anode or recaptured into another active QW (corresponding to QW A in figure 6.5). In analogy to a B2B QWIP, the efficiency of this process is described by the photoconductive gain $g_{photo} = p_e/(N\,p_c)$, where p_c is the capture probability of electrons by the active QW A of the next period, p_e is the escape probability for an excited electron from the state A_2 into the miniband and N is the number of periods consisting of QW and barriers A to E.

N284 was grown by MBE on a semi-insulating InP substrate and started with a 8000 Å thick $In_{0.53}Ga_{0.47}As$ buffer layer n-doped to $6 \times 10^{16}\,cm^{-3}$ followed by 30 repetitions of

n_{QW}	A	B	C	D	E
$2.1 \times 10^{17}\,\mathrm{cm}^{-3}$	95/27	35/27	35/27	35/27	35/27

Table 6.1: Growth parameters of the B2M detector N284. The first column lists the doping density n_{QW} of QW A; the ##/## number pairs in columns A−E are $In_{0.53}Ga_{0.47}As$ QW / $In_{0.52}Al_{0.48}As$ barrier thicknesses in Å. The column labels correspond to the band diagram in figure 6.5.

the active period described in table 6.1 and a 2500 Å $In_{0.53}Ga_{0.47}As$ cap layer n-doped to $5\times10^{18}\,\mathrm{cm}^{-3}$. One period is composed of the degenerately doped QW A and a superlattice forming a ground state miniband in resonance with the first excited state of QW A. N284 was processed into mesa structures as described in section 5.1 and a $(100\,\mu\mathrm{m})^2$ mesa was contacted for characterization. Current responsivity spectra were taken with a FTIR as described in section 5.2.

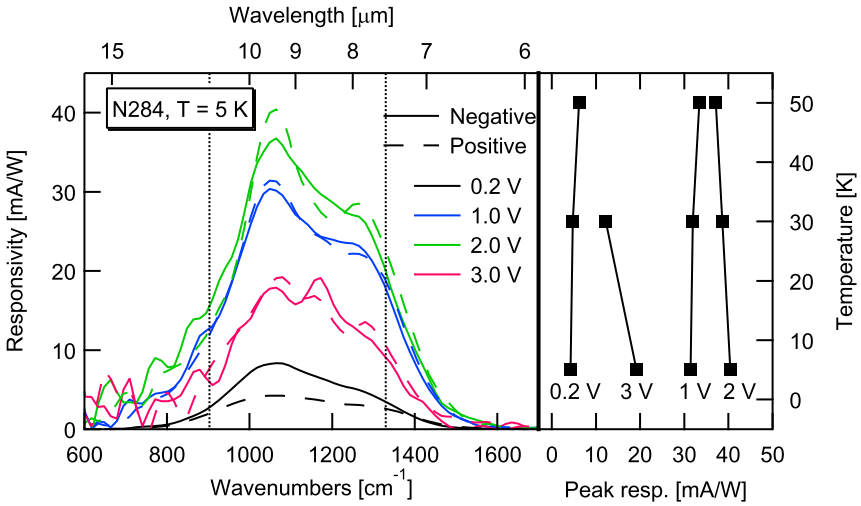

Figure 6.6: Left panel: measured responsivity spectra of the B2M detector N284 at 5 K for different bias voltages. The two dotted lines correspond to the simulated energy difference between the ground state A_1 and the lower respectively upper miniband edge. Right panel: temperature dependence of the peak responsivity at different bias voltages.

Figure 6.6 shows the measured current responsivity of N284 at 5 K for different applied bias voltages. The signal peaks at $1060\,\mathrm{cm}^{-1}$ (130 meV, 9.5 μm) and has its half-maxima at $920\,\mathrm{cm}^{-1}$ (114 meV) respectively $1350\,\mathrm{cm}^{-1}$ (167 meV), which is in good agreement with the simulated $A_1 \rightarrow$ miniband ISBT energies which lie between $905\,\mathrm{cm}^{-1}$and $1330\,\mathrm{cm}^{-1}$(112 meV − 165 meV). The peak responsivity is a non monotonic function of bias voltage: it increases up to 40 mA/W around ±2 V and then decreases since the miniband breaks up into localized wavefunctions lowering the escape probability for an excited electron. This is shown in the band profile in figure 6.7 calculated for an applied field of 2.7 V/μm corresponding to a 3 V potential difference across the active region. Such a responsivity maximum is another distinction compared to a B2B QWIP, where the responsivity increases with applied bias voltage up to a value where the carrier mobility in

the semiconductor is reduced by intervalley scattering. Compared to the 120 mA/W of the B2B QWIP N64 presented in section 6.1 detecting in the same wavelength range, the peak responsivity of N284 is about three times lower; as discussed above, this is explained by the lower mobility in the miniband for the B2M QWIP N284 compared to the continuum transport of the B2B QWIP N64.

The right panel of figure 6.6 shows the temperature dependence of N284's peak responsivity for different positive bias voltage amplitudes. At temperatures above 50 K, the dark current increases significantly, wherefore no signal could be measured for temperatures above 50 K due to the dominating dark current noise.

At 5 K and zero bias, the peak responsivity $\mathcal{R}_p$ of N284 amounts to 0.3mA/W, which is in contrast with the model of a symmetric photoconductive B2M QWIP where $\mathcal{R}_p$ should vanish at zero bias. This zero-bias $\mathcal{R}_p$, which is 13 times smaller than $\mathcal{R}_p$ at 2 V bias, can most probably be explained by a slight asymmetry in the structure as discussed in section 6.1 for the B2B QWIP N64.

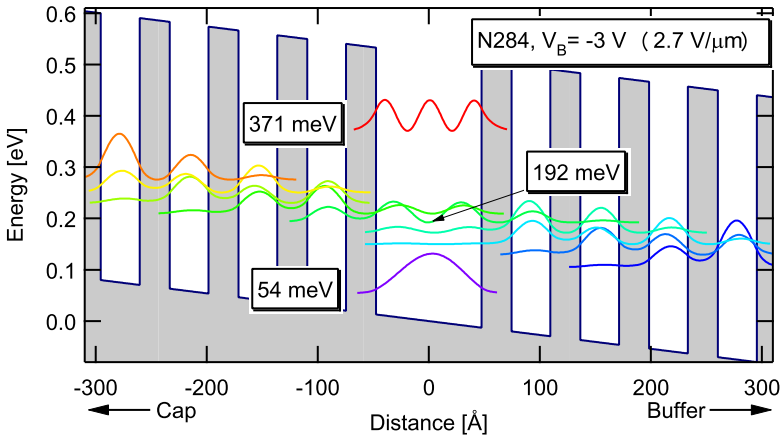

Figure 6.7: Simulated band structure of N284 with an applied electrical field of 2.7 V/µm corresponding to a bias voltage of 3 V across the active region. The miniband splits up into localized states, resulting in a lower escape probability and thus a lower responsivity.

The detectivity $\mathcal{D}^*$ of N284 was calculated with (2.45) using the measured peak responsivity. Similar to the previous, at zero bias, $\mathcal{D}^*$ is Johnson noise limited and the noise current is given by (2.39); for non-zero bias, $\mathcal{D}^*$ is limited by dark current noise i_d. To determine i_d with (2.40) the noise gain g_n was assumed to be equal to the photoconductive gain g_{photo} which was calculated using (2.38) and the measured peak absorption $\eta_p = 0.27$. Figure 6.8 shows the detectivity of N284 as function of bias voltage for 5 K and 50 K. $\mathcal{D}^*$ is maximal at 5 K and 0.2 V bias, where it amounts to 1.8×10^{10} Jones. This is nearly identical to the $\mathcal{D}^* = 1.6 \times 10^{10}$ Jones of the B2B QWIP N64 presented in section 6.1. The lower responsivity of the B2M QWIP N284 is thus compensated by its higher resistance resulting in a lower dark current noise.

In conclusion, a B2M photodetector sensitive between 11 µm and 7.5 µm was demonstrated. The device resistance R_0A of the B2M QWIP N284 is significantly higher compared to the B2B QWIP N64: at 5 K, $R_0A = 4.3 \times 10^4\,\Omega\text{cm}^2$ for N284, whereas $R_0A = 0.58\,\Omega\text{cm}^2$ for N64. However N284's responsivity of up to 40 mA/W at ±2 V bias

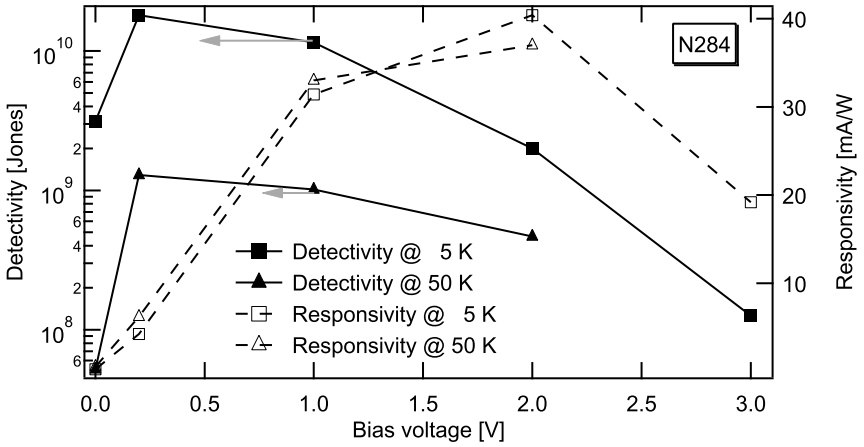

Figure 6.8: Peak detectivity and responsivity values of N284 as function of bias voltage at 5 K and 50 K.

is low compared to N64, which is attributed to the lower mobility of the miniband in comparison to the continuum.

The miniband however allows to tailor the detector's linewidth by design; the structure presented in this section shows a fractional linewidth of 35%, as compared to QWIP linewidths which usually lie around 20%. The detectivity is maximal at 5 K and 0.2 V with 1.8×10^{10} Jones and drops to 1.3×10^{9} Jones at 50 K. Yu and Li [1991] reported on a B2M QWIP with GaAs QWs and AlGaAs barriers detecting at 9 µm for which $\mathcal{D}^* = 1.6 \times 10^{10}$ Jones at 77 K. This better high temperature $\mathcal{D}^*$ is explained by the larger responsivity $\mathcal{R} = 230$ mA/W of their device, which is probably due to the lower $Al_{0.4}Ga_{0.6}As$ barrier height above the miniband (about 150 meV compared to about 300 meV for N284). Around 10 µm, the beneficial impact of the low $In_{0.53}Ga_{0.47}As$ effective electron mass on the absorption efficiency is thus canceled by the high $In_{0.52}Al_{0.48}As$ barrier height in the case of a B2M QWIP. Another MIR ISB photodetector design, the photovoltaic quantum cascade detector (QCD), is better suited to the $In_{0.53}Ga_{0.47}As$ / $In_{0.52}Al_{0.48}As$ system; in the following sections, QCDs detecting at different MIR wavelengths are thus presented.

6.3 Quantum cascade detectors

As described in section 3.2.2, QCDs are ISB photodetectors with a built-in asymmetry, which is the reason for which they generate a measurable photocurrent without requiring an external bias voltage. Although QCDs have a low responsivity compared to photoconductive QWIPs, they have a lower noise current: due to the biasless operation, no dark current noise is present and the generally lower Johnson noise is dominant. As the detection wavelength of QCDs is determined by a bound to bound transition, it is not fixed to the CBO, thus MIR QCDs can be realized in material systems with large CBOs.

In this section, QCDs detecting at wavelengths of 17 µm, 10 µm, 7.5 µm, and 4.7 µm are presented; they all have $In_{0.53}Ga_{0.47}As$ QWs and $In_{0.52}Al_{0.47}As$ barriers lattice matched to the InP substrate.

6.3.1 17 μm quantum cascade detector

Wavelengths close to 17 μm are of interest to astronomers for detection of cold interstellar molecular Hydrogen (H_2) using heterodyne spectroscopy [Krötz et al., 2008], as the shortest pure rotational line of H_2 lies at 17.035 μm [Valentijn and van der Werf, 1999]. This heterodyne detection scheme requires fast detectors sensitive at 17 μm; semiconductor ISB detectors are probably the only devices which can bring together those two requirements. In this section, three QCDs detecting at wavelengths around 17 μm are demonstrated. The samples were grown by MBE on semi-insulating InP substrate and consist of a 30 period active region described in table 6.2 sandwiched between two n-doped $In_{0.53}Ga_{0.47}As$ contact layers.

Figure 6.9 shows the calculated conduction band diagram of sample N819 designed for a detection energy (corresponding to the $A_1 \rightarrow A_2$ transition) of 68.2 meV (18.2 μm). Given the low detection energy and the $In_{0.53}Ga_{0.47}As$ LO phonon energy of 34 meV, the usual phonon stair QCD extractor described in section 3.2.2 would have only two steps. Such a single QW extractor would result in strong coupling between adjacent active QW ground states and thus a large dark current. To reduce this undesired ground state coupling, the center rung of the phonon stair consists of a miniband formed by several QWs and barriers with similar thicknesses. Thus, a photoexcited electron in level A_2 tunnels to B_1 and is then injected into the 25 meV lower C_1-F_1 miniband by phonon-assisted tunneling. From there, it is collected into the 35 meV lower ground state of the next period A'.

	E_{12} [meV (μm)]	A	B	C	D	E	F
N819	68.2 (18.2)	157/55	69/26	90/43	94/40	95/38	96/28
N973	71.3 (17.4)	153/55	63/40	66/36	70/32	73/30	74/24
N975	66.0 (18.8)	161/55	67/40	70/36	74/32	77/30	78/24

Table 6.2: Layer thicknesses for one period of the active region of the QCDs operating around 17 μm along with the simulated detection energy E_{12}. The layer thicknesses are given in Å for one period in QW/barrier pairs which are alphabetically labeled according to the band diagram in figure 6.9. The active region contains 30 periods and is sandwiched between a lower, 6000 Å thick, and upper, 2000 Å thick contact layer. The contact layers are doped to $3 \times 10^{17}\,cm^{-3}$ and QW A to $1 \times 10^{17}\,cm^{-3}$.

For responsivity measurements, metalized mesa structures were processed on N819 and a 45° facet was polished as described in section 5.1; the left panel of figure 6.10 shows the responsivity spectra for a $(200\,\mu m)^2$ mesa of N819 measured with the FTIR spectrometer's glowbar and KBr beamsplitter. At 10 K, the responsivity peaks at $610\,cm^{-1}$ (75.6 meV / 16.5 μm) with 3.7 mA/W and drops to 0.31 mA/W at 90 K. At higher temperatures, the low signal to noise ratio prohibited a reliable responsivity measurement: at 90 K, the $A_1 \rightarrow A_2$ photocurrent under illumination by the FTIR glowbar source amounts to 0.27 nA, whereas the Johnson noise RMS current calculated using (2.39) is already 0.53 nA at 110 K. The responsivity decrease with increasing temperatures is partially explained by the impedance mismatch between the source and the current amplifier as discussed in section 6.1: the device resistance of N819 decreases from $R_S = 10^6\,\Omega$ at 5 K to $R_S = 640\,\Omega$ at 90 K resulting in a 13% decrease of the photocurrent.

The responsivity spectra of N819 shown in the left panel of figure 6.10 have two pro-

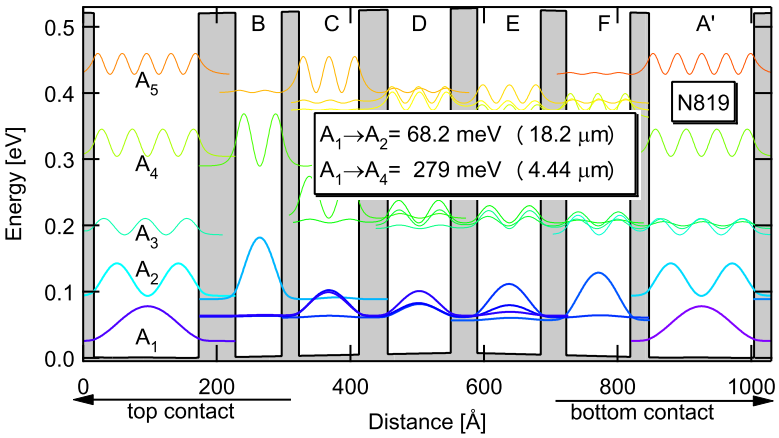

Figure 6.9: Simulated conduction band profile of the 17 μm QCD (sample N819). QW A is degenerately doped, leading to a populated state A_1. Photoexcited electrons can tunnel from A_2 through the C_1-D_1 miniband to the next period.

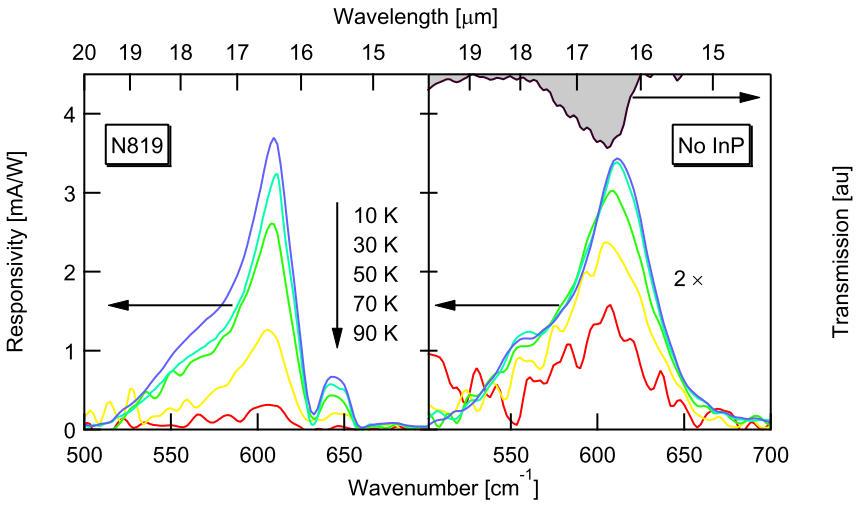

Figure 6.10: Measured responsivity spectra of sample N819. The left panel shows data obtained with a standard 45° facet which has two pronounced notches at 633 meV and 660 meV due to two-phonon absorption in the InP substrate; the data shown on the right panel was measured with the InP substrate removed and lacks the two dips. The measured ISB transmission shape is shown hanging from the top axis.

nounced dips at 633 cm^{-1} and 660 cm^{-1} which have their origin in the two-phonon absorption of the InP substrate [Koteles and Datars, 1976]. To measure a responsivity with the intrinsic ISBT line shape, a second process was done where the InP substrate below the signal mesa was removed using 37% HCl wet etching; HCl etches In at a rate of about 7 µm/s, whereas InGaAs and InAlAs are inert towards HCl. For this, the sample was first mounted and bonded in the standard 45° facet geometry. The metalized sample top and the bond wires were covered by wax for protection and stability, whereas the 45° facet below the bonded mesa was left free as shown schematically in figure 6.11. The sample was then partially dipped into HCl, thus removing the InP substrate below the bonded mesas, whereas a collapse of the 3 µm thin epitaxial layer was prevented by the wax. The progress of the etch process is documented by the three photos at the bottom of figure 6.11 taken underneath the 45° facet at different stages of the etch process.

As expected, the two two-phonon dips disappeared from the responsivity spectra shown on the right panel of figure 6.10, resulting in a more symmetric lineshape. The lower peak responsivity value of the measurement without substrate as compared to the un-etched sample is caused by a lower ISB absorption efficiency $\eta \propto \sin^2\alpha/\cos\alpha$ due the steeper (smaller) propagation angle α of the light inside the active region: compared to $\alpha = 45°$ in the standard 45° MPW geometry, α cannot be higher than the angle of total internal reflection between the active region and air for the substrate-etch process, namely about 20°.

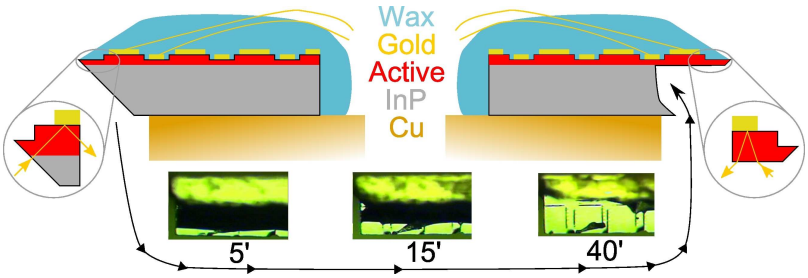

Figure 6.11: Schematic of InP etch process applied to N819. The three microscope photos at the bottom show the 45° facet after 5, 15, and 40 minutes HCl etch; after 40 minutes, the $(200\,\mu m)^2$ mesas are completely liberated from the InP substrate. The small inset to the left shows the light path for the 45° facet coupling, the one to the right for a sample with removed InP substrate.

At 10 K, the responsivity of the substrate-etch process peaks at 611 cm^{-1} (16.5 µm) and has a FWHM of 47 cm^{-1}, resulting in a fractional linewidth of 7.7%. Compared to the simulated $A_1 \rightarrow A_2$ energy of 550 cm^{-1}, the measured peak energy is 11% higher. Including the manybody effects described in section 2.1.4, the depolarization redshift and the excitonic blueshift result in an overall blueshift of only 0.9%. Another possible cause for the discrepancy between simulated and observed transition energy is a deviation of the effective thickness of QW A from the nominal one: for a QW thickness of 151 Å instead of 157 Å, the simulated transition energy of 606 cm^{-1} is in good agreement with the measured 611 cm^{-1}. This explanation is also supported by x-ray measurements, which revealed an active region period of 813 Å, 2.2% below the nominal value of 831 Å; this coincides well with a 151 Å active QW if only the $In_{0.53}Ga_{0.47}As$ QW thicknesses deviate from the

nominal values. The assumption that the effective QW thickness is thinner than the nominal one is further corroborated by a second responsivity peak at 2412 cm^{-1} (299 meV / 4.15 µm) which is attributed to the $A_1 \rightarrow A_4$ transition calculated to lie at 2420 cm^{-1} for a 151 Å thick QW A. The peak responsivity of this feature is about 30 times lower than the $A_1 \rightarrow A_2$ peak (namely 0.1 mA/W), which is explained by the lower dipole matrix element and the lower extraction efficiency from A_4 towards the next period.

In order to minimize the influence of InP two-phonon absorption, the ISB transmission hanging from the top axis in the right panel of figure 6.10 was obtained with a relatively small (200 µm thick and 500 µm long) 45° MPW. For normalization purposes, an additional transmission measurement was taken from a part of the thin sample where the active region was removed previously by wet etching. The transmission peaks at 605 cm^{-1} and is 34 cm^{-1} wide. Due to the small size of the sample, stray light problems made it impossible to extract a meaningful value for the absorption efficiency. Although the optical path length in the sample is only 700 µm, the ISB peak overlaps partly with the two-phonon absorption at 632 cm^{-1} and 660 cm^{-1}, resulting in an asymmetric shape with a steeper drop at higher energy.

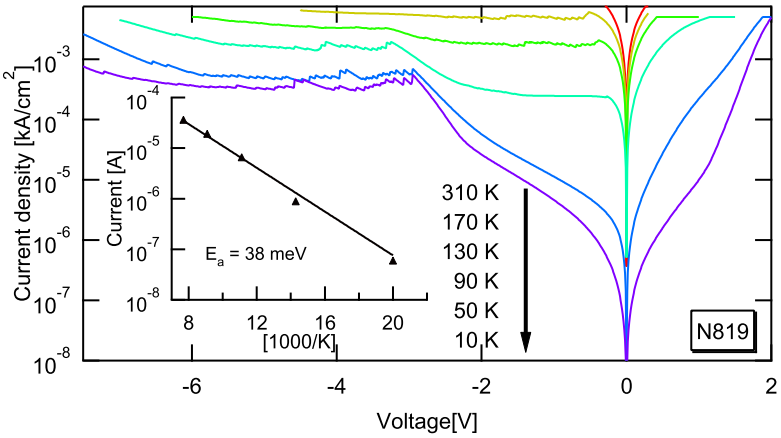

Figure 6.12: $I-V$ characteristics of N819 for different temperatures. The inset shows the Arrhenius plot taken at 90 mV; the extracted activation energy is $E_a = 50$ meV.

Figure 6.12 shows the $I-V$ characteristics of N819 at different temperatures. Positive voltages correspond to a positive potential at the top contact and therefore a positive conduction band slope in figure 6.9. For 10, 50, and 90 K, negative differential resistance (NDR) features set in at a voltage of −3 V at the top contact, whereas at 130 and 170 K, additional NDR features occur for voltages below −0.38 V. When computing the band structure with a superimposed electric field of $E_{ext} = 1.2\,\mathrm{V/\mu m}$ corresponding to a potential difference of −3 V across the active region, the ground state A_1 comes into resonance with the second extraction cascade state D_1 of the same period. At higher voltages, each period sequentially breaks off from this resonance condition resulting in multiple NDR peaks. At higher temperatures, the current through the miniband increases significantly due to thermal excitation, resulting in additional low-voltage NDR features due to resonances in the extraction miniband. A thermal activation energy of $E_{act} = 38$ meV was extracted from the Arrhenius plot of the current at 50 mV inset in figure 6.12; this E_{act}

corresponds to the energy separating the ground state from the extraction miniband, a clear indication for leakage current across the miniband.

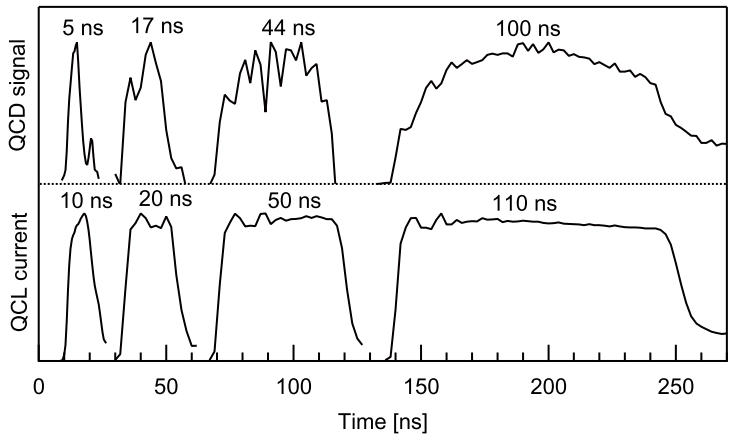

Figure 6.13: Signal of N819 illuminated by a pulsed 17 µm quantum cascade laser. Bottom: normalized laser drive current. Top: normalized detector signal. The FWHM times are indicated above the pulses.

As described at the beginning of this section, a 17 µm photodetector is of interest for heterodyne spectroscopy of interstellar gases to determine the amount of cold molecular Hydrogen based on its absorption line at 17.035 µm. The heterodyne detection scheme, which is described in detail by Sonnabend et al. [2002], depends on a high electrical bandwidth of the photodetector in the GHz range. With this application in mind, a first estimation of the detector speed was performed by measuring the response of N819 cooled to 10 K to the pulsed 17 µm quantum cascade laser (QCL) presented by Rochat et al. [2001]. For this experiment, the QCD photocurrent was amplified by a Miteq AFS5-00102000-30-10P-4 amplifier in series with a Sonoma 317 amplifier, which have an upper bandwidth limit of 2 GHz respectively 2.5 GHz. Figure 6.13 shows QCL drive current pulses of different lengths and the QCDs response to the optical pulse, both measured with an oscilloscope. The shortest optical pulse width measured is 5 ns, resulting in a QCD bandwidth of at least 200 MHz. As the QCL drive current electronics did not allow for shorter pulses, this value can be regarded as a lower limit for the true bandwidth, which, based on the results from a similar device detecting at 5.35 µm demonstrated by Hofstetter et al. [2006], is supposed to be in the GHz range. The smaller width of the measured QCD pulses compared to the drive current pulses can be explained by a retardation of lasing onset owing to the non-ideal current pulse flank.

Two modified 17 µm QCDs were grown with their extractor miniband A_1–F_1 lifted close to the coupled levels A_2, B_1 to obtain an increased device resistance and extraction efficiency. To assure that at least one of the new samples has a lower detection energy and is thus not affected by InP two-phonon absorption, one (N973) has an active QW thickness of 153 Å and the other (N975) one of 161 Å. Figure 6.14 shows the responsivity spectra of N973 and N975. At 5 K, the responsivity of N973 peaks at 605 cm^{-1} (75.0 meV) and the one of N975 at 574 cm^{-1} (71.2 meV). For N975 the InP two-phonon absorption

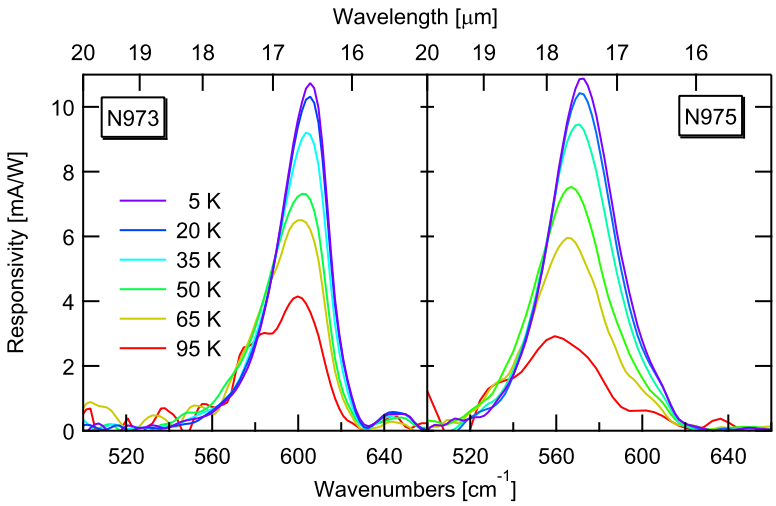

Figure 6.14: Measured responsivity spectra for different temperatures of samples N973 (left panel) and N975 (right panel).

is not visible anymore due to the lower peak detection energy. For both N975 and N973, the responsivity is more than twice as high compared to N819; this indicates a higher photoconductive gain and thus a higher extraction efficiency of the lifted miniband design.

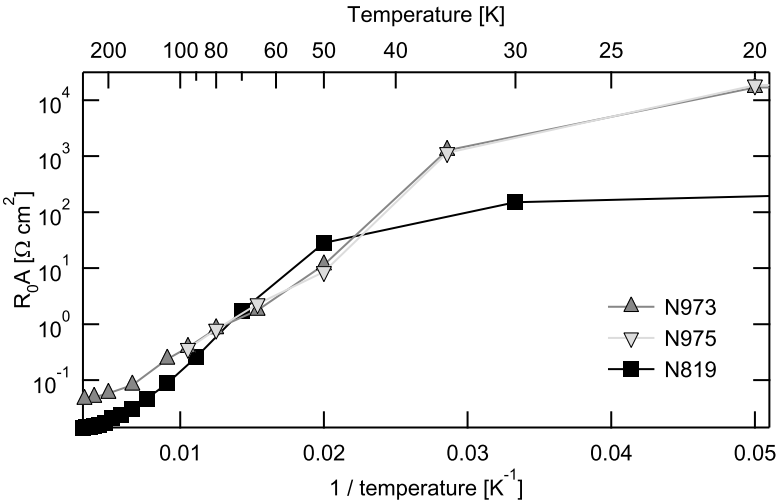

Figure 6.15: $R_0\,A$ product of the 17 µm QCDs as function of inverse temperature.

Figure 6.15 shows the resistance - area product $R_0\,A$ of all three 17 µm QCDs as function of inverse temperature. As expected for QCDs, the slope (which is proportional to the thermionic activation energy) decreases at low temperatures; this effect is more pronounced for N819, as its extraction miniband is at a lower energy compared to N973 and N975.

Based on the measured responsivity and device resistance, the Johnson noise limited detectivity D_J^* was calculated using (2.47). As seen in figure 6.16, both N973 and

N975 have a higher D^*_J compared to N819, especially at low temperatures: at 5 K, $D^*_J = 10^{11}$ Jones for N973 compared to $D^*_J = 4.3 \times 10^9$ Jones for N819. The photon noise limited BLIP detectivity calculated using (2.48) for a 300 K background and a hemispheric FOV is $1.22{\times}10^{11}$ Jones, wherefore no sample reaches the BLIP condition in the investigated temperature range.

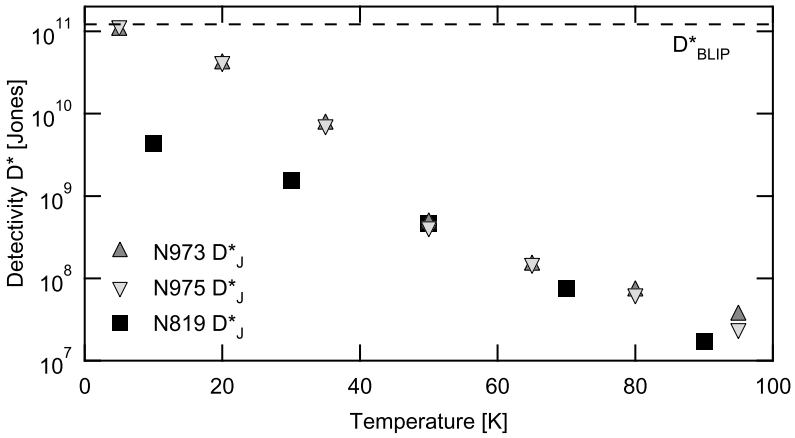

Figure 6.16: Johnson noise limited detectivity of the 17µm QCDs as function of temperature. The dashed line represents D^*_{BLIP} for a hemisphere FOV and a 300 K background.

Although N975 has a sufficiently low $A_1 \rightarrow A_2$ transition energy not to be affected by the InP two-phonon absorption, it is too close to the lower energy limit of the used spectrometer setup (shown in figure 5.5) to measure the peak absorption efficiency η_p. To nonetheless estimate the gain of the 17 µm QCDs, η_p was calculated with Fermi's golden rule (2.27) using the FWHM extracted from the responsivity measurements. For a double pass through the active region, the calculated η_p amounts to 38% for all three QCDs; inserting this value together with the measured peak responsivities into (2.38) results in escape probabilities p_e between 2% and 6% for the three presented QCDs. These low values are probably caused by the high barriers resulting in a low A_2-B_1 miniband width and thus a low tolerance for the layer thicknesses: a small deviation from the nominal value breaks up the A_2-B_1 miniband resulting in a greatly reduced extraction efficiency.

In conclusion, three QCDs detecting around 17 µm where demonstrated. Thanks to the vertical miniband transport in the extraction cascade, a high resistance is maintained for temperatures up to 100 K and a maximal operating temperature of 95 K is reached. By using a 17 µm QCL operating at short current pulses, a setup limited maximum operating frequency of 200 MHz was determined. Two devices based on a modified design with a lifted miniband showed an increased resistance and thus a higher detectivity compared to the original design. For this design, the detectivity at 5 K amounts to 10^{11} Jones. For a 17 µm bound to bound QWIP presented by Sarusi et al. [1994], the detectivity is 3×10^9 Jones at 55 K. For heterodyne spectroscopy, a detectivity of at least 10^{10} Jones at liquid nitrogen temperature (77 K) is desirable.

The $2-6\%$ escape probability p_e of the 17 µm QCDs still leaves room for improvement. To increase p_e, the alignment between the excited state A_2 of the active QW A and the

ground state B_1 of the first extractor QW B should be improved. By implementing the presented design in a material system with a lower CBO, such as GaAs / AlGaAs, the A_2 - B_1 miniband width increases, which reduces the impact of growth and simulation uncertainties on the extraction efficiency. Besides making the design more robust, this would not necessarily lead to a lower resistance: the steepest slope in figure 6.15 corresponds to an activation energy of 45 meV, which is well below the CBO of 520 meV indicating that the dark current of the presented devices is dominated by miniband transport.

6.3.2 10 µm, 7.5 µm, and 4.7 µm quantum cascade detectors

In this section, three QCDs detecting at 10 µm, 7.5 µm, and 4.7 µm based on $In_{0.53}Ga_{0.47}As$ / $In_{0.52}Al_{0.48}As$ lattice matched to InP are presented. As opposed to the 17 µm QCD discussed in section 6.3.1, the detection energy of those samples is sufficiently high to allow for an extraction cascade with multiple steps consisting of localized wave functions separated by about 35 meV; this ensures an efficient vertical transport of the electrons by LO-phonon assisted tunneling.

	E_{12}	n_{cnt}	n_{QW}	A	B	C	D	E	F	G	H
N1020	118	6	2	107/50	40.5/47	48/45	62/41	–	–	–	–
N1021	165	10	3	82/60	28/57	34/55	42/51	55/58	–	–	–
N1022	266	20	4	51/75	12.5/65	14.5/64	17/79	20/77	24/75	29/71	35/68

Table 6.3: Growth parameters of the 10 µm (N1020), 7.6 µm (N1021), and 4.7 µm (N1022) QCDs along with the simulated detection energy E_{12} in meV, and the Si doping densities n_{cnt} (upper and lower contact layer) and n_{QW} (QW A) in $10^{17}\,cm^{-3}$. The layer thicknesses are given in Å for one period in QW/barrier pairs which are alphabetically labeled according to the band diagram shown in figure 6.17.

All three samples were grown by MBE on a semi-insulating InP substrate; growth started with a 6000 Å thick $In_{0.53}Ga_{0.52}As$ lower contact layer followed by 30 repetitions of the active region described in table 6.3 and a 2000 Å thick $In_{0.53}Ga_{0.47}As$ upper contact layer. The layers are undoped except for the contact layers and the active QW A for which the nominal doping level is also listed in table 6.3.

The simulated bandstructure of the 10 µm QCD N1020 is shown in figure 6.17. The extraction cascade from A_2/B_1 to the ground state A_1' of the following period consists of three localized wavefunctions separated from each other by energy steps of 24 meV, 34 meV, and 54 meV, a compromise between high extraction efficiency and low Johnson noise: for a high extraction efficiency, the extractor steps should equal the $In_{0.53}Ga_{0.47}As$ LO phonon energy of 34 meV, whereas a large energy separation between the extractor wavefunctions and the ground state results in a higher resistance and thus a lower Johnson noise.

Analogous QCDs detecting at 7 µm (N1021) and at 4.7 µm (N1022) were designed by adapting the QW thickness and adding additional extractor steps to maintain a comparable step height. Also, the doping density of the active QW is chosen such that the Fermi energy relative to the ground state A_1 is similar for all samples and the contact layer doping is adapted to align the Fermi level between contact layer and active QW. The active region of N1021 and N1022 is described in table 6.3 and their simulated band diagrams

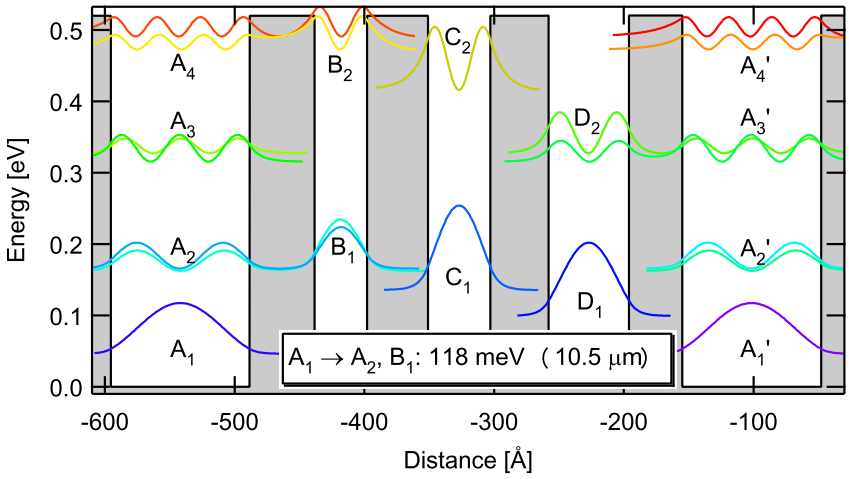

Figure 6.17: Simulated conduction band diagram of the 10.5 µm QCD N1020. The active QW A is degenerately doped, whereas the extractor consisting of QWs B, C, and D is undoped.

are found in appendix B. For characterization, metalized mesa structures were processed as described in section 5.1.

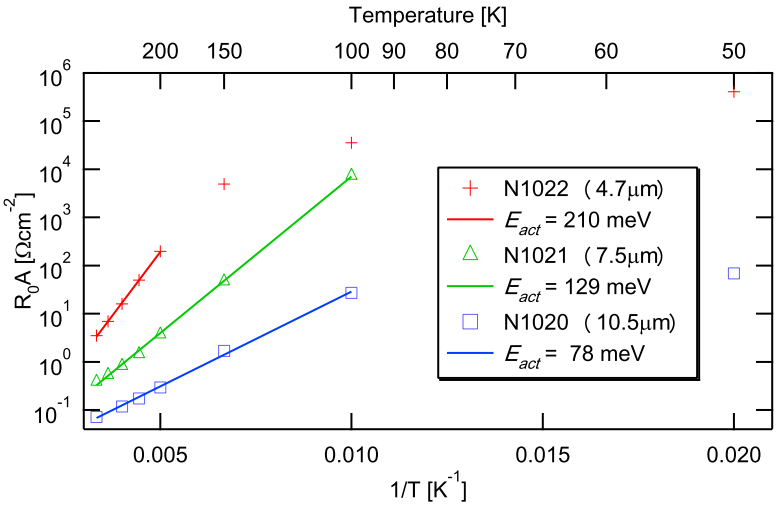

Figure 6.18: R_0A extracted from I-V measurements of the 10.5, 7, and 4.7 µm QCDs for different temperatures; the straight lines are exponential fits yielding the activation energies listed in the legend.

The I−V characteristics were measured with a $(200\,\mu\text{m})^2$ mesa for all three samples at different temperatures and the thus obtained differential resistance - area product around 0 V R_0A is shown in figure 6.18. The observed decrease of the Arrhenius plot slope at lower temperatures is common for QCDs. Structures with isolated QWs such as bound to bound QWIPs show a constant Arrhenius slope equivalent to the thermal activation energy from the QW ground state to the continuum. In a QCD, the contribution of

extractor states at intermediate energy levels to the dark current varies with temperature: at high temperatures, higher lying extractor states dominate dark current conductivity (corresponding to a steeper Arrhenius slope), whereas at lower temperatures, lower lying extractor states become more important (corresponding to a flatter Arrhenius slope). While comparing the data of the three QCD's in figure 6.18, it is evident that both R_0A as well as the high-temperature Arrhenius slope (and thus activation energy) increase with increasing detection energy; this is explained by the larger energy separation between the doped ground state A_1 and the remaining electron states for samples with higher detection energy.

The high-temperature activation energy of N1020 detecting at 127 meV extracted with a linear fit of $\ln(R_0A)$ over $1/T$ for $T = 100 - 300$ K is 78 meV, and lies between the simulated ISB energies $A_1 \rightarrow C_1 = 91$ meV and $A_1 \rightarrow D_1 = 56$ meV; for N1021 detecting at 168 meV, $E_{act} = 129$ meV corresponds to the simulated $A_1 \rightarrow C_1 = 129$ meV. The Arrhenius plot of N1022 detecting at 268 meV is only linear down to 200 K with $E_{act} = 210$ meV, corresponding to the simulated $A_1 \rightarrow D_1 = 209$ meV.

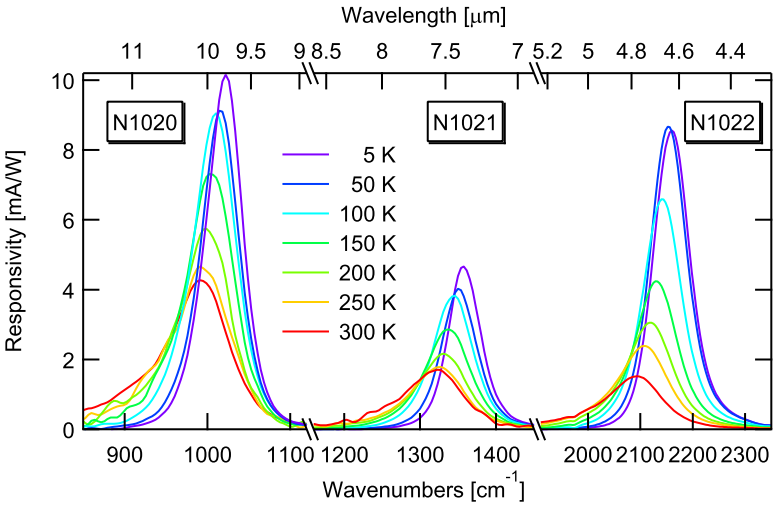

Figure 6.19: Responsivity of the ISB $A_1 \rightarrow A_2$ transition of N1020 (left), N1021 (center), and N1022 (right) at different temperatures.

	E_{12} (cm^{-1} / meV / µm)	$\mathcal{R}_p$ [mA/W]	2Γ [cm^{-1}] ($2\Gamma/E_{12}$)
N1020	1022 / 127 / 9.78	10.2	5 K: 21.7 (5.1%), 300 K: 87.5 (8.8%)
N1021	1358 / 168 / 7.4	4.7	5 K: 50.4 (3.7%), 300 K: 90 (6.8%)
N1022	2160 / 268 / 4.63	8.6	5 K: 80.8 (3.7%), 300 K: 126 (6%)

Table 6.4: Peak position E_{12}, peak value $\mathcal{R}_p$, and FWHM 2Γ, of the measured responsivity spectra of the InGaAs QCDs N1020, N1021, and N1022 taken from figure 6.19.

For optical characterization, a 45° facet was polished and a $(200\,\mu m)^2$ mesa was contacted. Figure 6.19 shows the $A_1 \rightarrow A_2$ responsivity peak of all three samples. The responsivity peak position E_{12}, peak value $\mathcal{R}_p$ and FWHM 2Γ are summarized in table 6.4. The observed increase of the absolute linewidth with decreasing QW thickness is common for

ISBTs and is explained by an interface roughness dominated lineshape [Campman et al., 1996].

For N1022 and N1021, the measured ISBT energy corresponds well to the simulated one of 266 meV for N1022 respectively 165 meV for N1021; for N1020, the observed value of 127 meV is 8% above the designed 118 meV. Including manybody effects in the calculations as described in section 2.1.4 results in a 0.3% redshift; although not determined unambiguously, the origin of the remaining blueshift lies most probably in a QW thickness deviation: for a 4% thinner QW, the simulated $A_1 \rightarrow A_2$ ISBT energy corresponds to the measured value.

All three samples exhibit an ISBT energy redshift with increasing temperature; for N1020, for example, the responsivity shifts from 1022 cm^{-1} (127 meV / 9.78 µm) at 5 K to 991 cm^{-1} (123 meV / 10.1 µm) at 300 K. A simple theory taking into account only the temperature dependence of the effective electron mass and CBO would predict a blueshift of the ISBT energy with increasing temperature; to explain the observed redshift well known in literature [Covington et al., 1989, Manasreh et al., 1990] correctly, band filling and nonparabolicity have to be taken into account [Larrabee et al., 2003]: as shown on the right panel of figure 6.20, the occupancy transition of the Fermi-Dirac distribution becomes smoother at higher temperatures leading to population of larger wave vector states of the ground state A_1. In combination with the non-parabolicity of the electron bands, this leads to an energy reduction and broadening of the ISB transition with higher temperature as shown in figure 6.20.

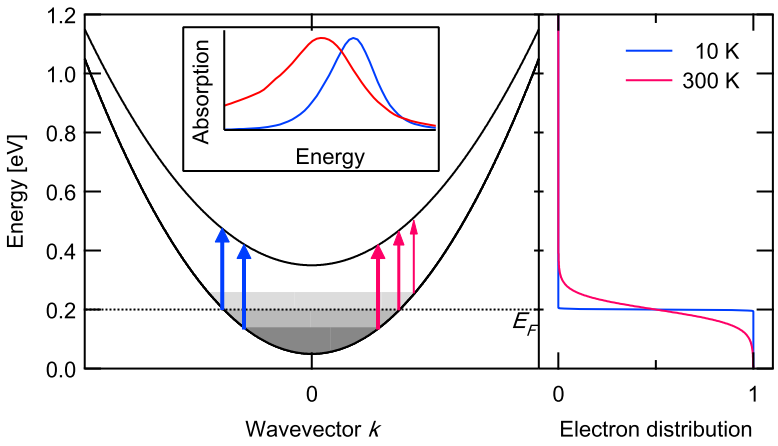

Figure 6.20: Temperature dependent ISB energy shift. Left panel: conduction band diagram of a 2-level QW in k space. E_F is the Fermi level, the arrows illustrate absorption probabilities and the shaded area represents the electron population at 300 K (darker shade = higher population). Inset: normalized absorption spectrum at 10 K (blue, narrow) and 300 K (red, broadened and redshifted) . Right panel: Fermi-Dirac distribution at 10 K and at 300 K.

Another striking feature of the responsivity spectra shown in figure 6.19 is the decrease of the peak responsivity $\mathcal{R}_p$ with increasing temperature. For N1020 $\mathcal{R}_p$ drops from 10.2 mA/W at 5 K to 4.27 mA/W at 300 K. This behavior is explained by both broadening of the ISB linewidth 2Γ and the lower electron population n_s in the ground state A_1 at

higher temperatures due to thermal activation of electrons into the D_1 level lying 54 meV above A_1, as $\mathcal{R}_p \propto \eta \propto n_s/\Gamma$. For N1020, the calculated n_s drops from $2.14 \times 10^{11}\,\mathrm{cm}^{-2}$ at 5 K to $1.7 \times 10^{11}\,\mathrm{cm}^{-2}$ at 300 K and the measured Γ increases from $25.85\,\mathrm{cm}^{-1}$ to $43.75\,\mathrm{cm}^{-1}$, resulting in a calculated 53% reduction of the peak responsivity which is close to the observed 58% decrease in $\mathcal{R}_p$.

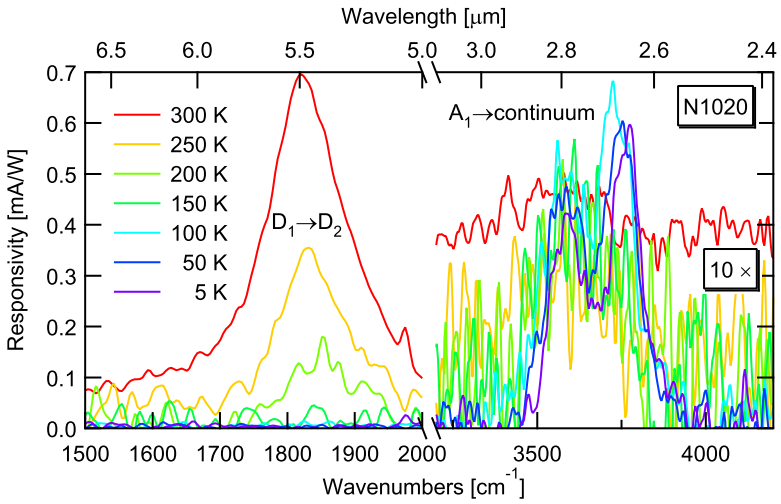

Figure 6.21: Additional photocurrent peaks of N1020. The left peak has its origin in the $D_1 \rightarrow D_2$ transition, the right peak in the $A_1 \rightarrow$ continuum transition.

Figure 6.21 shows the high energy continuation of N1020's responsivity spectrum shown in figure 6.19. The left panel shows a responsivity peak around $1820\,\mathrm{cm}^{-1}$ (256 meV / 5.49 μm), which is only visible at temperatures above 100 K and reaches 0.7 mA/W at 300 K. This signal is caused by the $D_1 \rightarrow D_2$ transition in the thickest, last extractor QW. At low temperatures, this transition is not visible due to the low electron population of D_1: self-consistent Schrödinger-Poisson simulations resulted in a population of $n_s^{D1} = 5.36 \times 10^6\,\mathrm{cm}^{-2}$ at 50 K and to $n_s^{D1} = 2.8 \times 10^{10}\,\mathrm{cm}^{-2}$ at 300 K. In addition to the increased electron population of D_1 at higher temperatures, D_2 is in resonance with A_3, from where electrons are likely to relax to A_2 due to the high matrix element $\langle A_3|z|A_2\rangle = 18$ Å. A_2 again is by purpose designed to be in resonance with the extractor, wherefore a photocurrent arises through the $D_1 \rightarrow D_2 \rightarrow A_3 \rightarrow A_2 \rightarrow$ extractor $\rightarrow A_1'$ path resulting in the observed responsivity peak. As the upper level of the last extractor QW (D_2 in the case of N1020) is not in resonance with a level in the active QW (A_3 in the case of N1020) for N1021 and N1022, those two samples do not show a corresponding responsivity peak.

The right panel of figure 6.21 shows a further responsivity peak of N1020 around $3700\,\mathrm{cm}^{-1}$(460 meV / 2.7 μm). Based on its transition energy and its low amplitude of roughly 0.06 mA/W, it is assigned to the ISB transition from A_1 to continuum levels above the $In_{0.52}Al_{0.48}As$ barriers. For N1020 and N1021, another responsivity peak around $8000\,\mathrm{cm}^{-1}$ (990 meV / 1.25 μm) was observed which has its origin in the interband transition in the active QW A; this interband responsivity peak is strongest for N1020: 1.69 mA/W at 5 K and 2.89 mA/W at 300 K. A more detailed discussion of the interband responsivity in QCDs is found in appendix A.

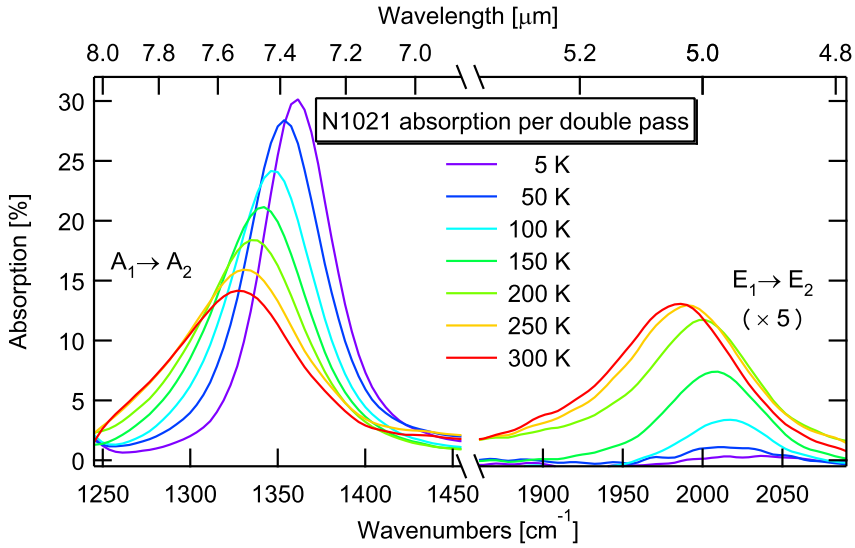

Figure 6.22: Absorption per double pass of N1021. Peak energy and FWHM agree with the measured responsivity.

All three samples were also polished into 45° MPWs for transmission measurements. Figure 6.22 shows the obtained absorption of N1021 for TM polarized light. The $A_1 \rightarrow A_2$ absorption shown on the left redshifts with increasing temperature in good agreement with the responsivity spectra shown in figure 6.19. The peak absorption decreases from 30% at 5 K (at 1360 cm^{-1}) to 14% at 300 K (at 1330 cm^{-1}), while the measured responsivity decrease from 5 K to 300 K of 64% is caused by the decrease in absorption. It is caused again by spectral broadening and a decrease in the electron population of A_1 at elevated temperatures as discussed for the responsivity of N1020. This depopulation comes along with an increased electron density in the ground state of the thickest last extractor QW (E_1 for N1021) giving rise to the $E_1 \rightarrow E_2$ absorption peak shown on the right side of figure 6.22 which absorbs 2.6% per double pass at 300 K (at 1985 cm^{-1}). In contrast to the $D_1 \rightarrow D_2$ ISBT of N1020 discussed above, the high temperature absorption in QW E of N1020 does not lead to a measurable photocurrent as no state in the active QW A is aligned with E_2.

Figure 6.23 shows the room temperature double pass absorption along with the corresponding responsivity spectra for all three samples. Using equation (3.1), an escape probability $p_e = 11\%$ is obtained for N1020 with a peak absorption $\eta = 14\%$, a peak responsivity $\mathcal{R}_{300\,K} = 4.27$ mA/W, and 30 periods. For N1021, $p_e = 6\%$ with $\eta = 14\%$ and $\mathcal{R}_{300\,K} = 1.7$ mA/W, and for N1022 $p_e = 12.5\%$ with $\eta = 9\%$ and $\mathcal{R}_{300\,K} = 1.5$ mA/W. Although higher than the $2 - 6\%$ escape probabilities of the 17 μm QCDs presented in section 6.3.1, this values are still low; an improved alignment between active QW and extractor would lead to higher absorption probabilities.

Figure 6.24 shows the Johnson noise limited detectivity for all three samples as function of temperature obtained with (2.47) using measured values for the responsivity $\mathcal{R}$ and the resistance - detector area product around 0 V R_0A; also shown are the constant background limited detectivities calculated with (2.48) using the measured absorption lineshape. The

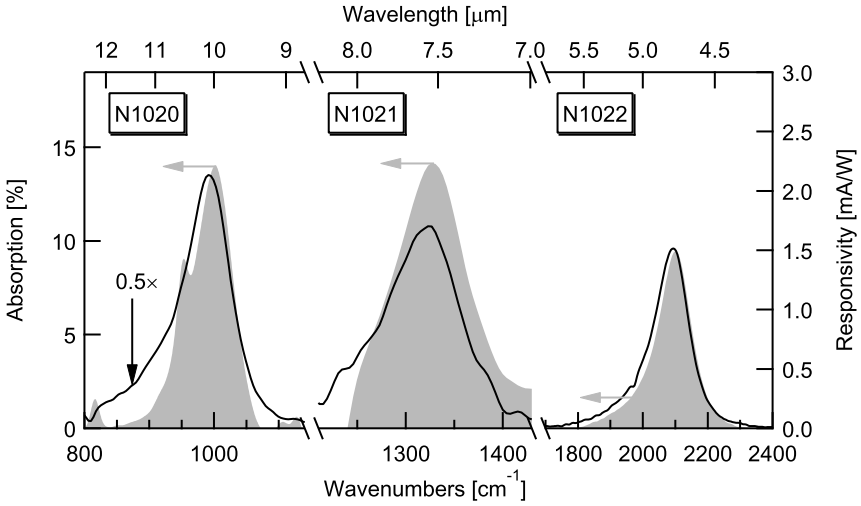

Figure 6.23: Absorption per double pass η and responsivity $\mathcal{R}$ of N1020, N1021, and N1022 at 300 K. Peak energy and FWHM of η and $\mathcal{R}$ agree very well.

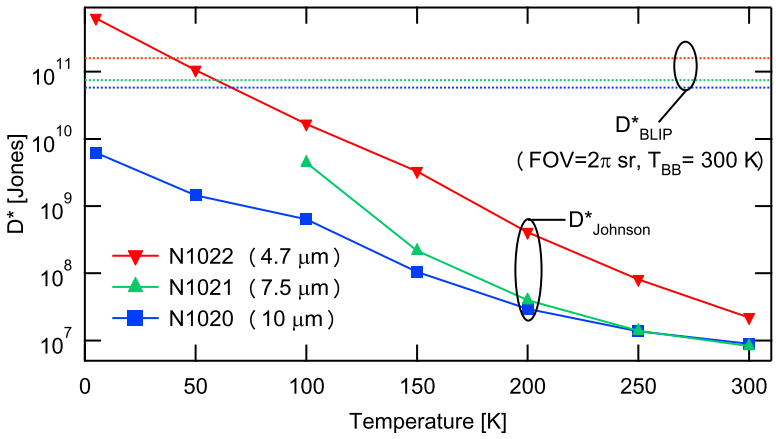

Figure 6.24: Detectivities $\mathcal{D}^*$ of N1020, N1021, and N1022 as function of temperature. $\mathcal{D}^*$ is Johnson noise limited except for N1022 below $T_{BLIP} = 45$ K. The dashed lines on top represent the background limited detectivity $\mathcal{D}^*_{BLIP}$ for a hemispherical field of view and a background temperature of 300 K.

detectivity of N1022 becomes background limited at T_{BLIP}=45 K, whereas T_{BLIP} is below 5 K for N1020 and N1021.

In conclusion, three QCDs at 10 µm, 7.4 µm, and 4.7 µm operating up to room temperature were demonstrated. The measured characteristics correspond very well to the nominal values, which proves the maturity of the $In_{0.53}Ga_{0.47}As$ / $In_{0.52}Al_{0.48}As$ material system as well as the robustness of the QCD design. Compared to the 10 µm bound to bound and bound to continuum QWIP presented in sections 6.1 and 6.2, the 10 µm QCD N1020 has a comparable detectivity $\mathcal{D}^*$ at temperatures below 50 K; in contrast to the two QWIPs, $\mathcal{D}^*$ has a slower decrease with temperature, wherefore a signal was observed up to 300 K. Compared to commercial liquid nitrogen cooled mercury-cadmium-telluride (MCT) detectors and GaAs / AlGaAs QWIPs, the $\mathcal{D}^*$ of the three presented QCDs is lower. At 5 µm, MCTs have a $\mathcal{D}^* = 1 \times 10^{11}$ Jones compared to 0.6×10^{11} for the 4.7 µm QCD N1022 at 75 K. At 10 µm, MCTs reach $\mathcal{D}^* = 5 \times 10^{10}$ Jones, whereas the 10 µm QCD N1020 reaches 0.1×10^{10} Jones at 75 K. To improve MIR QCDs, the escape probability, absorption efficiency, and device resistance should be increased. To obtain a higher resistance and absorption efficiency, the barrier thicknesses at the low-energy end of the extractor needs to be enlarged. By increasing the oscillator strength between the highest extractor ground state in resonance with the excited ground state of the active QW and the second highest extractor ground state, the escape probability can be improved. Also, the commercial potential in QCDs lies not in superior $\mathcal{D}^*$ but in high-speed photovoltaic operation in the infrared together with low-cost production by using well-established semiconductor materials.

Together with the 16.5 µm QCD presented in section 6.3.1, four devices spanning the MIR range were presented. Consequently, the realization of QCD's at any intermediate wavelength between 17 µm and 4.6 µm should be a straightforward task.

Chapter 7

Near Infrared Detectors

The near infrared (NIR), situated between visible light and MIR in the electromagnetic spectrum shown in figure 5.3, encompasses wavelengths between 0.8 µm and 5 µm. An industrially significant field for NIR photodetectors are long haul fiber communications, which depend on fast optoelectronic devices sensitive at 1.5 µm as the glass fiber attenuation is minimal at this wavelength. The second atmospheric window between $3 - 5$ µm is interesting for eye safe free space optical communication links, but also for high precision time of flight measurements used in 3D imaging.

To realize ISB photodetectors in the NIR, the semiconductor heterostructures presented in the previous chapter are not appropriate: for $In_{0.53}Ga_{0.47}As$ / $In_{0.52}Al_{0.48}As$ material with a CBO of 520 meV, the highest ISB energy between ground state and first excited state is around 320 meV for a QW thickness of 34 Å. For the GaAs / $Al_xGa_{1-x}As$ system with a CBO of up to 1 eV, the maximal E_{12} is 550.5 meV for a 22 Å QW with $x = 1$ and $E_{12} = 219.9$ meV for a 39 Å QW with $x = 0.39$ (for $x > 0.39$, the bandgap of $Al_xGa_{1-x}As$ becomes indirect). To reach higher ISBT energies, a material combination with a larger CBO is required.

There exist several alternative semiconductor heterostructures with large CBOs, each of whom has its own advantages and drawbacks: strain compensated $In_{x>0.53}Ga_{1-x}As$ / $In_{x<0.52}Al_{1-x}As$ builds upon the mature lattice matched $In_{0.53}Ga_{0.47}As$ / $In_{0.52}Al_{0.48}As$ system, but for a sufficient enhancement of the CBO, the large introduced strain severely hampers the growth. $In_{0.53}Ga_{0.47}As$ / $AlAs_{0.56}Sb_{0.44}$ is lattice matched to InP and has a CBO of 1.6 eV; however, growth of AlAsSb is less mature, the abruptness of its interface towards InGaAs is reduced by interdiffusion, and the conduction band minimum of AlAsSb is 789 meV lower in the X valley compared to the Γ valley. InAs / AlSb has a CBO of 2.1 eV, but suffers from strain. Group III nitrides (AlN, GaN, InN and their alloys) offer a large range of CBOs, for example 1.9 eV for AlN / GaN, and have a direct bandgap, but their large lattice mismatches and the lack of lattice matched substrates with low defect densities makes growth difficult.

In this chapter, NIR ISB photodetectors based on strain compensated InGaAs / InAlAs and on $In_{0.53}Ga_{0.47}As$ / $AlAs_{0.56}Sb_{0.44}$ are presented.

7.1 Strain compensated InGaAs / InAlAs quantum cascade detectors

As discussed in chapter 4, the CBO of an $In_xGa_{1-x}As$ / $In_yAl_{1-y}As$ heterostructure can be heightened from the lattice-matched value of 0.52 eV at $x = 0.53, y = 0.52$ by increasing x and decreasing y in a way that the strains of the barrier and the QW cancel each other with respect to the InP substrate.

E_{12}	n_{cnt}	n_{QW}	A	B	C	D	E	F	G	H
319	10^{18}	10^{18}	45/60	10/50	13/40	16/35	19/30	22/30	27/26	33/40

Table 7.1: Growth parameters of the strained InGaAs / InAlAs QCD along with the simulated detection energy E_{12} in meV and the Si doping densities in cm^{-3} of the contact layers (n_{cnt}) and of QW A (n_{QW}). The layer thicknesses are given in Å for one period in QW/barrier pairs which are alphabetically labeled according to the band diagram.

N1037 is a QCD with $In_{0.61}Ga_{0.39}As$ QWs and $In_{0.45}Al_{0.55}As$ barriers, which corresponds to a lattice mismatch of ±0.5% towards the InP substrate and results in a CBO of 610 meV [Faist et al., 1998]. MBE growth started with a 6000 Å thick $In_{0.53}Ga_{0.47}As$ lower contact layer lattice matched to the InP substrate, followed by 10 repetitions of the active region described in table 7.1. The structure is capped by a lattice matched 2000 Å thick $In_{0.53}Ga_{0.47}As$ upper contact layer. The MBE machine was calibrated to produce strain compensated layers for structures with equal amounts of barrier and QW material. As the active region of the presented QCD consists to 60% of barriers, it has a small residual strain of 0.1% towards InP. As expected for such small strains, the grown wafer showed no signs of relaxation

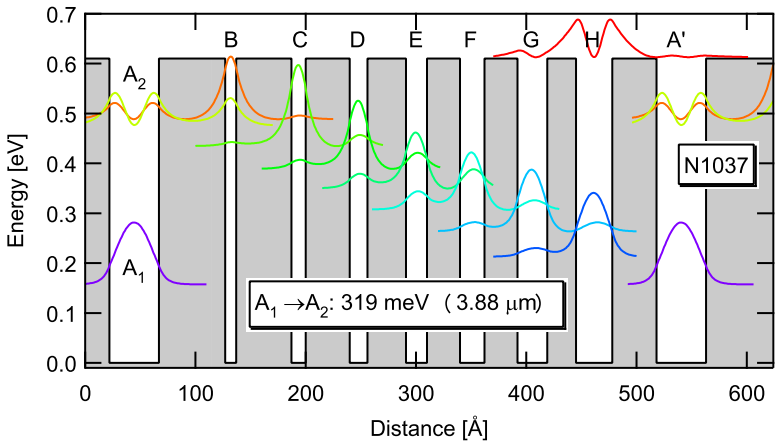

Figure 7.1: Simulated bandstructure of the strain compensated $In_{0.61}Ga_{0.39}As$ / $In_{0.45}Al_{0.55}As$ N1037 with a CBO of 610 meV designed for a detection energy of 319 meV.

The design of N1037 illustrated by the simulated conduction band diagram in figure 7.1 follows the QCD design criterions listed in section 3.2.2: the first excited state A_2 of the degenerately doped QW A is in resonance with the ground state of the first extractor

QW B and the ground states of the following extractor QWs C − H have a separation energy close to the InGaAs LO phonon energy (34 meV) to ensure an efficient vertical transport of photoexcited electrons.

For transmission measurements, a sample of N1037 was cleaved and polished into the 45° MPW geometry, whereas for current responsivity and current - voltage measurements, $(200\,\mu m)^2$ mesa contacts were additionally processed and contacted as described in section 5.1. Optical characterization was performed in a FTIR spectrometer using a KBr beamsplitter and glowbar illumination.

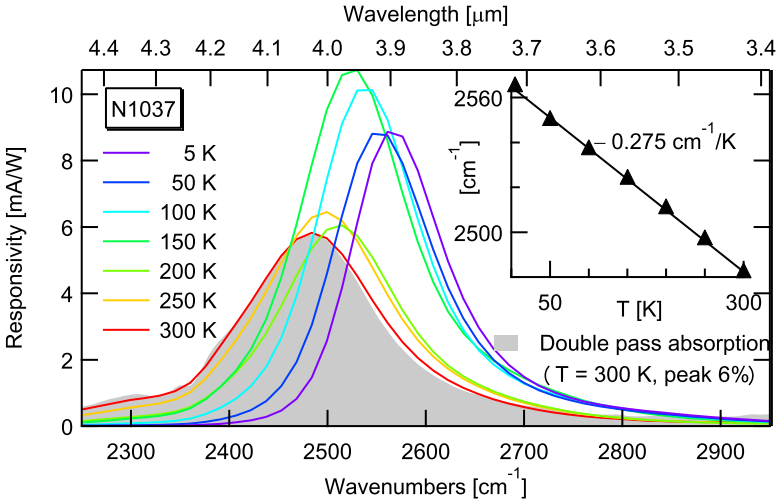

Figure 7.2: Responsivity spectra of the strained InGaAs QCD N1037 for different temperatures along with the room temperature absorption spectrum. The inset shows the peak responsivity position extracted from a fitted Lorentz curve as function of temperature; the straight line is a linear fit.

The measured responsivity shown in figure 7.2 amounts to 8.9 mA/W at 2565 cm^{-1} (318 meV / 3.9 μm) at 5 K. This corresponds well to the simulated $A_1 \rightarrow A_2$ ISBT energy of 319 meV, demonstrating that both growth and simulation of 0.5% strained InGaAs / InAlAs heterostructures have a high maturity comparable to lattice matched $In_{0.53}Ga_{0.47}As$ / $In_{0.52}Al_{0.48}As$. The spectral lineshape of the 300 K responsivity is identical to the one of the measured room temperature absorption also shown in figure 7.2. N1037's (fractional) responsivity linewidth increases from 113 cm^{-1} (4.4%) at 5 K to 164 cm^{-1} (6.6%) at 300 K. The linewidth broadening comes along with a peak absorption energy redshift of $-0.275\,cm^{-1}/K$ displayed in the inset of figure 7.2. Both broadening and redshift are due to band filling and non parabolicity as shown in figure 6.20 and correspond well to the analogous values of the lattice matched InGaAs / InAlAs QCDs presented in section 6.3.2. The responsivity is maximal at 150 K with 10.7 mA/W; this does not correspond to the typical monotonic QCD peak responsivity decrease with increasing temperature caused by ISB linewidth broadening and electron depopulation of the ground state A_1 as discussed in section 6.3.2. As the peak absorption decreases monolithically with increasing temperature, the photodetector gain must be temperature dependent, which again indicates a temperature dependent escape probability p_e. This behavior is not well understood and

was not further explored, as it did not occur in other QCDs investigated in this work.

Inserting the measured room temperature peak absorption per double pass of 6% and the corresponding peak responsivity of 5.8 mA/W into (3.1) results in a 30% escape probability p_e of photoexcited electrons in A_2 into the extractor. This is $2-3$ times higher compared to the lattice matched $In_{0.53}Ga_{0.47}As$ / $In_{0.52}Al_{0.48}As$ QCDs presented in section 6.3.2. This behaviour is consistent with N1037's higher tunneling transition probability T_e from the state A_2 and B_1 calculated using [Capasso et al., 1986]:

$$T_e = e^{-\sqrt{\frac{8m^* m_0 \Delta E q}{\hbar^2}} t_b}, \tag{7.1}$$

where ΔE is the barrier height and t_b the barrier thickness. For the 4.7 µm QCD N1022, $p_e = 12.5\%$ and $T_e = 1.3\%$, whereas for N1037, $p_e = 30\%$ and $T_e = 3.3\%$.

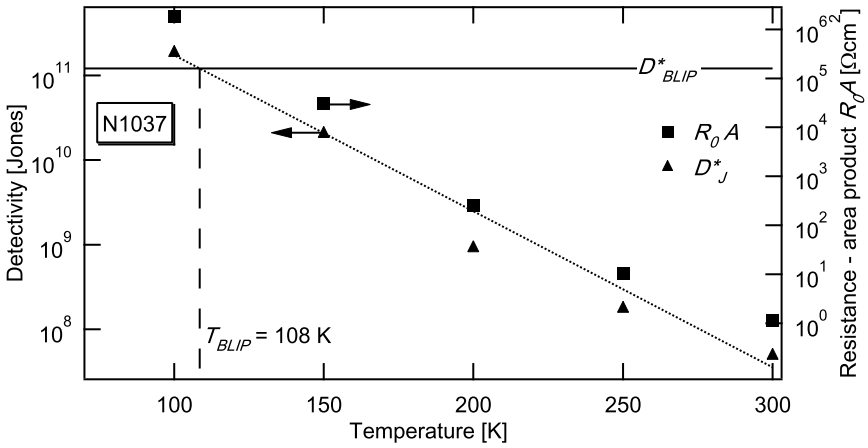

Figure 7.3: Johnson noise limited detectivity $\mathcal{D}^*_J$ and resistance area product around 0 V R_0A of the strained InGaAs QCD N1037 for different temperatures. $\mathcal{D}^*_J$ equals the background limited detectivity $\mathcal{D}^*_{BLIP}$ (FOV: 2π sr, 300 K background) at $T_{BLIP} = 113$ K.

The Johnson noise limited detectivity (2.47) $\mathcal{D}^*_J$ of N1037 was calculated with the measured resistance - area product displayed in figure 7.3 and the peak responsivities taken from figure 7.2. $\mathcal{D}^*_J$ equals 4.9×10^7 Jones at 300 K and reaches the background limited detectivity $\mathcal{D}^*_{BLIP} = 1.2 \times 10^{11}$ Jones (for 300 K background temperature and a hemispherical FOV) at $T_{BLIP} = 108$ K. This improvement over the longer wavelength QCDs presented in section 6.3.2, where only N1022 with a detection wavelength of 4.7 µm reached the BLIP condition at $T_{BLIP} = 45$ K, is expected: at shorter wavelengths, the higher electron states and thicker barriers of a QCD result in an increased resistance R and thus a lower Johnson noise current $i_n \propto \sqrt{R}$ and a higher $\mathcal{D}^* \propto 1/i_n$.

In conclusion, the QCD detection energy range of the lattice matched $In_{0.53}Ga_{0.47}As$ / $In_{0.52}Al_{0.48}As$ material system was extended towards higher energies by introducing a 0.5% strain between QW / barrier and the InP substrate without giving up on the good material quality. At 150 K, the presented $In_{0.61}Ga_{0.39}As$ / $In_{0.45}Al_{0.55}As$ QCD peaks at 3.96 µm with 10.7 mA/W. The BLIP condition is met at 108 K with $\mathcal{D}^* = 1.2 \times 10^{11}$ Jones, which is comparable to commercial photovoltaic InSb detectors such as the Judson technologies J10D series with a $\mathcal{D}^* = 7 \times 10^{10}$ Jones at 4 µm and 77 K. Thus, QCDs are an

interesting candidate for low-level light measurements at 4 µm. By further increasing the strain, InGaAs / InAlAs QCDs can be realized at shorter wavelengths. Faist et al. [1998] reported on a short wavelength quantum cascade laser based on $In_{0.7}Ga_{0.3}As$ / $In_{0.4}Al_{0.6}As$ QW / barriers with a CBO of 740 meV; this offset would allow for QCDs operating down to 2.9 µm(up to 430 meV).

7.2 InGaAs / AlAsSb quantum cascade detectors

To obtain ISB detectors working at wavelengths below 3 µm, the QCD design was applied to the $In_{0.53}Ga_{0.44}As$ / $AlAs_{0.56}Sb_{0.44}$ material system lattice matched to the InP substrate, which offers a CBO of 1.6 eV (see also section 4.3). Other advantages besides the high CBO are that the mature processing technology of the InGaAs / InAlAs system can be used, that growth of the InGaAs QWs is well established, and that high quality InP substrate is available at low cost; the difficulties lie in the growth of the $AlAs_{0.56}Sb_{0.44}$ barrier material and the barrier / QW interface quality. The samples presented in this section were grown by MBE at the Fraunhofer Institute for Applied Solid State Physics in Freiburg, Germany; their Varian Gen-II solid state MBE system is frequently used for growth of InGaAs / AlAsSb quantum cascade lasers emitting down to 3.7 µm [Yang et al., 2007] and was therefore a promising choice for the growth of the proposed short-wavelength QCDs. The bandstructure simulation for the InGaAs / AlAsSb structures were done at the Fraunhofer Institute for Applied Solid State Physics as well with a self-consistent Schrödinger-Poisson solver incorporating band-nonparabolicity through an energy dependent mass calculated with a three band model; material parameters are taken from Georgiev and Mozume [2001].

7.2.1 2 µm and 2.5 µm quantum cascade detectors

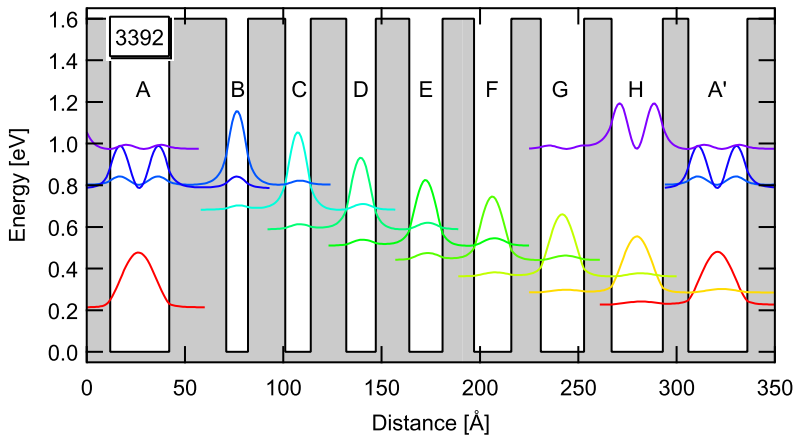

Figure 7.4: Simulated bandstructure of the InGaAs / AlAsSb QCD 3392 with a nominal $A_1 \rightarrow A_2$ detection energy of 572 meV (2.17 µm).

First, two QCDs designed for detection energies of 572 meV / 2.17 µm (3392) and 761 meV / 1.63 µm (3394) were investigated. The structures were grown on a semi-

insulating Fe-doped (001) InP substrate and consist of 20 repetitions of the active region described in table 7.2. It was sandwiched between two $In_{0.53}Ga_{0.47}As$ contact layers n-doped to $8 \times 10^{18}\,cm^{-3}$ with a thickness of 6000 Å between substrate and active region and 2000 Å above the active region. The simulated bandstructure of sample 3392 is shown in figure 7.4.

	A	B	C	D	E	F	G	H	J	K
3392	30/26	11/19	13/18	15/17	17/16	19/15	22/14	26/13	–	–
3394	23.4/30	7/25	8/22	9/21	10/20	12/19	14/17	16/16	18/15	20/13
3403	24.5/23	11/19	12.5/18	14/17	16/16	18/15	20/14	22/13	18/15	20/13

Table 7.2: Growth parameters of the InGaAs / AlAsSb QCDs 3392 with a nominal detection energy $E_{12} = 572\,meV$ and 3394 with a nominal $E_{12} = 761\,meV$; 3403 is designed for $E_{12} \approx 570\,meV$ based on the results of 3392. The layer thicknesses are given in Å for one period in QW/barrier pairs which are alphabetically labeled according to the band diagrams; all layers are undoped except for QW A which is n-doped to $2 \times 10^{18}\,cm^{-3}$.

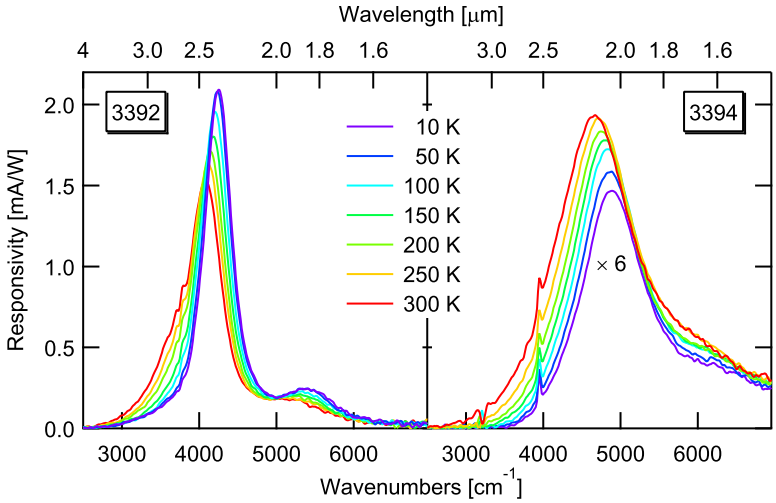

Figure 7.5: Responsivity spectra of AlAsSb QCDs for different temperatures. Left panel: 3392 detecting around $4065\,cm^{-1}$ (2.45 μm). The shoulder at $5500\,cm^{-1}$ is due to the diagonal transition from the active QW's ground state A_1 into the last extractor QW's excited state H_2. Right panel: responsivity of 3394 detecting around $4880\,cm^{-1}$ (2.05 μm) scaled by a factor of 6.

For characterization, $(200\,\mu m)^2$ square mesa structures were processed onto both samples and a 45° facet was polished as described in section 5.1. Figure 7.5 shows the responsivity spectra measured with the FTIR spectrometer using glowbar illumination in combination with a KBr beamsplitter.

Table 7.3 lists the responsivity peak position, value, and FWHM for 3392 and 3394. The responsivity peaks at 605 meV / 2.05 μm for 3394 and at 528 meV / 2.35 μm for 3392; those are the highest operating QCD energies obtained in this work. Compared to the

	E_{12} [meV]	2Γ [meV]	$\mathcal{R}_p$ [mA/W]
3392	5 K: 528, 300 K: 505	5 K: 52, 300 K: 71	5 K: 2.09, 300 K: 1.53
3394	5 K: 606, 300 K: 580	5 K: 124, 300 K: 157	5 K: 0.24, 300 K: 0.32

Table 7.3: Peak position E_{12}, FWHM 2Γ, and peak value $\mathcal{R}_p$ of the measured responsivity spectra of the AlAsSb QCDs 3392 and 3394 taken from figure 7.5.

simulated E_{12} ISBT energies, the measured values are however lower by 8% (3392) respectively 20% (3394). The increase of the deviation between measured and simulated ISBT energy for decreasing QW thickness is consistent with the findings of Neogi et al. [2000], who investigated ISB absorption in InGaAs / AlAsSb QWs with varying thicknesses. They observed a minimal ISBT energy of 650 meV as opposed to the theoretical 920 meV for a QW thickness of 14.5 Å; this discrepancy is explained by the influence of interface fluctuations between QW and barrier as shown in figure 7.6 [Cristea et al., 2006]. Interface roughness is also the reason for the wide fractional responsivity linewidth of 10%

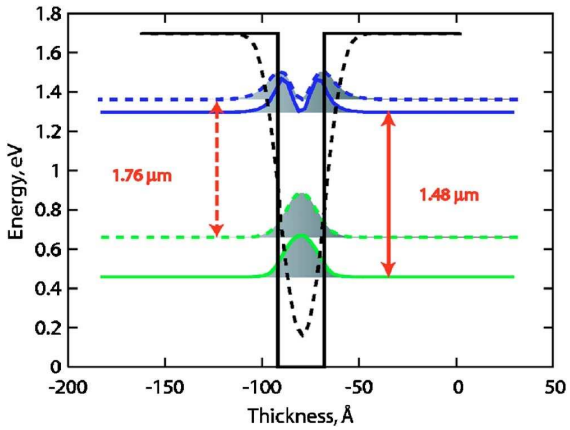

Figure 7.6: Conduction band simulation of a 24 Å thick strained $In_{0.78}Ga_{0.22}As$ QW with $AlAs_{0.56}Sb_{0.44}$ barriers taken from Cristea et al. [2006]. Solid lines represent an ideal QW resulting in a transition wavelength of 1.48 µm, dashed lines include QW / barrier interdiffusion through a graded potential, resulting in a redshifted transition wavelength of 1.76 µm.

at 5 K for 3392 and even 20% for 3394; comparable longer-wavelength $In_{0.53}Ga_{0.47}As$ / $In_{0.52}Al_{0.48}As$ QCDs presented in this work have significantly narrower linewidths, such as the 4.7 µm QCD N1022 discussed in section 6.3.2 with 3.7% at 5 K.

The weak shoulder of 3392's responsivity peaking at 5400 cm^{-1} (670 meV) with 0.25 mA/W at 5 K can be assigned to the diagonal $A_1 \rightarrow H_2$ transition followed by the $H_2 \rightarrow A_2 \rightarrow$extractor path: due to the small barrier between QW H and A, the oscillator strength $f_{osc}^{A_1,H_2} = 0.106$ is sufficient to lead to a measurable photocurrent.

The observed redshift with increasing temperature of the peak position is characteristic for ISBTs and described in detail in section 6.3.2. For 3392, the decrease in peak responsivity $\mathcal{R}_p$ is compensated by the broadening of the FWHM 2Γ, wherefore the total absorption efficiency $\eta \propto \mathcal{R}_p\Gamma$ is not temperature dependent. The responsivity of 3394

however increases for higher temperatures, which is opposed to the decrease observed for the other QCDs presented in this work. Due to 3394's weak absorption of 1.2% (described below), its temperature dependence could not be explored, and the origin of 3394's unusual responsivity increase remains unclear.

For absorption measurements, 3392 and 3394 were cleaved and polished into 3 mm long 45° MPW geometries. The measured room temperature absorptions peak at 518 meV for 3392 and at 585 meV for 3394, which is in good agreement with the measured peak responsivity energies. The measured peak absorptions per double pass of 3% for 3392 and 1.2% for 3394 also agree well with the values calculated using Fermi's golden rule (2.27) of 2.95% for 3392 and 0.84% for 3394. This weak absorption efficiency $\eta_{A_1}^{A_2,B_1}$ is caused by the low ($A_1 \rightarrow A_2$, $A_1 \rightarrow B_1$) oscillator strengths f_{osc} of (0.225, 0.0598) for 3392 and (0.158, 0.114) for 3394. As the oscillator strengths obey the sum rule $\sum_F f_{osc}^{A_1 F} = cst.$ [Sirtori et al., 1994], a reduction of $f_{osc}^{A_1 H_1} = 0.367$ and $f_{osc}^{A_1 H_2} = 0.106$ would result in an increase of $\eta_{A_1}^{A_2,B_1}$. A stronger $\eta_{A_1}^{A_2,B_1}$ was indeed observed for samples EP745 and 3505 presented later in this section, which have a thicker barrier between QW H and A compared to 3392.

By inserting the measured peak responsivity and absorption into (3.1), an escape to capture probability ratio p_e/p_c of 0.51 for 3392 respectively 0.46 for 3394 is computed; as p_c is close to unity for QCDs, this results in an escape probability around 50% for both devices. This is higher than the p_e reported for the InGaAs / InAlAs QCDs presented earlier in this work.

The Johnson noise limited detectivity $\mathcal{D}^*$ of 3392 and 3394 was calculated with (2.47) using measured values for the peak responsivity $\mathcal{R}_p$ and the resistance - area product R_0A around 0 V. At 300 K, 3392 has an R_0A of 47.9 Ωcm^2 resulting in a $\mathcal{D}^*$ of 8.2×10^7 Jones; the corresponding values for 3394 are $R_0A = 24.5\,\Omega\text{cm}^2$ and $\mathcal{D}^* = 1.2 \times 10^7$ Jones. Both R_0A and $\mathcal{D}^*$ are shown in figure 7.12 for different temperatures. The background limited detectivity $\mathcal{D}^*_{BLIP}$ given by (2.48) is calculated for a 300 K background and a hemispherical field of view and amounts to 1.15×10^{12} Jones for 3392 respectively 1.47×10^{11} Jones for 3394. As the R_0A measurements are limited by the maximal source meter sensitivity of 5 pA to values below $\sim 10^7\,\Omega\text{cm}^2$, the measured $\mathcal{D}^*$ are extrapolated to determine the temperature T_{BLIP} at which the condition $\mathcal{D}^* = \mathcal{D}^*_{BLIP}$ is met. The thus obtained values are $T_{BLIP} = 5$ K for 3392 and $T_{BLIP} = 70$ K for 3394. The higher T_{BLIP} of 3394 is explained by its shorter operation wavelength, resulting in a higher R_0A and thus a higher detectivity. Both 3392 and 3394 have a low T_{BLIP} compared to the strained InGaAs QCD N1037 presented in section 7.1 with $T_{BLIP} = 108$ K. The reason for this low performance is found in the weak absorption efficiency of 3392 and 3394.

Based on the assumption that the discrepancy between measured and simulated detection energy of 3392 is caused by interface fluctuations as shown in figure 7.6, a redo of 3392 was grown and investigated: 3403 has a 24.5 Å thick main QW (3392: 30 Å), whereas the first extractor QW is identical to the one of 3392; the detailed layer thicknesses of 3394 are listed in table 7.2. 3403 peaked at 600 meV (2.07 µm), thus showing a monotonic relation between transition energy and QW thickness together with 3392 and 3394. The responsivity amounts to 0.16 mA/W at 5 K, which is twice as low than for 3394; this is caused by less efficient extraction of the photoexcited electrons from the active QW due to a bad alignment of the extractor, as the thinner active QW lifts the excited state A_2 above the ground state B_1 of the first extractor QW.

7.2.2 Variations of the 2.5 µm quantum cascade detector

To obtain a better understanding of the InGaAs / AlAsSb QCD conduction band profile, five variations of the 2.5 µm QCD 3392 were designed and investigated. The lower wavelength QCD 3392 presented in the previous section was chosen as design template due to its weaker deviation from the simulated values, narrower linewidth, and thicker QWs compared to 3394.

3411, 3412 In order to determine the sensitivity of the coupling between the electron states A_2 and B_1, which affects the extraction efficiency and thus the responsivity, on the thickness d_B of the first extractor QW B, a sample with $d_B = 11.7$ Å (3411) and one with $d_B = 10.3$ Å (3412) were grown. Additional changes compared to 3392 are an 8% thinner barrier between QW A and B to increase the A_2−B_1 miniband width and a 21% thicker last extractor barrier to reduce the undesired $A_1' \rightarrow H_2$ shoulder at 670 meV found in the responsivity spectrum of 3392. The growth parameters of the active region are listed in table 7.4. Figure 7.7 shows the room temperature responsivity of 3411 and 3412 compared

	n_{cnt}	n_{QW}	A	B	C	D	E	F	G	H
3392	8	2	30/26	11/19	13/18	15/17	17/16	19/15	22/14	26/13
3411	2/8	2	30/24	11.7/19	13.2/18	15/17	17/16	19/15	22/14	26/17
3412	2/8	2	30/24	10.3/19	12/18	14/17	16.2/16	19/15	22/14	26/17
EP745	1	2	30/24	11/19	13/18	15/17	17/16	19/16	22/17	26/23
3504	0.5	1	30/24	11/19	13/18	15/17	17/16	19/18	22/20	26/26
3505	0.5	2	30/24	11/19	13/18	15/17	17/16	19/18	22/20	26/26

Table 7.4: Growth parameters of the InGaAs / AlAsSb QCDs based on 3392. n_{cnt} is the n-doping of the lower / upper contact layer and n_{QW} of the active QW A, both in units of $10^{18}\,cm^{-3}$. The layer thicknesses are given in Å for one period in QW/barrier pairs which are alphabetically labeled according to the band diagram shown in figure 7.4. For comparison, the data of 3392 is restated.

to 3392. The high energy shoulder of 3392 which has its origin in the $A_1' \rightarrow H_2$ transition is reduced for 3411 and 3412. As expected, their thicker barrier between QW H and A' resulted in a lower $A_1' \rightarrow H_2$ oscillator strength of $f_{osc} = 0.066$. The otherwise identical spectral shape of the three samples attest to a good reproducibility of the growth.

The responsivities of 3411 and 3412 are nearly identical, wherefore the ±6% variation of the QW B thickness d_B has only a weak impact on the extraction efficiency. According to the Schrödinger band structure simulation, a 6% deviation of d_B from the optimal thickness results in a 50% reduction of the A_2 - B_1 oscillator strength; if 3411 and 3412 have a d_B above respectively below the optimal thickness, their A_2 - B_1 oscillator strengths and thus responsivity differ by $0-50\%$. Therefore, the nearly equal responsivities of both 3411 and 3412 indicate that the optimal d_B is around 11 Å, which corresponds to the nominal value of d_B for sample 3392.

EP745 Based on the results of 3411 and 3412, a redo of 3392 with thicker extractor barriers, especially between QW H and A', was designed to further suppress the high

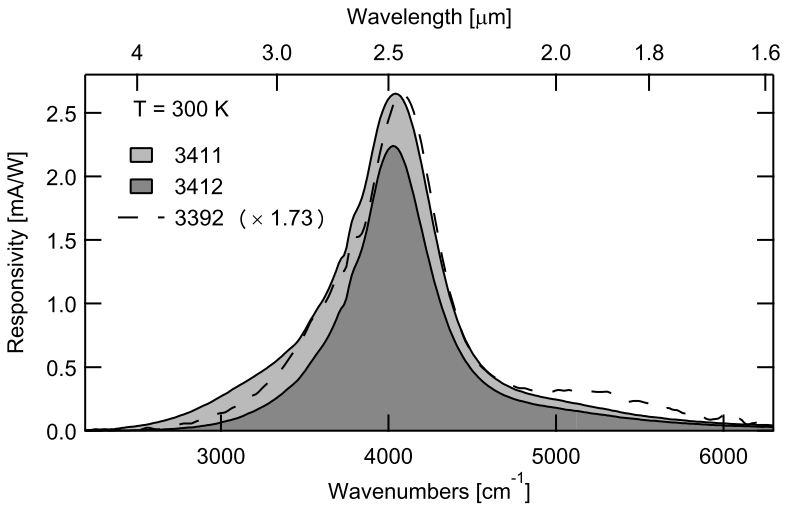

Figure 7.7: Responsivity spectra of AlAsSb QCDs 3411 with a extractor QW B thickness $d_B = 11.7\,\text{Å}$ and 3412 with $d_B = 10.3\,\text{Å}$. For comparison, the responsivity of 3392 with $d_B = 11\,\text{Å}$ is given.

energy shoulder of 3392; another benefit of the thicker barrier between QW H and A' is the higher oscillator strength and thus absorption efficiency between A_1 and A_2 respectively B_1, as described in the discussion of 3392's absorption. The overall extraction efficiency does not suffer from a thicker barrier at the low-energy end of the extractor: once an extracted electron reaches the thicker barrier, its recapture probability into the active QW from where it originated is negligible.

EP745, described in table 7.4 was grown at the ETH Zurich on a Veeco GEN II MBE system. As described by Cristea et al. [2005], AlAs diffusion barriers were introduced at the QW / barrier interfaces to reduce the Sb segregation between QW and barrier.

The responsivity of EP745 is shown in figure 7.8. Compared to 3392, two main differences are observed: the linewidth of EP745 is 35% smaller and the high energy shoulder at $5400\,\text{cm}^{-1}$ is not present in EP745's responsivity. This shows that both the AlAs interdiffusion barriers at the interfaces and the thicker barrier between QWs H and A' have the expected effect of improving the interface abruptness and lowering the A'$_1 \rightarrow$H$_2$ oscillator strength.

The AlAs diffusion barriers used in EP745 lead to a significantly higher device resistance compared to the other AlAsSb 2.5 μm QCDs: at 200 K, the resistance - area product around 0 V (R_0A) is $8.9\times10^6\,\Omega\text{cm}^2$ for EP745 compared to $4300\,\Omega\text{cm}^2$ for 3392. Figure 7.9 shows the measured current density as function of applied voltage for EP745; below 200 K, the current close to 0 V of the $(200\,\mu\text{m})^2$ device drops below the multimeter sensitivity of about 5 pA wherefore R_0A cannot be extracted at low temperatures. As a consequence of the high R_0A, the Johnson current noise is low and the Johnson noise limited detectivity $\mathcal{D}^*$ (2.47) is high, namely 2.9×10^{10} Jones at 200 K. If the calculated D^* are extrapolated towards lower temperatures, $\mathcal{D}^*$ equals the 300 K background limited hemispherical $D^*_{BLIP} = 1.15 \times 10^{12}$ Jones at $T_{BLIP} = 100\,\text{K}$; therefor, EP745 has the highest R_0A, $\mathcal{D}^*$, and T_{BLIP} of all InGaAs / AlAsSb QCDs characterized in this chapter.

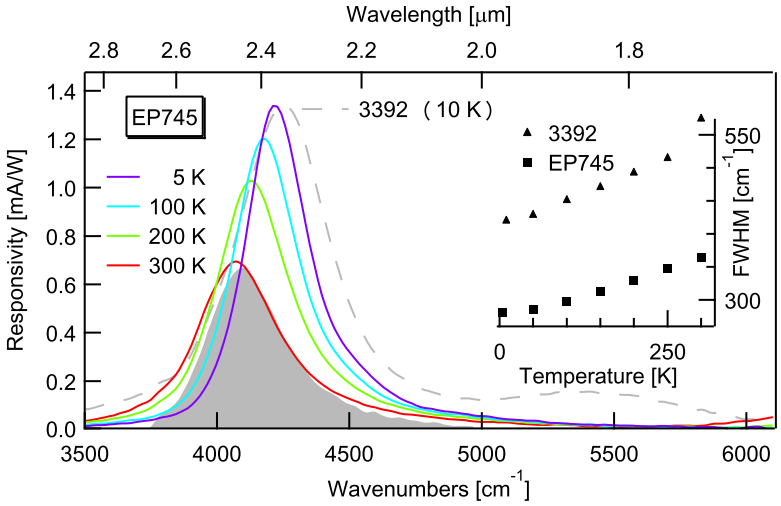

Figure 7.8: Responsivity of AlAsSb QCD EP745 at different temperatures (solid lines). The dashed line is the responsivity of 3392 at 10 K scaled by a factor 0.64. The shaded area is the room temperature absorption per double pass of EP745 with a peak value of 3.4%. The inset compares the FWHM of EP745 to 3392.

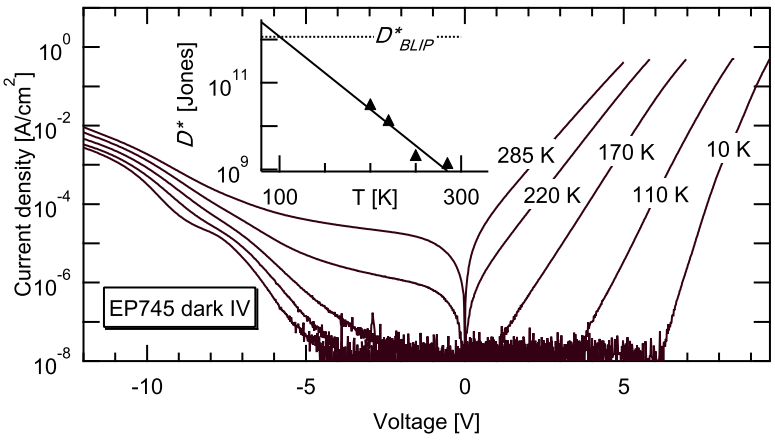

Figure 7.9: Dark current density of EP745 for different temperatures. The inset shows the Johnson noise limited detectivity $\mathcal{D}^*$ calculated with the measured responsivity and resistance (triangles) and an exponential fit of $\mathcal{D}^*$ (solid line).

3504, 3505 To evaluate the impact of the doping density n_{3D}^A in the active QW A on absorption, responsivity, resistance, and detectivity, a pair of 3392 redos with $n_{3D}^A = 1 \times 10^{18}\,\mathrm{cm}^{-3}$ (sample 3504) and $n_{3D}^A = 2 \times 10^{18}\,\mathrm{cm}^{-3}$ (sample 3505) were grown in Freiburg. The detailed structure, which has again thicker barriers at the lower end of the extractor, is listed in table 7.4.

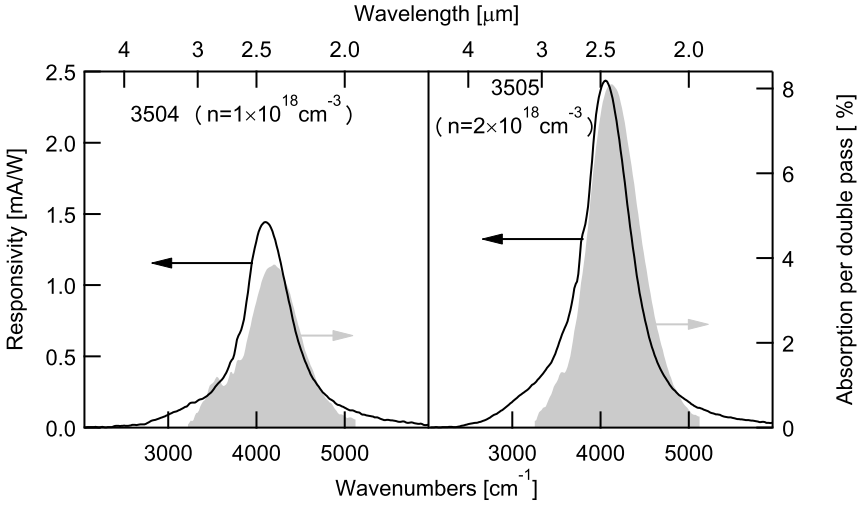

Figure 7.10: Room temperature responsivity (black solid line) and absorption (grey shaded area) for AlAsSb QCDs with different doping levels n_{3D}^A in the active QW A. Left panel: 3504 ($n_{3D}^A = 1 \times 10^{18}\,\mathrm{cm}^{-3}$). Right panel: 3505 ($n_{3D}^A = 1 \times 10^{18}\,\mathrm{cm}^{-3}$).

The measured room temperature absorption and responsivity of 3504 and 3505 are shown in figure 7.10. The absorption peak value η_p is 3.8% per double pass for 3504 and 8% for 3505; as η_p is proportional to the doping level n_{3D}^A in QW A, this shows that the effective n_{3D}^A is twice as high for 3505 than for 3504, in accordance with the nominal values of $n_{3D}^A = 1 \times 10^{18}\,\mathrm{cm}^{-3}$ for 3504 respectively $n_{3D}^A = 2 \times 10^{18}\,\mathrm{cm}^{-3}$ for 3505. The measured absorption is also in reasonable accordance with the calculated values of 9.5% for 3505 and 4.8% for 3504, corrobating the simulated oscillation strengths $f_{osc}^{A_1A_2} = 0.323$ and $f_{osc}^{A_1B_1} = 0.255$. The significant increase compared to 3392 ($f_{osc}^{A_1A_2} = 0.225$ and $f_{osc}^{A_1B_1} = 0.060$) is due to 3505s and 3504s thicker barrier between QW H and A, as discussed above.

The 300 K peak responsivity $\mathcal{R}_p$ is 69% stronger for 3505 (2.44 mA/W) than for 3504 (1.44 mA/W); as $\mathcal{R}_p = q/(h\nu) g_d \eta_p$ and $\eta_p^{3505}/\eta_p^{3504} = 2$, the photodetector gain g_d is thus 18% higher for 3504 than for 3505. This small difference can be caused by processing variations (for example of the 45° facet's surface roughness) and growth variations of layer thickness and interface quality. Another effect of 3505's higher doping level is a decrease of the device resistance, namely $R_0A = 31.9\,\Omega\mathrm{cm}^2$ at 300 K compared to $186\,\Omega\mathrm{cm}^2$ for 3394. The opposite changes of R_0A and $\mathcal{R}$ result in similar detectivities for both 3504 and 3505, namely 8.6×10^7 Jones respectively 11×10^7 Jones at 300 K. $\mathcal{D}^*$ and R_0A of both samples are summarized for different temperatures in figure 7.12

The spectral shape of 3505's photocurrent was studied under application of an external field. The top panel of figure 7.11 shows measured spectra of 3505 for different applied

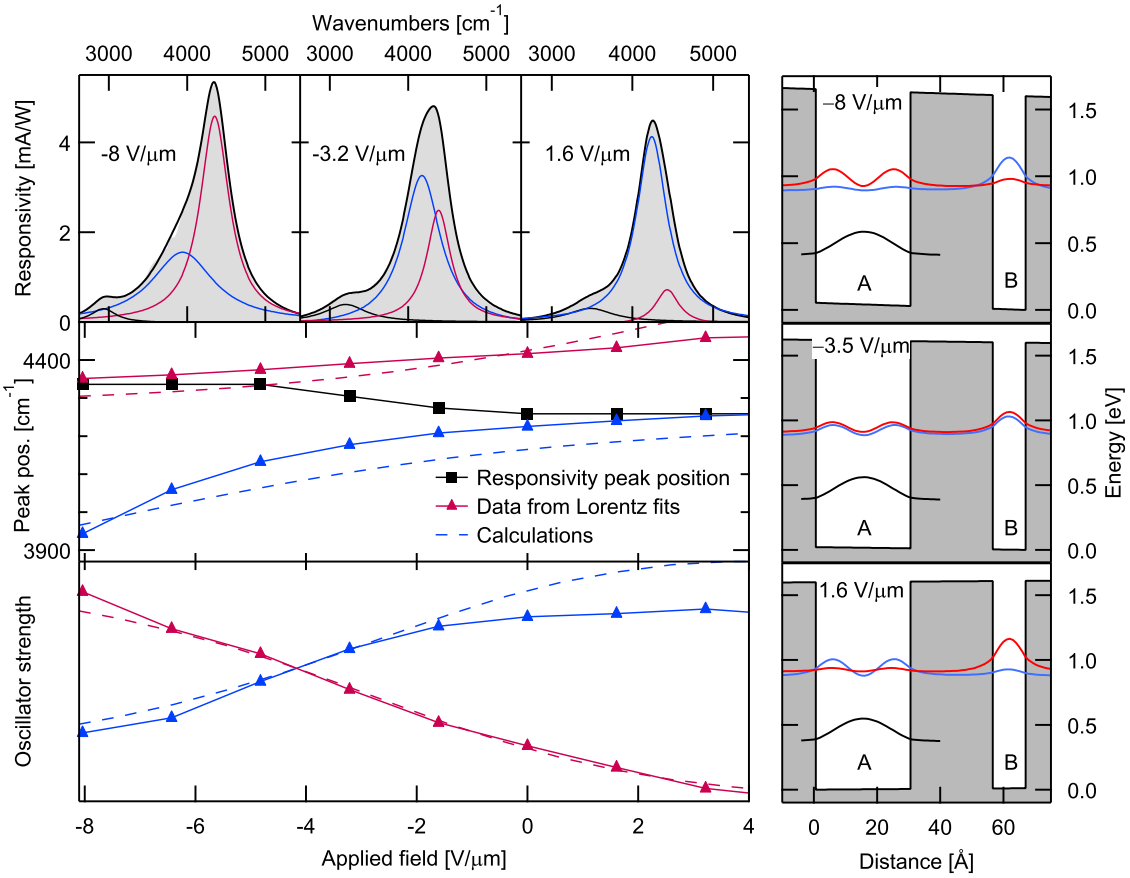

Figure 7.11: Anticrossing of 3505 under bias at 10 K. The top three panels show the responsivity spectra measured at different bias voltages (grey shaded area) superimposed by a fit (black line) consisting of three Lorentzians (black, blue, and red line). The center panel compares the peak positions of the two Lorentzians (red and blue triangles) to the simulated transition energies (red and blue dashed line). The lower panel compares the amplitude of both Lorentzians (red and blue triangles) to the calculated oscillator strengths from the ground state to the upper states. The three vertically aligned panels to the far right show the conduction band simulations at different bias voltages, in accordance with the top three panels.

fields, as well as a fit consisting of three Lorentzians. The weak black Lorentzian at the lowest energy shows a linear Stark shift of 75 eV/(V/Å), corresponding to the distance between the center of QW A and C (75.5 Å); therefore it is attributed to the $A_1 \rightarrow C_1$ transition. The two Lorentzians at higher energies correspond to the transitions between the ground state A_1 and the coupled states A_2 and B_1; they exhibit an anticrossing if the amplitude of the applied field is modified: in the strongly negative field regime, the low-energy transition is localized in QW B resulting in a linear Stark shift and a low transition probability from A_1 (which is proportional to the oscillator strength f_{osc}). In contrast the high energy transition is localized in QW A, does not shift, and has a high f_{osc}. For low fields, both wave functions are localized in QWs A and B, have a non-linear Stark shift and comparable oscillator strength. For strongly positive fields, finally, the low energy wave function is localized in QW A, does not Stark shift and has a high f_{osc}, whereas the high energy wavefunction is localized in QW B, exhibits a linear Stark shift and a low f_{osc}. As seen in the center panel of figure 7.11, the measured peak detection energies of the two Lorentzians correspond well to the ones obtained by band structure simulations. The lower panel of figure 7.11 compares the amplitude of the measured Lorentzians with the simulated oscillator strength, again showing a good qualitative agreement between experiment and simulation. The somewhat counter intuitive shift of the overall peak responsivity, also shown in the center panel of figure 3, is caused by anticrossing; its direction is opposite to the $A_1 \rightarrow C_1$ Stark shift. The observation of anticrossing shows that a very good alignment between A_2 and B_1 was achieved.

In conclusion, short-wavelength QCDs operating down to 2 µm respectively up to 606 meV (sample 3394) based on lattice matched $In_{0.53}Ga_{0.47}As$ / $AlAs_{0.56}Sb_{0.44}$ on InP were designed and investigated. The low absorption efficiency of initial samples (3.8% per double pass for 3392 respectively 1.2% for 3394) was improved for later devices by increasing the thickness of the last extractor barrier, which resulted in lower coupling between the active QW's ground state and the states of the last extractor QW, which in turn increases the oscillator strength between ground and first excited state in the active QW. It was shown that an increase of device resistance by two orders of magnitude and a 35% smaller linewidth are obtained by introducing AlAs interface diffusion barriers between InGaAs QWs and AlAsSb barriers for sample EP745. This sample has also the highest detectivity ($\mathcal{D}^* = 1.28 \times 10^9$ Jones at 300 K) and T_{BLIP} (100 K, $\mathcal{D}^*_{BLIP} = 1.15 \times 10^{12}$ Jones) of all InGaAs / AlAsSb QCDs investigated in this work. For wavelengths below 2.5 µm, commercial InGaAs interband photodetectors are available which show significantly better performance: the Judson technologies J23-xxx-2.6 with a 50% cutoff wavelength of $\lambda_c = 2.6$ µm has a room temperature $\mathcal{D}^* = 6 \times 10^{10}$ Jones, which increases to $\mathcal{D}^* = 3.6 \times 10^{12}$ Jones for a Peltier-cooled device with an operating temperature of 188 K. At this temperature, InAs detectors with $\lambda_c = 3.3$ µm have similar $\mathcal{D}^*$. As both InAs and InGaAs are close to the theoretical limit of $\mathcal{D}^*$ and have mature and cost-efficient material growth and processing, possible commercial interest to ISB photodetectors at wavelengths below 3.3 µm narrows down to applications which require fast detection speed or intrinsically narrow linewidths. One example is 3D imaging based on the time-of-flight distance measurement principle, where the depth resolution is proportional to the light pulse frequency. Thanks to their small linewidth, QCD stacks detecting at slightly different wavelengths would provide a rough estimation on spectral composition without requiring a

grating or interferometric spectrometer; a large prospective market for NIR spectroscopy is non-invasive determination of Glucose concentration in human blood by measuring glucose absorption features around 3 µm.

Anticrossing of two quantized electron levels was observed in the photoresponse of sample 3505 when applying varying bias voltages, demonstrating both good material quality and a high confidence level of the band structure simulations.

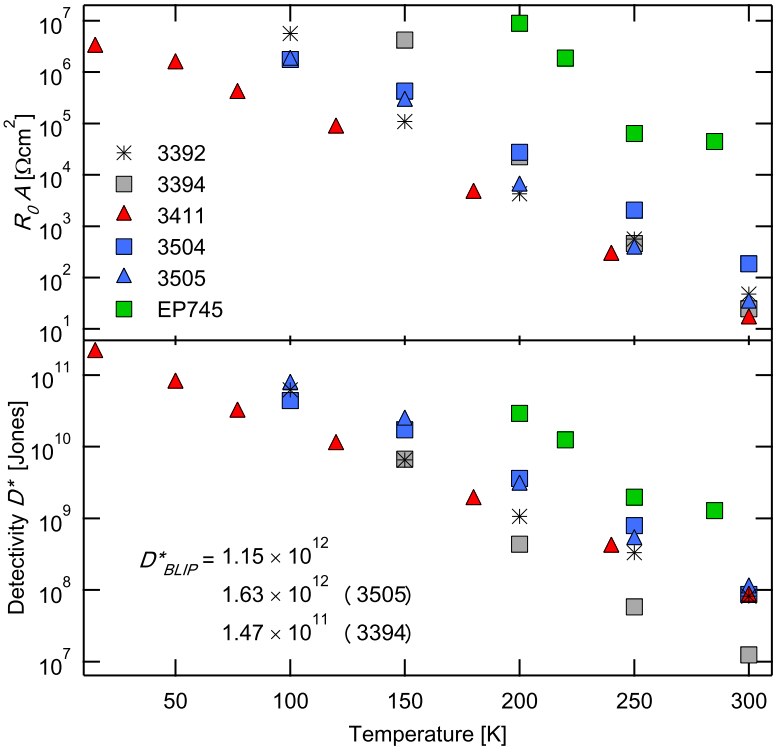

Figure 7.12: Top panel: measured resistance - area product around 0 V (R_0A) for different AlAsSb QCDs; the maximal source meter sensitivity of 5 pA limits this measurement to values below about $10^7\,\Omega\mathrm{cm}^2$. Bottom panel: Johnson noise limited detectivity calculated using the R_0A shown on top and the measured peak responsivity. The indicated D^*_{BLIP} is calculated for a 2π sr FOV and a 300 K background temperature based on the measured absorption which barely varies between the samples except for 3505 and 3394.

The Johnson noise limited detectivities $\mathcal{D}^*$ of the investigated samples are summarized in figure 7.12. With $\mathcal{D}^* = 1.28 \times 10^9$ Jones at 285 K, EP745 has the highest detectivity due to its large resistance; 3394 has the lowest detectivity ($\mathcal{D}^* = 1.25 \times 10^7$ Jones at 300 K) due to its low responsivity.

Detection wavelengths below the reported 2 µm using the $In_{0.53}Ga_{0.47}As/AlAs_{0.56}Sb_{0.44}$ material system can be obtained by reducing the In content in the QW while additional AlAs layers at the QW / AlAsSb barrier both compensate the strain and act as diffusion barriers between the InGaAs QW and the AlAsSb barrier. With this approach, Cristea et al. [2006] obtained ISB absorption at 1.76 µm for a 14.5 Å thick $In_{0.78}Ga_{0.22}As$ QW with 8.7 Å thick AlAs diffusion barriers. To reach the industrially significant wavelength range

of 1.3 µm−1.5 µm, the interface abruptness must be further improved; one approach is to lower the MBE growth temperature, which reduces the barrier / QW interdiffusion with the drawback of inferior crystalline quality.

Chapter 8

Conclusions and Outlook

Conclusion In this work intersubband photodetectors in the mid and near infrared were designed and investigated. The emphasis was put on the quantum cascade detector (QCD). Due to its photovoltaic operation scheme, it does not require an external voltage bias and is not subject to dark current noise. The QCD operation principle is based on an asymmetric conduction band potential formed by a series of quantum wells (QWs) with increasing thicknesses called extractor. Similar to the externally applied electric field in a photoconductive QW infrared photodetector (QWIP), this asymmetry results in a preferential vertical transport direction for photoexcited electrons and thus in a measurable photocurrent. QCDs were demonstrated at detection wavelengths λ_0 between 2 µm and 17 µm based on different semiconductor materials.

The design of QCD devices was shown to be robust and reliable. The detection wavelength of the presented InGaAs / InAlAs QCDs corresponds very well to the values calculated with a numerical Schrödinger solver based on the nominal layer thicknesses. The high material quality resulted in small fractional detection linewidths down to 3.7%.

The longest λ_0 demonstrated in this work is 17 µm. For QCDs with efficient phonon assisted extraction cascades, detection energies below 70 meV (corresponding to $\lambda_0 >$ 17 µm) are impractical: the low detection energy results in less QWs and barriers in the extractor and thus a lower device resistance and detectivity. For the 17 µm QCDs, this problem was alleviated by replacing an extractor QW with a miniband formed by the ground states of multiple QWs / barriers of identical thickness.

The detection range of QCDs was extended towards shorter wavelengths both by introduction of strain to the InGaAs / InAlAs system or by replacing the InAlAs barriers with $AlAs_{0.56}Sb_{0.44}$. With the first approach, a detection wavelength of 4 µm was obtained, which is in good agreement with simulations. The second approach yielded even shorter detection wavelengths down to $\lambda_0 = 2$ µm; however, these λ_0 were redshifted compared to the simulated value of 1.63 µm due to graded interfaces originating from Sb segregation between the InGaAs QW and the AlAsSb barrier.

Figure 8.1 shows the detectivities of the investigated QCDs along with two photoconductive QWIPs also characterized in the course of this work. The 17 µm QCD N973 has a detectivity $\mathcal{D}^*$ of 1×10^{11} Jones at 5 K. This high detectivity demonstrates the advantage of a narrow linewidth photodetector in this wavelength range: the $\mathcal{D}^*$ of a broad band photodetector with a cutoff wavelength of $\lambda_c = 17$ µm can not be higher than the photon noise limited $\mathcal{D}^*_{BLIP} = 0.47 \times 10^{11}$ Jones. The $\mathcal{D}^*$ of an ISB detector with a 6% fractional

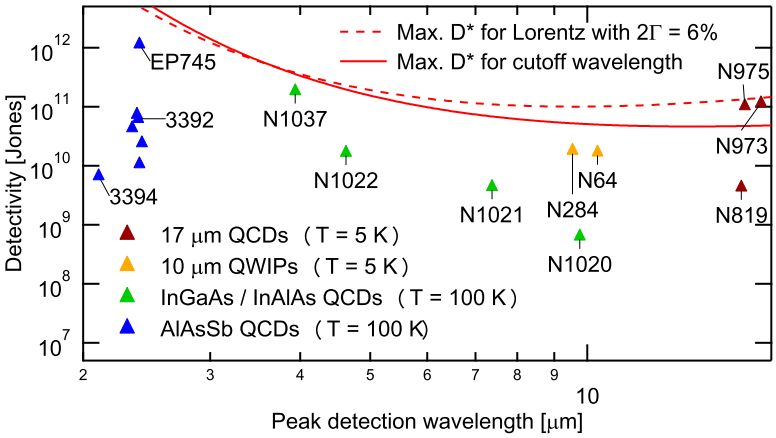

Figure 8.1: Detectivities of samples presented in this work. The red lines show the background limited detectivity for a hemispheric FOV and a 300 K background; the solid line is calculated for cutoff absorption, the dashed line for a Lorentzian absorption.

linewidth is limited by a higher $\mathcal{D}^*_{BLIP} = 1.4 \times 10^{11}$ Jones, as it does not 'see' most of the 300 K background irradiance. Although the 17 µm QCDs have a near optimal $\mathcal{D}^*$ at 5 K, it rapidly decreases with increasing temperature: at 65 K, $\mathcal{D}^* = 1.4 \times 10^8$ Jones. The same tendency is observed for the two photoconductive QWIPs N64 and N284.

The $\mathcal{D}^*$ of the four investigated InGaAs / InAlAs QCDs at an operating temperature of 100 K is represented by green triangles. The 4 µm strained InGaAs / InAlAs QCD N1037 has a $\mathcal{D}^* = 1.9 \times 10^{11}$ Jones. Compared to commercially available photodetectors, it is the most competitive device in terms of $\mathcal{D}^*$ presented in this work: MCT detectors have a $\mathcal{D}^*$ of about 1×10^{11} Jones at 4 µm.

InGaAs / AlAsSb QCDs represented by blue triangles in figure 8.1 have $\mathcal{D}^*$ ranging from 6.7×10^9 Jones for 3394 detecting at 2 µm to 1.2×10^{12} Jones for EP745 detecting at 2.5 µm. The high $\mathcal{D}^*$ of EP745 is a result of its high resistance; the improvement compared to the other InGaAs / AlAsSb QCDs is due to additional AlAs diffusion barriers at the QW / barrier interface, which were only grown for EP745.

Although the electrical bandwidth of the presented detectors was not systematically investigated, a lower bandwidth limit of 200 MHz was measured for the 17 µm QCD N819 with a pulsed 17 µm quantum cascade laser. Based on results published for a 5 µm QCD by Hofstetter et al. [2006], the bandwidth of the presented detectors is supposed to lie above 10 GHz.

Outlook While the presented QCDs show a good performance at low temperatures, the background limited operation temperature T_{BLIP} is below 77 K except for the 4 µm QCD N1037 and the 2.5 µm QCD EP745. To increase T_{BLIP}, a higher responsivity and lower noise current is required. A better understanding of the escape probability and dark current would help to design QCDs with enhanced $\mathcal{D}^*$ and lower T_{BLIP}. The following simple escape probability model based on scattering lifetimes might be useful for future designs: the escape probability p_e is expressed by the phonon scattering lifetimes from the upper resonant state A_2 or B_1 towards the ground state A_1 (τ_{rel}) and towards the

extractor state C_1 (τ_{esc}):

$$p_e = \frac{\tau_{rel}}{\tau_{rel} + \tau_{esc}}. \tag{8.1}$$

Figure 8.2 illustrates this model: the left panel shows an excerpt of the conduction band profile of the 7.4 µm QCD N1021 presented in section 6.3.2; (8.1) results in $p_e = 0.09$. By decreasing the barrier thickness b_2, τ_{esc} is reduced resulting in $p_e = 0.60$ and thus a higher responsivity. The barrier thickness b_1 is simultaneously increased to maintain the device resistance, wherefor $\mathcal{D}^*$ should scale with the responsivity.

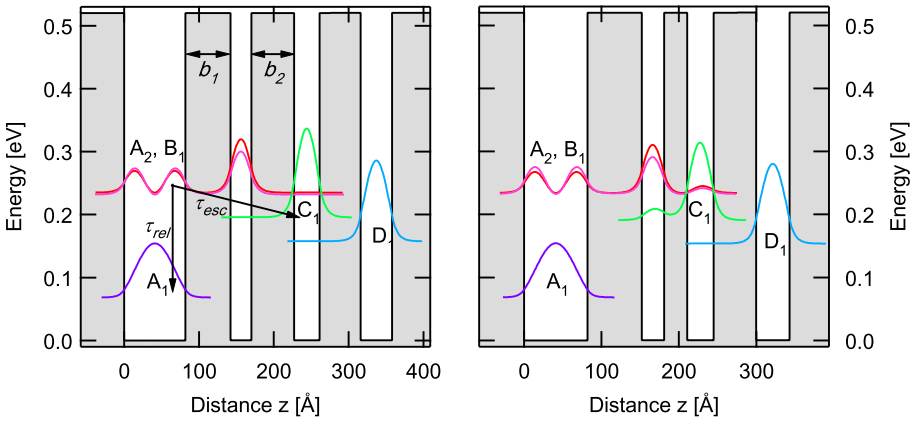

Figure 8.2: Left: conduction band of QCD N1021. τ_{rel} and τ_{esc} are lifetimes of the photoexcited electrons. Right: modified structure with a larger barrier thickness b_1 and a smaller b_2 resulting in a lower τ_{esc}.

It would be interesting to determine how far one can go with strained InGaAs / InAlAs material in terms of short wavelength QCDs. Faist et al. [1998] demonstrated quantum cascade laser (QCL) structures at wavelengths down to 3.4 µm in this system. As QCLs are more delicate towards material quality, QCD detection wavelengths around 3 µm do not seem too ambitious.

By improving the interface quality and straining the QW and barrier layers, InGaAs / AlAsSb QCDs can be pushed towards even shorter detection wavelengths. First, the performance around 2 µm should however be improved. The QCD design in this material system would also benefit from more accurate band diagram simulations of bound electron states close to the continuum.

The narrow detection linewidth of QCD detectors could lead to some interesting applications. By growing a heterostructure consisting of multiple QCD active region stacks detecting at different wavelengths, a 'spectrometer' could be realised where each active region stack is separately read out. Connecting all stacks in series would result in a broad band IR detector.

Finally, it seems that the time is mature enough to apply efficient grating couplers to QCDs. Grating couplers, which are routinely used for QWIP focal plane arrays, could drastically increase the absorption efficency of QCDs and open the path for MIR and NIR FPAs profiting from the biasless operation of QCDs.

Acknowledgments

I would like to thank

- My thesis director, Prof. Dr. Daniel Hofstetter, for giving me the opportunity to do this work in his group and for his guidance through my PhD.
- Dr. Esther Baumann. Most of the work presented here is not 'mine', but 'ours' (as can be guessed from my publication list). I only wrote this work down in time thanks to her help and motivation.
- The other members of Prof. Hofstetter's optoelectronics group: Dr. Marcel Graf, whose PhD thesis is the foundation of this work, as well as Dr. Ricardo Théron, Dr. Yargo Bonetti, and Matthieu Pellaton for their help.
- Dr. Quankui Yang from the Fraunhofer IAF in Freiburg for helping me out with conduction band simulations of the antimony based QCDs, his support and for reading this thesis and acting as a co examiner.
- Prof. Dr. Peter Seitz for reading this thesis and acting as co examiner.
- Prof. Dr. Jérôme Faist and the group members of his mesoscopic group: Tobias Gresch for his professional technical support of all these machines, Milan Fischer for the growth of InP based samples and for various moments spent together at work and on week-ends in the Alps, Dr. Marcella Giovannini for growth, Christoph Walther for discussions and Romain Terazzi for various discussions on physics.
- Christoph Manz from the Fraunhofer IAF in Freiburg, and Yuriy Fedoryshyn as well as Prof. Dr. Jäckel from the ETH Zürich for growth of antimony based QCDs.
- Peter Krötz and Dr. Guido Sonnabend from the University of Cologne, who assisted the frequency response measurements of the 17 µm QCD.
- Nicolas Hoyler for growth and all people from the electronic and mechanical workshops as well as the secretaries at the University of Neuchâtel for their support and for keeping our workplaces running .
- My family for her support and for not being too mad at me being socially non-existent over the last few years.

Bibliography

R. Akimoto, Y. Kinpara, K. Akita, F. Sasaki, and S. Kobayashi. Short-wavelength intersubband transitions down to 1.6 μm in ZnSe/BeTe type-II superlattices. *Appl. Phys. Lett.*, 78(5):580, 2001.

Z. I. Alferov. Electroluminescence of heavily-doped heterojunctions pAl_xGa_{1-x}As−nGaAs. *J. Lumin.*, 1-2:869, 1970.

T. Ando, A. B. Fowler, and F. Stern. Electronic properties of two-dimensional systems. *Rev. Mod. Phys.*, 54(2):437, 1982.

G. Bastard. *Wave mechanics applied to semiconductor heterostructures*. Les éditions de physique, Les Ulis Cedex, 1988.

E. Baumann. *Near infrared intersubband absorption and photovoltaic detection in GaN/AlN multi quantum well structures*. PhD thesis, University of Neuchâtel, Physics department, 2007. URL `http://doc.rero.ch/lm.php?url=1000,40,4,20071002085608-PW/These_BaumannE.pdf`.

E. Baumann, F. R. Giorgetta, D. Hofstetter, S. Leconte, F. Guillot, E. Bellet-Amalric, and E. Monroy. Electrically adjustable intersubband absorption of a GaN/AlN superlattice grown on a transistorlike structure. *Appl. Phys. Lett.*, 89(10):101121, 2006.

F. Bernardini and V. Fiorentini. Macroscopic polarization and band offsets at nitride heterojunctions. *Phys. Rev. B*, 57(16):R9427–R9430, 1998.

K. L. Campman, H. Schmidt, A. Imamoglu, and A. C. Gossard. Interface roughness and alloy-disorder scattering contributions to intersubband transition linewidths. *Appl. Phys. Lett.*, 69(17):2554, 1996.

F. Capasso, K. Mohammed, and A. Y. Cho. Resonant tunneling through double barriers, perpendicular quantum transport phenomena in superlattices, and their device applications. *IEEE J. Quantum Electron.*, 22(9):1853–1869, 1986.

K. K. Choi, S. V. Bandara, S. D. Gunapala, W. K. Liu, and J. M. Fastenau. Detection wavelength of InGaAs/AlGaAs quantum wells and superlattices. *J. Appl. Phys.*, 91(2): 551, 2002.

S. L. Chuang. *Physics of optoelectronic devices*. Wiley New York, 1995.

H. C. Chui, E. L. Martinet, M. M. Fejer, and Jr. J. S. Harris. Short wavelength intersubband transitions in InGaAs/AlGaAs quantum wells grown on GaAs. *Appl. Phys. Lett.*, 64(6):736, 1994.

L. C. Chui, J. S. Smith, S. Margalit, A. Yariv, and A. Y. Cho. Application of internal photoemission from quantum-well and heterojunction superlattices to infrared photodetectors. *Infrared Phys.*, 23:93, 1983.

B. C. Covington, C. C. Lee, B. H. Hu, H. F. Taylor, and D. C. Streit. Infrared intersubband absorption in GaAs/AlAs multiple quantum wells. *Appl. Phys. Lett.*, 54(21):2145, 1989.

P. Cristea, Y. Fedoryshyn, and H. Jäckel. Growth of AlAsSb/InGaAs mbe-layers for all-optical switches. *J. Cryst. Growth*, 278(1-4):544–547, 2005.

P. Cristea, Y. Fedoryshyn, J. F. Holzman, F. Robin, H. Jäckel, E. Müller, and J. Faist. Tuning the intersubband absorption in strained AlAsSb/InGaAs quantum wells towards the telecommunications wavelength range. *J. Appl. Phys.*, 100(11):116104, 2006.

L. Doyennette, L. Nevou, M. Tchernycheva, A. Lupu, F. Guillot, E. Monroy, R. Colombelli, and F.H. Julien. GaN-based quantum dot infrared photodetector operating at 1.38 μm. *Electron. Lett.*, 41(19):1077–1078, 2005.

J.-Y. Duboz, J. A. Gupta, M. Byloss, G. C. Aers, H. C. Liu, and Z. R. Wasilewski. Intersubband transitions in InGaNAs/GaAs quantum wells. *Appl. Phys. Lett.*, 81(10): 1836, 2002.

L. Esaki and H. Sakaki. New photoconductor. *IBM Tech. Discl. Bull.*, 20:2456, 1977.

L. Esaki and R. Tsu. Superlattice and negative differential conductivity in semiconductors. *IBM J. of Research and Development*, 14(1):61, 1970.

J. Faist, F. Capasso, D. L. Sivco, C. Sirtori, A. L. Hutchinson, and A. Y. Cho. Quantum cascade laser. *Science*, 264(5158):553–556, 1994.

J. Faist, F. Capasso, D. L. Sivco, A. L. Hutchinson, S. G. Chu, and A. Y. Cho. Short wavelength ($\leq$3.4 μm) quantum cascade laser based on strained compensated InGaAs/AlInAs. *Appl. Phys. Lett.*, 72:680, 1998.

J. Faist, F. Capasso, C. Sirtori, D. L. Sivco, and A. Y. Cho. *Quantum cascade lasers*, volume 66 of *Semiconductors and semimetals*. Academic press, London, UK, 2000.

M. A. Fauci, R. Breiter, W. Cabanski, W. Fick, R. Koch, J. Ziegler, and S. D. Gunapala. Medical infrared imaging - differentiating facts from fiction, and the impact of high precision quantum well infrared photodetector camera systems, and other factors, in its reemergence. *Infrared Physics and Technology*, 42(3):337, 2001.

R. Ferreira and G. Bastard. Evaluation of some scattering times for electrons in unbiased and biased single- and multiple-quantum-well structures. *Phys. Rev. B*, 40(2):1074–1086, 1989.

L. Gendron, M. Carras, A. Huynh, V. Ortiz, C. Koeniguer, and V. Berger. Quantum cascade photodetector. *Appl. Phys. Lett.*, 85(14):2824–2826, 2004.

L. Gendron, C. Koeniguer, V. Berger, and X. Marcadet. High resistance narrow band quantum cascade photodetectors. *Appl. Phys. Lett.*, 86(12):121116, 2005.

N. Georgiev and T. Mozume. Photoluminescence study of InGaAs/AlAsSb heterostructure. *J. Appl. Phys.*, 89(2):1064–1069, 2001.

F. R. Giorgetta, E. Baumann, D. Hofstetter, S. Leconte, F. Guillot, E. Bellet-Amalric, and E. Monroy. High frequency (f=2.37 GHz) room temperature operation of 1.55 μm AlN/GaN-based intersubband detector. *Electron. Lett.*, 43:185–186, 2007a.

F. R. Giorgetta, E. Baumann, D. Hofstetter, C. Manz, Q. Yang, K. Köhler, and M. Graf. InGaAs/AlAsSb quantum cascade detectors operating in the near infrared. *Appl. Phys. Lett.*, 91:111115, 2007b.

M. Graf, G. Scalari, D. Hofstetter, J. Faist, H. Beere, E. Linfield, D. Ritchie, and G. Davies. Terahertz range quantum well infrared photodetector. *Appl. Phys. Lett.*, 84(4):475–477, 2004.

S. D. Gunapala and S. V. Bandara. *Quantum well infrared photodetector (QWIP) focal plane arrays*, volume 62 of *Semiconductors and semimetals*. Academic press, London, UK, 2000.

S. D. Gunapala, S. V. Bandara, J. K. Liu, C. J. Hill, S. B. Rafol, J. M. Mumolo, J. T. Trinh, M. Z. Tidrow, and P. D. LeVan. Development of mid-wavelength and long-wavelength megapixel portable QWIP imaging cameras. *Infrared Physics & Technology*, 47(1-2): 67–75, 2005.

J. D. Heber, C. Gmachl, H. M. Ng, and A. Y. Cho. Comparative study of ultrafast intersubband electron scattering times at $\sim 1.55\,\mu$m wavelength in GaN/AlGaN heterostructures. *Appl. Phys. Lett.*, 81(7):1237–1239, 2002.

M. Helm. *The basic physics of intersubband transitions*, volume 62 of *Semiconductors and semimetals*. Academic press, London, UK, 2000.

W. Herschel. Experiments on the refrangibility of the invisible rays of the sun. By William Herschel, LL. D. F. R. S. *Philosophical Transactions of the Royal Society of London*, 90 (-1):284, 1800. doi:10.1098/rstl.1800.0015.

D. Hofstetter, M. Beck, and J. Faist. Quantum-cascade laser structures as photodetectors. *Appl. Phys. Lett.*, 81(15):2683–2685, 2002.

D. Hofstetter, S.-S. Schad, H. Wu, W. J. Schaff, and L. F. Eastman. GaN/AlN-based quantum-well infrared photodetector for 1.55 μm. *Appl. Phys. Lett.*, 83(3):572–574, 2003.

D. Hofstetter, M. Graf, T. Aellen, J. Faist, L. Hvozdara, and S. Blaser. 23 GHz operation of a room temperature photovoltaic quantum cascade detector at 5.35 μm. *Appl. Phys. Lett.*, 89(6):061119, 2006.

D. Hofstetter, E. Baumann, F. R. Giorgetta, F. Guillot, S. Leconte, and E. Monroy. Optically nonlinear effects in intersubband transitions of GaN/AlN-based superlattice structures. *Appl. Phys. Lett.*, 91(13):131115, 2007.

N. Iizuka, K. Kaneko, and N. Suzuki. Near-infrared intersubband absorption in GaN/AlN quantum wells grown by molecular beam epitaxy. *Appl. Phys. Lett.*, 81(10):1803–1805, 2002.

J. B. Johnson. Thermal agitation of electricity in conductors. *Phys. Rev.*, 32(1):97, 1928.

C. Kittel. *Introduction to solid state physics.* John Wiley & Sons, 1996.

C. Koeniguer, G. Dubois, A. Gomez, and V. Berger. Electronic transport in quantum cascade structures at equilibrium. *Physical Review B*, 74(23):235325, 2006.

W. Kohn and L. J. Sham. Self-consistent equations including exchange and correlation effects. *Phys. Rev.*, 140(4A):1133, 1965.

E. S. Koteles and W. R. Datars. Two-phonon absorption in InP and GaP. *Solid State Commun.*, 19(3):221, 1976.

H. Kroemer. Quasi-electric and quasi-magnetic fields in non-uniform semiconductors. *RCA Review*, 18:332, 1957.

P. Krötz, D. Stupar, J. Krieg, G. Sonnabend, M. Sornig, F. Giorgetta, E. Baumann, M. Giovannini, N. Hoyler, D. Hofstetter, and R. Schieder. Applications for quantum cascade lasers and detectors in mid-infrared high-resolution heterodyne astronomy. *Appl. Phys. B*, 2008. doi:10.1007/s00340-007-2832-2.

K. T. Lai, R. Gupta, M. Missous, and S. K. Haywood. Intersubband absorption from 2 to 7 μm in strain-compensated double-barrier $In_xGa_{1-x}As$ multiquantum wells. *Semicond. Sci. Technol.*, 19(11):1263, 2004.

D. C. Larrabee, G. A. Khodaparast, J. Kono, K. Ueda, Y. Nakajima, M. Nakai, S. Sasa, M. Inoue, K. I. Kolokolov, J. Li, and C. Z. Ning. Temperature dependence of intersubband transitions in InAs/AlSb quantum wells. *Appl. Phys. Lett.*, 83(19):3936–3938, 2003.

B. F. Levine. Quantum-well infrared photodetectors. *J. Appl. Phys.*, 74(8):R1–R81, 1993.

B. F. Levine, K. K. Choi, C. G. Bethea, J. Walker, and R. J. Malik. New 10 μm infrared detector using intersubband absorption in resonant tunneling GaAlAs superlattices. *Appl. Phys. Lett.*, 50(16):1092–1094, 1987.

B. F. Levine, A. Y. Cho, J. Walker, R. J. Malik, D. A. Kleinman, and D. L. Sivco. InGaAs/InAlAs multiquantum well intersubband absorption at a wavelength of $\lambda = 4.4\,\mu$m. *Appl. Phys. Lett.*, 52(18):1481, 1988.

B. F. Levine, S. D. Gunapala, and R. F. Kopf. Photovoltaic GaAs quantum well infrared detectors at 4.2 μm using indirect Al_xGa_{1-x} barriers. *Appl. Phys. Lett.*, 58(14):1551, 1991.

B. F. Levine, A. Zussman, S. D. Gunapala, M. T. Asom, J. M. Kuo, and W. S. Hobson. Photoexcited escape probability, optical gain, and noise in quantum well infrared photodetectors. *J. Appl. Phys.*, 72:4429, 1992.

M. E. Levinshtein, S. L. Rumyantsev, and M. S. Shur, editors. *Properties of advanced semiconductor materials: GaN, AlN, InN, BN, SiC, SiGe.* John Wiley and Sons, 2001.

H. C. Liu. Dependence of absorption-spectrum and responsivity on the upper state position in quantum-well intersubband photodetectors. *J. Appl. Phys.*, 73(6):3062, 1993.

H. C. Liu. *Quantum well infrared photodetector physics and novel devices*, volume 62 of *Semiconductors and semimetals.* Academic press, London, UK, 2000.

H. C. Liu and J. Li. Quantum well intersubband heterodyne infrared detection up to 82 GHz. *Appl. Phys. Lett.*, 67(11):1594–1596, 1995.

H. C. Liu, C. Y. Song, A. Shen, M. Gao, Z. R. Wasilewski, and M. Buchanan. GaAs/AlGaAs quantum-well photodetector for visible and middle infrared dual-band detection. *Appl. Phys. Lett.*, 77(16):2437, 2000.

H. C. Liu, C. Y. Song, A. J. SpringThorpe, and J. C. Cao. Terahertz quantum-well photodetector. *Appl. Phys. Lett.*, 84(20):4068, 2004.

H. C. Liu, C. Y. Song, J. A. Gupta, and G. C. Aers. Intersubband transition in narrow GaInNAs/GaAs quantum wells. *Appl. Phys. Lett.*, 89(24):241122, 2006.

H. Lu, A. Shen, M. C. Tamargo, C. Y. Song, H. C. Liu, S. K. Zhang, R. R. Alfano, and M. Munoz. Midinfrared intersubband absorption in Zn_xCd_{1-x} $Se/Zn_{x'}Cd_{y'}$ $Mg_{1-x'-y'}Se$ multiple quantum well structures. *Appl. Phys. Lett.*, 89(13):131903, 2006.

M. O. Manasreh, F. Szmulowicz, D. W. Fischer, K. R. Evans, and C. E. Stutz. Intersubband infrared absorption in a $GaAs/Al_{0.3}Ga_{0.7}As$ quantum well structure. *Appl. Phys. Lett.*, 57(17):1790, 1990.

X. Marcadet, C. Renard, M. Carras, M. Garcia, and J. Massies. InAs/AlAsSb based quantum cascade lasers. *Appl. Phys. Lett.*, 91(16):161104, 2007.

D. F. Nelson, R. C. Miller, and D. A. Kleinman. Band nonparabolicity effects in semiconductor quantum wells. *Phys. Rev. B*, 35(14):7770, 1987.

A. Neogi, H. Yoshida, T. Mozume, N. Georgiev, T. Akiyama, and O. Wada. Absorption saturation of near-infrared intersubband transition in lattice-matched InGaAs/AlAsSb quantum wells. *Physica E*, 7(1-2):183–186, 2000.

L. Nevou, M. Tchernycheva, F. H. Julien, F. Guillot, and E. Monroy. Short wavelength ($\lambda = 2.13\,\mu$m) intersubband luminescence from GaN/AlN quantum wells at room temperature. *Appl. Phys. Lett.*, 90(12):121106, 2007.

K. Ohtani, N. Matsumoto, H. Sakuma, and H. Ohno. Intersubband absorption in n-doped InAs/AlSb multiple-quantum-well structures. *Appl. Phys. Lett.*, 82(1):37, 2003.

D. G. Revin, J. W. Cockburn, M. J. Steer, R. J. Airey, M. Hopkinson, A. B. Krysa, L. R. Wilson, and S. Menzel. InGaAs/AlAsSb/InP quantum cascade lasers operating at wavelengths close to 3 μm. *Appl. Phys. Lett.*, 90(2):021108, 2007.

M. Rochat, D. Hofstetter, M. Beck, and J. Faist. Long-wavelength ($\lambda \approx 16\,\mu$m), room-temperature, single-frequency quantum-cascade lasers based on a bound-to-continuum transition. *Appl. Phys. Lett.*, 79(26):4271–4273, 2001.

A. Rogalski. Quantum well photoconductors in infrared detector technology. *J. Appl. Phys.*, 93(8):4355, 2003.

E. Rosencher and P. Bois. Model system for optical nonlinearities – asymmetric quantum-wells. *Phys. Rev. B*, 44(20):11315–11327, 1991.

E. Rosencher and B. Vinter. *Optoélectronique*. Masson, 1998.

E. Rosencher, P. Bois, J. Nagle, E. Costard, and S. Delaitre. Observation of nonlinear optical rectification at 10.6 μm in compositionally asymmetrical AlGaAs multiquantum wells. *Appl. Phys. Lett.*, 55(16):1597–1599, 1989.

G. Sarusi, S. D. Gunapala, J. S. Park, and B. F. Levine. Design and performance of very long-wavelength GaAs $Al_xGa_{1-x}As$ quantum-well infrared photodetectors. *J. Appl. Phys.*, 76(10):6001–6008, 1994.

H. Schneider. Optimized performance of quantum well intersubband infrared detectors: photovoltaic versus photoconductive operation. *J. Appl. Phys.*, 74(7):4789, 1993.

H. Schneider and H. C. Liu. *Quantum well infrared photodetectors*. Springer, 2006.

H. Schneider, F. Fuchs, B. Dischler, J. D. Ralston, and P. Koidl. Intersubband absorption and infrared photodetection at 3.5 and 4.2 μm in GaAs quantum wells. *Appl. Phys. Lett.*, 58(20):2234, 1991a.

H. Schneider, P. Koidl, F. Fuchs, B. Dischler, K. Schwarz, and J. D. Ralston. Photovoltaic intersubband detectors for $3 - 5\,\mu$m using GaAs quantum-wells sandwiched between AlAs tunnel barriers. *Semicond. Sci. Technol.*, 6(12C):C120, 1991b.

H. Schneider, K. Kheng, M. Ramsteiner, J. D. Ralston, F. Fuchs, and P. Koidl. Transport asymmetry and photovoltaic response in (AlGa)As/AlAs/GaAs/(AlGa)As single-barrier quantum-well infrared detectors. *Appl. Phys. Lett.*, 60(12):1471, 1992.

F. Schwabl. *Quantenmechanik*. Springer, 1998.

E. Scott Barr. The infrared pioneers–II. Macedonio Melloni. *Infrared Phys.*, 2(2):67, 1962.

M. P. Semtsiv, U. Müller, W. T. Masselink, N. Georgiev, T. Dekorsy, and M. Helm. Intersubband transitions in GaP-AlP heterostructures. *Appl. Phys. Lett.*, 89(18):184102, 2006.

M. P. Semtsiv, M. Wienold, S. Dressler, and W. T. Masselink. Short-wavelength ($\lambda \approx 3.05\,\mu$m) InP-based strain-compensated quantum-cascade laser. *Appl. Phys. Lett.*, 90 (5):051111, 2007.

S. C. Shen. MCT versus quantum-well structures for IR detectors. *Semicond. Sci. Technol.*, 8(1):S443, 1993.

C. Sirtori, F. Capasso, J. Faist, and S. Scandolo. Nonparabolicity and a sum-rule associated with bound-to-bound and bound-to-continuum intersubband transitions in quantum-wells. *Phys. Rev. B*, 50(12):8663, 1994.

J. H. Smet, L. H. Peng, Y. Hirayama, and C. G. Fonstad. Electron intersubband transitions to 0.8 eV (1.55 μm) in InGaAs/AlAs single quantum wells. *Appl. Phys. Lett.*, 64(8):986, 1994.

J. S. Smith, L. C. Chiu, S. Margalit, A. Yariv, and A. Y. Cho. A new infrared detector using electron-emission from multiple quantum wells. *J. Vac. Sci. Technol. B*, 1(2):376, 1983.

G. Sonnabend, D. Wirtz, F. Schmülling, and R. Schieder. Tuneable heterodyne infrared spectrometer for atmospheric and astronomical studies. *Appl. Opt.*, 41(15):2978, 2002.

S. Strite and H. Morkoç. GaN, AlN, and InN: a review. *Journal of Vacuum Science and Technology B*, 10(4):1237–1266, 1992.

S. M. Sze. *Physics of semiconductor devices*. John Wiley & Sons, 2nd edition, 1981.

E. A. Valentijn and P. P. van der Werf. First extragalactic direct detection of large-scale molecular hydrogen in the disk of ngc 891. *The Astrophys. J.*, 522:L29, 1999.

I. Vurgaftman and J. R. Meyer. Band parameters for nitrogen-containing semiconductors. *J. Appl. Phys.*, 94(6):3675–3696, 2003.

I. Vurgaftman, J. R. Meyer, and L. R. Ram-Mohan. Band parameters for III–V compound semiconductors and their alloys. *J. Appl. Phys.*, 89(11):5815–5875, 2001.

L. C. West and S. J. Eglash. 1st observation of an extremely large-dipole infrared transition within the conduction-band of a GaAs quantum well. *Appl. Phys. Lett.*, 46(12):1156–1158, 1985.

Wikipedia. Infrared — wikipedia, the free encyclopedia, 2007. URL `http://en.wikipedia.org/w/index.php?title=Infrared&oldid=174429030`. [Online; accessed 1-December-2007].

W. L. Wolfe and G. J. Zissis, editors. *The infrared handbook*. Environmental Research Institute of Michigan, 2nd edition, 1985.

Q. Yang, C. Manz, W. Bronner, N. Lehmann, F. Fuchs, K. Köhler, and J. Wagner. High peak-power (10.5 W) GaInAs/AlGaAsSb quantum-cascade lasers emitting at $\lambda \sim 3.6 - 3.8\,\mu$m. *Appl. Phys. Lett.*, 90(12):121134, 2007.

L. S. Yu and S. S. Li. A metal grating coupled bound-to-miniband transition GaAs multiquantum well/superlattice infrared detector. *Appl. Phys. Lett.*, 59(11):1332, 1991.

Publication List

E. Baumann, F. R. Giorgetta, D. Hofstetter, L. Kirste, H. Wu, W. J. Schaff, and L. F. Eastman. Intersubband absorption in AlN/GaN-superlattice structures. *Phys. Stat. Sol. (c)*, 2(3):1014–1018, 2005a.

E. Baumann, F. R. Giorgetta, D. Hofstetter, H. Lu, X. Chen, W. J. Schaff, L. F. Eastman, S. Golka, W. Schrenk, and G. Strasser. Intersubband photoconductivity at 1.6 μm using a strain-compensated AlN/GaN superlattice. *Appl. Phys. Lett.*, 87(19):191102, 2005b.

E. Baumann, F. R. Giorgetta, D. Hofstetter, H. Wu, W. J. Schaff, L. F. Eastman, and L. Kirste. Tunneling effects and intersubband absorption in AlN/GaN superlattices. *Appl. Phys. Lett.*, 86(3):032110, 2005c.

E. Baumann, F. R. Giorgetta, D. Hofstetter, S. Golka, W. Schrenk, G. Strasser, L. Kirste, S. Nicolay, E. Feltin, J. F. Carlin, and N. Grandjean. Near infrared absorption and room temperature photovoltaic response in AlN/GaN superlattices grown by metal-organic vapor-phase epitaxy. *Appl. Phys. Lett.*, 89(4):041106, 2006a.

E. Baumann, F. R. Giorgetta, D. Hofstetter, S. Leconte, F. Guillot, E. Bellet-Amalric, and E. Monroy. Electrically adjustable intersubband absorption of a GaN/AlN superlattice grown on a transistorlike structure. *Appl. Phys. Lett.*, 89(10):101121, 2006b.

E. Baumann, F. R. Giorgetta, D. Hofstetter, F. Guillot, S. Leconte, E. Bellet-Amalric, and E. Monroy. GaN/AlN electro-optical modulator prototype at telecommunication wavelengths. *Phys. Stat. Sol. (c)*, 4:1621–1624, 2007.

D. Hofstetter, E. Baumann, F. R. Giorgetta, M. Graf, M. Maier, F. Guillot, E. Bellet-Amalric, and E. Monroy. High-quality AlN/GaN-superlattice structures for the fabrication of narrow-band 1.4 μm photovoltaic intersubband detectors. *Appl. Phys. Lett.*, 88(12):121112, 2006.

D. Hofstetter, L. Despont, M. G. Garnier, E. Baumann, F. R. Giorgetta, P. Aebi, L. Kirste, H. Lu, and W. J. Schaff. Structural investigations of epitaxial InN by x-ray photoelectron diffraction and x-ray diffraction. *Appl. Phys. Lett.*, 90(19):191912, 2007.

P. Krötz, D. Stupar, J. Krieg, G. Sonnabend, M. Sornig, F. R. Giorgetta, E. Baumann, M. Giovannini, N. Hoyler, D. Hofstetter, and R. Schieder. Applications for quantum cascade lasers and detectors in mid-infrared high-resolution heterodyne astronomy. *Appl. Phys. B*, pages –, 2008. doi:10.1007/s00340-007-2832-2.

A. Lupu, F. H. Julien, S. Golka, G. Pozzovivo, G. Strasser, E. Baumann, F. R. Giorgetta, D. Hofstetter, S. Nicolay, M. Mosca, E. Feltin, J.-F. Carlin, and N. Grandjean. Lattice matched GaN–InAlN waveguides at $\lambda = 1.55\,\mu$m grown by metal–organic vapor phase epitaxy. *IEEE Photonics Technology Letters*, 20(2):102, 2008.

E. Monroy, F. Guillot, S. Leconte, E. Bellet-Amalric, E. Baumann, F. R. Giorgetta, D. Hofstetter, L. Nevou, M. Tchernycheva, L. Doyennette, F. H. Julien, T. Remmele, and M. Albrecht. MBE growth of nitride-based photovoltaic intersubband detectors. *Superlattices Microstruct.*, 40(4-6):418–425, 2006a.

E. Monroy, F. Guillot, S. Leconte, E. Bellet-Amalric, L. Nevou, L. Doyennette, M. Tchernycheva, F. H. Julien, E. Baumann, F. R. Giorgetta, D. Hofstetter, and L. S. Dang. III-nitride nanostructures for infrared optoelectronics. *Acta Physica Polonica A*, 110 (3):295–301, 2006b.

F. R. Giorgetta, E. Baumann, M. Graf, L. Ajili, N. Hoyler, M. Giovannini, J. Faist, D. Hofstetter, P. Krötz, and G. Sonnabend. 16.5 μm quantum cascade detector using miniband transport. *Appl. Phys. Lett.*, 90(23):231111, 2007a.

F. R. Giorgetta, E. Baumann, D. Hofstetter, S. Leconte, F. Guillot, E. Bellet-Amalric, and E. Monroy. High frequency (f=2.37 GHz) room temperature operation of 1.55 μm AlN/GaN-based intersubband detector. *Electron. Lett.*, 43:185–186, 2007b.

F. R. Giorgetta, E. Baumann, D. Hofstetter, C. Manz, Q. Yang, K. Köhler, and M. Graf. InGaAs/AlAsSb quantum cascade detectors operating in the near infrared. *Appl. Phys. Lett.*, 91:111115, 2007c.

F. R. Giorgetta, E. Baumann, R. Theron, M. L. Pellaton, M. Fischer, J. Faist, and D. Hofstetter. Short wavelength (4 μm) quantum cascade detector based on strain compensated InGaAs / InAlAs. *Submitted to Appl. Phys. Lett.*, 2008.

Z. Wang, K. Reimann, M. Woerner, T. Elsaesser, D. Hofstetter, E. Baumann, F. R. Giorgetta, H. Wu, W. J. Schaff, and L. F. Eastman. Ultrafast hole burning in intersubband absorption lines of GaN/AlN superlattices. *Appl. Phys. Lett.*, 89(15):151103, 2006.

Appendix A

Interband Responsivity in Intersubband Photodetectors

For some of the presented detectors, an interband (IB) photocurrent originating from the QW was observed. Figure A.1 shows the IB for the 17 µm QCD N819 presented in section 6.3.1. At 10 K, the IB signal peaks at 7056 cm^{-1} (1.4 µm), which corresponds to the IB transition energy of the intermediate extractor miniband of N819 of 7096 cm^{-1}. The peak responsivity of the IB signal decreases with temperature.

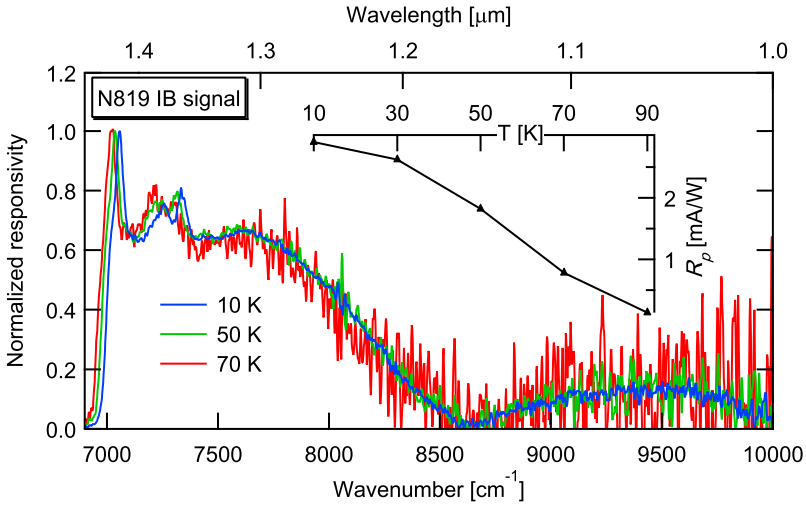

Figure A.1: Normalized IB responsivity of the InGaAs / InAlAs QCD N819 with ISB peak signal at 17 µm for different temperatures. Inset: peak IB responsivity $\mathcal{R}_P^{IB}$ as function of temperatures.

The IB signal of the InGaAs / AlAsSb QCD EP745 detecting at 2.5 µm presented in section 7.2.2 is displayed in figure A.2. The signal shown in the right panel peaks around 9800 cm^{-1} (1 µm) at 10 K and corresponds to ground state IB transitions in intermediate extractor QWs. The signal shown in the left panel peaks around 7800 cm^{-1} (1.28 µm). Its origin is not quite clear: the bandgap of the bulk InGaAs contact layers corresponds to 7270 cm^{-1} at 10 K (including the blue shift introduced by the degenerate doping), whereas

the IB transition energy in the thickest QW is 8053 cm^{-1}. Also, it is the only observed IB peak which does not shift with temperature, which could be an indication that it is a measurement artefact. Both IB signals are maximal at 200 K.

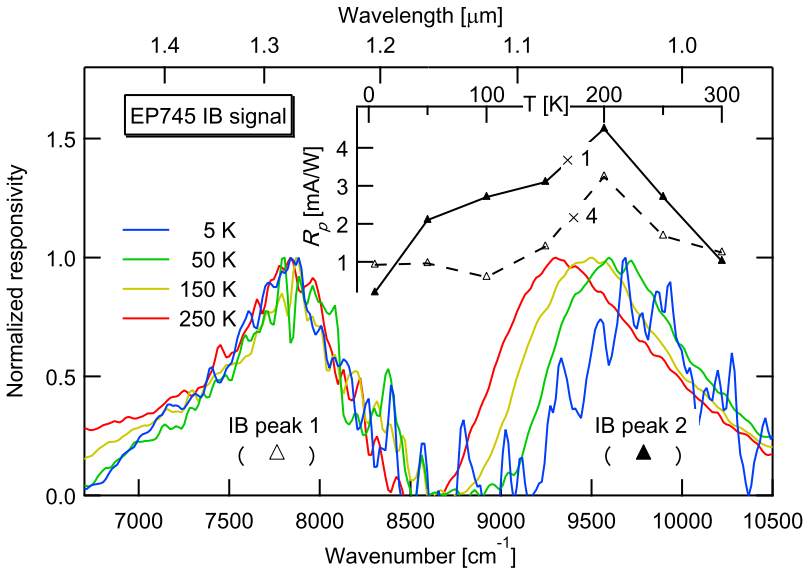

Figure A.2: Normalized IB responsivity of InGaAs / AlAsSb QCD EP745 with ISB peak signal at 2.5 μm for different temperatures. The left peak (IB peak 1) and right peak (IB peak 2) are normalized separately. The inset shows $\mathcal{R}_P^{IB}$ for both peaks.

Figure A.3 shows the IB signal of the strained InGaAs / InAlAs 4 μm QCD N1037 presented in section 7.1. The bottom panel depicts the normalized IB signal for different temperatures. The high energy peak at 8130 cm^{-1} (1.23 μm) is comparable to the IB energy of the largest QW of 8053 cm^{-1}; the small discrepancy is explained by the fact that the blue shift due to the quantized hole state was not taken into account for the calculation of the IB energy. The origin of the low energy peak at 7560 cm^{-1} is unclear; the bandgap energy of the bulk contact layers of N1037 of 7270 cm^{-1} is significantly lower. In contrast to the low energy peak of EP745, it shifts with temperature. The IB signal increases with temperature.

The top panel of figure A.3 shows the IB signal of N1037 for different applied voltages at 100 K. As seen in the inset, the IB signal is photoconductive, reaching a peak responsivity of 75 mA/W at −5 V. The IB signal is minimal at +1 V. Except for the weak signal at +1 V and the apparition of a low energy shoulder at high bias amplitudes, the spectral shape of the IB signal does not change with bias amplitude.

In conclusion, an IB signal of three QCDs based on the tree material systems used in this work is presented. Based on their transition energies, the IB signals can be attributed to QWs of the active region. The temperature dependence of the IB signal is not consistent among the three presented samples and not well understood. For some applications, the IB signal can be desirable; a two color QWIP / IB detector was published by Liu et al. [2000]. On the other hand, the IB signal reduces the background limited detectivity of QCDs, as more background photons are detected. Also, potential spectroscopic applica-

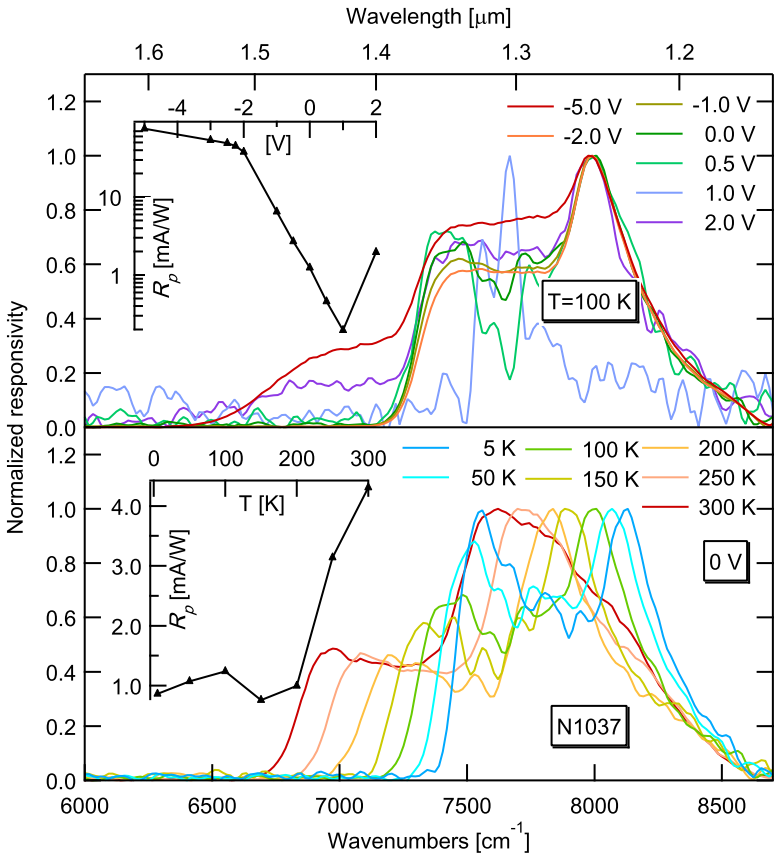

Figure A.3: Normalized IB responsivity of the strained InGaAs / InAlAs QCD N1037 with ISB peak signal at 4 µm. Bottom panel: for different temperatures and 0 V applied bias; inset: peak IB responsivity $\mathcal{R}_P^{IB}$. Top panel: for different bias voltages at 100 K; inset: $\mathcal{R}_P^{IB}$.

tions would require devices with a narrow and unique detection line. For both cases, it would be benefitial to further investigate the IB signal behavior of ISB devices. A better understanding of its origin would hopefully allow to tailor the IB signal to specific needs.

Appendix B

Simulated Conduction Band Diagrams

This appendix shows the simulated conduction band diagrams of the 17 µm QCD N973 (section 6.3.1), and of the 4.7 µm QCD N1022 and the 7.5 µm QCD N1021 (section 6.3.2).

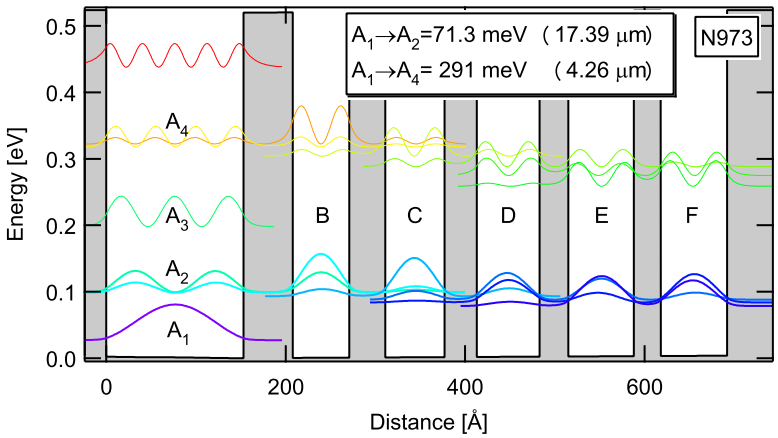

Figure B.1: Conduction band profile of the 17 µm QCD N973 discussed in section 6.3.1

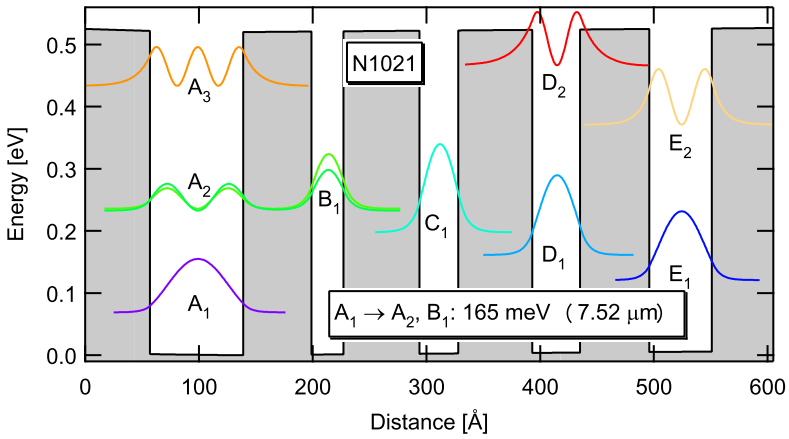

Figure B.2: Conduction band profile of the 7.5 µm QCD N1021 discussed in section 6.3.2

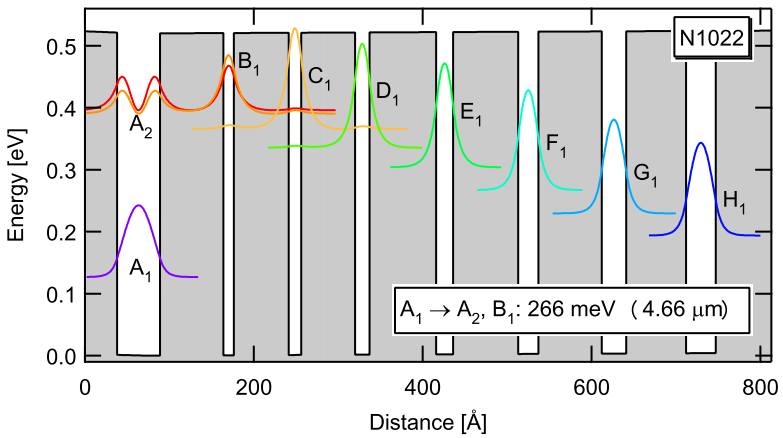

Figure B.3: Conduction band profile of the 4.7 µm QCD N1022 discussed in section 6.3.2